SLAC-R-958

Measurement of the decay $B \to \omega \ell \nu$ with the *BABAR* detector and determination of $|V_{ub}|$

by

Martin Nagel

M.S., Rose-Hulman Institute of Technology, 2001

A thesis submitted to the

Faculty of the Graduate School of the

University of Colorado in partial fulfillment

of the requirements for the degree of

Doctor of Philosophy

Department of Physics

2010

Work supported in part by US Department of Energy contract DE-AC02-76SF00515.

SLAC National Accelerator Laboratory, Menlo Park, CA 94025

This thesis entitled:
Measurement of the decay $B \to \omega \ell \nu$ with the *BABAR* detector and determination of $|V_{ub}|$
written by Martin Nagel
has been approved for the Department of Physics

Uriel Nauenberg

Second reader

Date

The final copy of this thesis has been examined by the signatories, and we find that both the content and the form meet acceptable presentation standards of scholarly work in the above mentioned discipline.

Nagel, Martin (Ph.D., Physics)

Measurement of the decay $B \to \omega \ell \nu$ with the *BABAR* detector and determination of $|V_{ub}|$

Thesis directed by Professor Uriel Nauenberg

We measure the branching fraction of the exclusive charmless semileptonic decay $B \to \omega \ell \nu_\ell$, where ℓ is either an electron or a muon, with the charged B meson recoiling against a tag B meson decaying in the charmed semileptonic modes $B \to D \ell \nu_\ell$ or $B \to D^* \ell \nu_\ell$. The measurement is based on a dataset of 426.1 fb^{-1} of e^+e^- collisions at a CM energy of 10.58 GeV recorded with the *BABAR* detector at the PEP-II asymmetric B Factory located at the SLAC National Accelerator Laboratory. We also calculate the relevant $B \to \omega$ hadronic form factors to determine the magnitude of the Cabibbo-Kobayashi-Maskawa matrix element $|V_{ub}|$.

Acknowledgements

In an attempt that is bound to fall short, I will try to acknowledge all those who have contributed to and helped me through my graduate experience. First and foremost, I want to thank my advisor, Uriel Nauenberg, for his support, his advice, and his patience throughout my years as a graduate student. Second, I thank the members of the semileptonic AWG at *BABAR*, for their great help in putting this analysis together, in particular Vera Luth and Jochen Dingfelder. The greatest amount of gratitude I owe to David Lopes Pegna, who provided valuable feedback and advice on an almost daily basis during the later stages of my analysis.

I would also like to thank the *BABAR* Collaboration as a whole for providing such a great ressource for all things related to a high energy physics analysis, from C++ coding advice, detector hardware expertise, and profound physics insights, to the intricacies of statistics. Many thanks also to the accelerator and PEP-II teams for their dedication to achieve ever new record levels of luminosity.

Thanks to my fellow graduate students Wells Wulsin and Manuel Franco Sevilla and to my part-time office mates Shenjian Chen, Jinlong Zhang, Kevin Flood, and Carl Vuosalo for fruitful discussions and practical advice.

I also want to thank the University of Colorado and the Department of Energy for financial support of my research.

Last, but not least: my wife Safoora. We stood together during these not always easy years, and this degree is her achievement even more than mine.

Contents

Chapter

1 Introduction 1

2 Theory 4

2.1 The Standard Model 4

2.1.1 Particles and Interactions 4

2.1.2 Lagrangian 8

2.1.3 Discrete symmetries of the SM 9

2.1.4 Flavor mixing and the CKM matrix 12

2.2 Semileptonic B meson decays 16

2.2.1 Inclusive charmless decays 18

2.2.2 Exclusive charmless decays 19

2.3 Hadronic form factors 20

2.3.1 Form factors and helicity amplitudes 20

2.3.2 Form factor calculations 24

2.4 Extraction of $|V_{ub}|$ from $B \to \omega \ell \nu$ 24

3 The Detector 26

3.1 The *BaBar* experiment 26

3.2 The linear accelerator and PEP-II 26

3.3 The *BaBar* detector 28

3.3.1 SVT 34
3.3.2 DCH 37
3.3.3 DIRC 40
3.3.4 EMC 44
3.3.5 IFR 49
3.3.6 Trigger 53
3.3.7 Data acquisition 57

4 Dataset 59
4.1 On-peak and off-peak data 59
4.2 Monte Carlo simulations 60
4.3 Skim 62
4.4 Data structure 65

5 Event Selection 66

6 Candidate Selection 72
6.1 PID and composite lists 72
6.2 Signal and background classification 74
6.3 Tag reconstruction 75
6.4 Signal reconstruction 81
6.5 Event reconstruction 83
6.6 Final candidate selection 89
6.7 Efficiencies 89

7 Data Monte-Carlo Comparison 92
7.1 Double tag correction 92
7.2 Comparison of data and MC simulation 93

8 Yield Extraction 100

8.1 Fit method 100

8.2 Fit result 102

8.3 Fit validation 106

9 Systematic Uncertainties 108

9.1 Stability of the fit 108

9.2 Uncertainties in detector response and reconstruction 108

9.2.1 Tracking efficiency 109

9.2.2 PID efficiency 109

9.2.3 Neutrals efficiency 109

9.3 Other uncertainties 110

9.4 Comparison between electrons and muons 110

10 Results and Discussion 113

10.1 Branching fraction 113

10.2 Determination of $|V_{ub}|$ 114

Bibliography 116

Appendix

A Mathematical Derivations 120

A.1 Derivation of $\cos\theta_{BY}$ 120

A.2 Derivation of $\cos^2\Phi_B$ 121

B Form factors from light-cone sum rules 123

Tables

Table

2.1 Various quantum number assignments and group representations of the SM fermions. 10

2.2 Various quantum number assignments and group representations of the SM bosons. 10

2.3 Selected properties of SM mesons relevant to this analysis. 11

3.1 Selected PEP-II design parameters. 29

3.2 Production cross sections for on-peak data. 31

3.3 Overview of the coverage, segmentation, and performance of the *BABAR* detector systems. 58

4.1 Data samples used in the analysis. 61

4.2 MC samples used in this analysis. 63

4.3 MC signal sample used in this analysis. 64

5.1 Summary of event selection cuts. 69

5.2 Efficiency of event selection cuts for various data samples. 71

6.1 Branching fractions for charm semileptonic B decays relevant to this analysis. 76

6.2 Branching fractions for the hadronic D decay modes used in this analysis. 77

6.3 Relative selection efficiencies for various data samples. 91

8.1 Fit results for signal and background yields. 103

9.1 Summary of systematic errors. 111

10.1 Comparison with previous results of the branching fraction $\mathcal{B}(B^+ \to \omega \ell^+ \nu)$.113

10.2 Comparison of various results for $|V_{ub}|$. 115

B.1 Parameters for the LCSR form factor calculation. 124

Figures

Figure

2.1 The Standard Model of elementary particles. 6

2.2 Summary of the interactions between particles in the SM 7

2.3 The normalized unitarity triangle. 15

2.4 Constraints on the UT from various measurements. 17

2.5 Current measurements and world average of $|V_{ub}|$. 21

2.6 Exclusive measurements of $|V_{ub}|$. 22

2.7 Tree level Feynman diagram for the weak semileptonic decay $B^- \to \omega \ell^- \bar{\nu}_\ell$. 22

3.1 Schematic of the linear accelelerator and PEP-II. 27

3.2 Longitudinal view of the *BABAR* detector. 32

3.3 Transverse cross-section of the *BABAR* detector. 32

3.4 Amount of material in the *BABAR* detector. 33

3.5 Integrated luminosity delivered by PEP-II and recorded by *BABAR*. . . . 33

3.6 Transverse cross section of the SVT. 35

3.7 Longitudinal cross section of the SVT. 36

3.8 SVT hit reslution 37

3.9 Longitudinal cross section of the DCH. 38

3.10 Schematic layout of the drift cells for the four innermost superlayers. . . 38

3.11 Drift cell isochrones. 41

3.12 DCH single cell resolution. 41

3.13 DCH resolution in the transverse momentum p_T. 41

3.14 DCH track reconstruction efficiency. 41

3.15 Longitudinal cross section of the DIRC. 43

3.16 Schematics of the top half of the DIRC radiator barrel and imaging region. 43

3.17 PID performance. 44

3.18 Longitudinal cross section of the EMC. 45

3.19 Schematic view of an EMC crystal assembly. 46

3.20 Energy resolution of the EMC. 48

3.21 Angular resolution of the EMC. 48

3.22 The IFR barrel and endcaps. 50

3.23 Cross section of a planar RPC with the schematics of the HV connections. 51

3.24 Picture and schematic drawing of a LST module. 52

3.25 Lepton identification and pion misidentification probability. 54

3.26 Distribution of z_0 for L1 tracks 56

3.27 Schematic diagram of the data acquisition at *BABAR*. 56

4.1 Hadronic e^+e^- cross section at the Υ resonances. 61

5.1 Display of a $B \to \omega\mu\bar{\nu}$ event in the *BABAR* detector. 67

5.2 Distribution of the second normalized Fox-Wolfram momemt $R2$. 70

5.3 Number of charged tracks per event for various event types. 70

5.4 CM momentum distribution for various lepton types. 71

6.1 Mass of D candidate and mass difference between D^* and its corresponding D candidate. 78

6.2 Cosine of the angle between the tag B and the $Y^{(*)}$ system. 80

6.3 Mass of the ω candidate and cosine of the angle between the signal B and the X system. 82
6.4 CM momentum of the lepton candidate versus that of the ω candidate. 84
6.5 Efficiency and gain in purity of the cut on the sum of ω and lepton momentum. 85
6.6 Invariant mass of lepton-lepton combinations and cosine of angle between them. 85
6.7 Legend for Figures 6.8 and 6.9. 87
6.8 Number of charged tracks and sum of charges in the remaining part of the event. 87
6.9 Residual energy in the remaining part of the event. 88
6.10 Purity vs. efficiency of remaining tracks and residual energy cuts. 88

7.1 Fit of the D mass distribution for the double tag study. 93
7.2 Legend for Figures 7.3 - 7.6. 94
7.3 Data MC comparison of $\cos\theta_{BY}$ and $\cos\theta_{BX}$. 95
7.4 Data MC comparison of number of remaining charged tracks. 96
7.5 Data MC comparison of residual energy. 97
7.6 Data MC comparison of the mass of the selected ω candidate. 98

8.1 Event kinematics of a double-semileptonic decay. 100
8.2 Distributions of $\cos^2\Phi_B$ for various sources and their corresponding PDFs. 104
8.3 Yiel extraction fit on MC and data. 104
8.4 Distribution of $\cos^2\Phi_B$ for data and MC. 105
8.5 Pull distribution of signal and background yields. 107

9.1 Data MC comparison of $\cos\theta_{BY}$ and $\cos\theta_{BX}$ for electrons and muons separately. 112

A.1 Event kinematics of a double-semileptonic decay. 121

B.1 Form factors for $B \to \omega$ decays as a function of q^2. 125

Chapter 1

Introduction

We live in a world of matter. We consist of matter. What seems obvious to the casual observer, is actually one of the big unsolved questions in cosmology. For every ordinary matter particle there exists a corresponding antimatter particle, and when a particle and its antiparticle meet, they annihilate each other in a flash of light. Right after the Big Bang, there were equal numbers of particles and antiparticles in the Universe. Over time, most of the particles annihilated with antiparticles, but a small amount of matter was left over at the end – this is what we are made of. Sakharov identified three necessary conditions to generate this excess of matter in the evolution of the Universe: departure from thermal equilibrium, baryon number violation, and both C and CP violation [1].

The laws of physics were originally thought to be exactly the same for particles and antiparticles. This is referred to as CP symmetry. The violation of this symmetry was first observed in neutral kaon decays in 1964 [2], implying that matter and antimatter do behave differently. As mentioned before, the violation of this symmetry is required for our very existence. In 1972, Kobayashi and Maskawa realized that CP violation arises quite naturally when the method of quark mixing proposed by Cabibbo [3] is extended from two to three generations of quarks [4]; they were subsequently awarded with half of the 2008 Nobel Prize in Physics.

A promising way to test the Kobayashi-Maskawa mechanism for CP violation is to

study the properties of B mesons [5, 6, 7], particularly in so-called "B-factories", where $B\overline{B}$ pairs are produced by annihilating electrons and positrons in head-on collisions. In order to see the asymmetry however, one needs to measure the lifetimes of the short-lived B mesons, which can be achieved by colliding beams with asymmetric energies, so that differences in the B meson lifetimes translate into measurable spatial separations of their decay verteces [8]. This is the motivation behind the *BABAR* experiment at the SLAC National Accelerator Laboratory, designed to study *CP* violation in the B system and thus the nature of the matter-antimatter asymmetry.

An important part of the Kobayashi-Maskawa mechanism for *CP* violation is the so-called CKM matrix element $|V_{ub}|$, which is most accessible, for both experimental and theoretical reasons, through charmless semileptonic B decays. These decays can be grouped in inclusive and exclusive decays, with different underlying theoretical uncertainties, which makes it desirable to have redundant measurements for both approaches. Typical exclusive measurements involve the decays $B \to \pi\ell\nu$, $B \to \rho\ell\nu$, $B \to \eta\ell\nu$, $B \to \eta'\ell\nu$, and $B \to \omega\ell\nu$ [9]. Of the latter decay, only two measurements have been published so far [10, 11]. In this dissertation, an alternative method is presented to measure the exclusive charmless semileptonic decay $B \to \omega\ell\nu$, which is also based on a larger dataset.

In the next chapter, we present a brief overview of the Standard Model of particle physics. In particular, we discuss the relationship of the CKM matrix element $|V_{ub}|$ and *CP* violation, and the theory of semileptonic B meson decays. In chapter 3, we present the experimental apparatus, i.e. the PEP-II storage ring and the *BABAR* detector. The dataset obtained from the experimental apparatus is described in chapter 4. The following two chapters outline the analysis strategy, in particular the details of the event and candidate selection, respectively. The approach to extract the $B \to \omega\ell\nu$ branching fraction from the data is presented in chapter 8, followed by a discussion of the dominant systematic uncertainties in chapter 9. In the last chapter, we describe the extraction of

the CKM matrix element $|V_{ub}|$ from the measured branching fraction, and report and discuss our findings.

Chapter 2

Theory

2.1 The Standard Model

The Standard Model (SM) of particle physics is a theory of three of the four known fundamental interactions and the elementary particles that take part in these interactions. It is formulated as a Lorentz-covariant quantum field theory invariant under transformations of the gauge group $SU(3)_c \times SU(2)_L \times U(1)_Y$, which is a combination of the $SU(3)_c$ gauge-invariant strong interactions of Quantum Chromodynamics (QCD) and the $SU(2)_L \times U(1)_Y$ gauge-invariant Glashow-Salam-Weinberg (GSW) theory of electroweak interactions. The fourth fundamental interaction, gravitation, is not included.

Quantum field theories are described in terms of a Lagrangian, from which the equations of motion are derived; particles enter the Lagrangian in terms of space-time dependent (localized) quantum mechanical fields. The requirement of invariance of the Lagrangain under certain gauge transformations makes the SM a quantum gauge theory and guarantees its renormalizability.

2.1.1 Particles and Interactions

The SM consists of three types of particles: spin-1/2 fermions that constitute all matter, spin-1 gauge vector bosons that mediate the interactions between these matter particles, and the spin-0 scalar Higgs boson, responsible for generating the masses

of both matter fermions and gauge bosons via the process of *spontaneous symmetry breaking*.[1]

The fermions themselves fall into two families, quarks and leptons, each of which is divided into three generations, as depicted in Fig. 2.1. The six quarks carry color degrees of freedom and transform as a triplet under the $SU(3)_c$ gauge group, i.e. they interact strongly as described in QCD. The leptons are color-neutral and transform as a $SU(3)_c$-singlet, i.e. they do not participate in strong interactions. Both quarks and leptons interact weakly and are grouped into left-handed $SU(2)_L$ doublets and right-handed singlets, since weak interactions violate parity and only interact with left-handed fermions.

$$f_L^q = q_L = \begin{pmatrix} u \\ d \end{pmatrix}_L \qquad f_R^q = u_R, d_R \qquad f_L^\ell = \ell_L = \begin{pmatrix} \nu_\ell \\ \ell \end{pmatrix}_L \qquad f_R^\ell = \nu_{\ell R}, \ell_R \tag{2.1}$$

All quarks and the charged leptons are also subject to electromagnetic interactions. Furthermore, for each fermion there exists a corresponding anti-fermion with the same mass but opposite charge and flavor quantum numbers.

In the SM, particles exert forces onto each other through the exchange of virtual gauge bosons. The strong interaction is mediated by the exchange of color-bearing gluons g_a, which belong to the octet representation of the $SU(3)_c$ gauge group.[2] Electromagnetic and weak forces are mediated by the exchange of photons γ and the weak gauge boson triplet $W^\pm$ and Z^0, respectively. These gauge fields are not manifest in the Lagrangian, since they are created from linear combinations of the weak isospin and weak hypercharge fields $\boldsymbol{W}$ and B through the Higgs mechanism, in particular:

$$W^{+\mu} = (W_1^\mu - \mathrm{i}W_2^\mu)/\sqrt{2} \qquad W^{-\mu} = (W_1^\mu + \mathrm{i}W_2^\mu)/\sqrt{2} \tag{2.2a}$$

$$Z^\mu = \cos\theta_W W_3^\mu - \sin\theta_W B^\mu \qquad A^\mu = \sin\theta_W W_3^\mu + \cos\theta_W B^\mu \tag{2.2b}$$

[1] A symmetry is said to be spontaneously broken if it is manifest in the Lagrangian but lacking the corresponding mass-degenerate multiplet structure.

[2] Gauge bosons generally belong to the adjoint representation of their symmetry group.

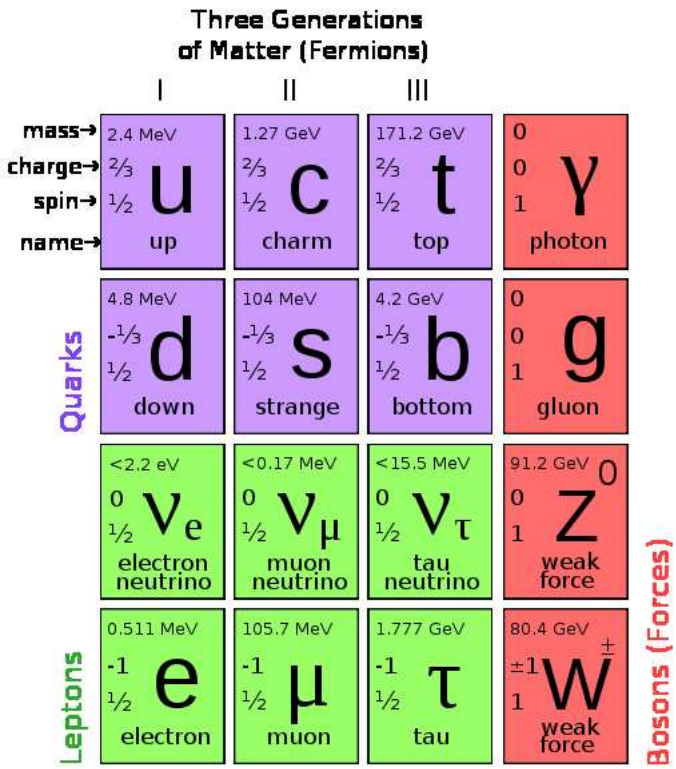

Figure 2.1: The Standard Model of elementary particles with three generations of fermions (in the three left columns), divided into quarks and leptons, and the gauge bosons in the rightmost column [12].

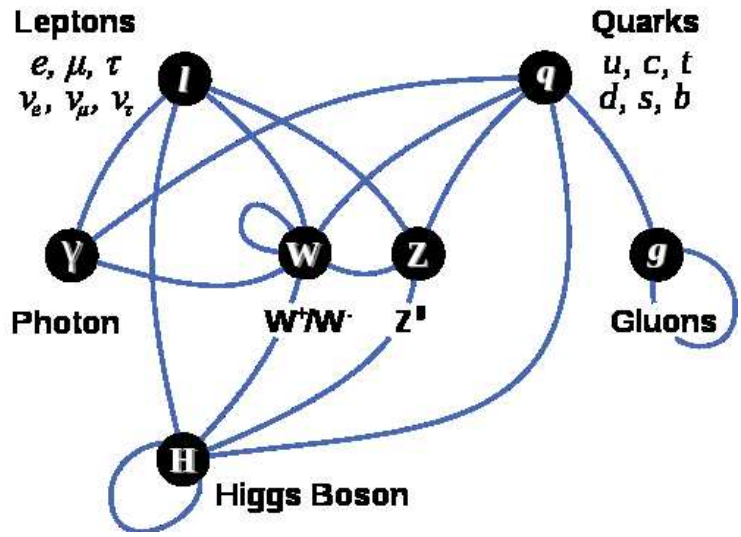

Figure 2.2: Summary of the interactions between particles in the SM [12].

where θ_W is called the weak mixing angle, given by $\cos\theta_W = g/(g^2 + g'^2)^{1/2}$ and $\sin\theta_W = g'/(g^2 + g'^2)^{1/2}$ (g and g' are explained in the next section). In this process, three of the gauge bosons acquired a mass term, while one of them, identified as the physical photon, remains massless.[3] The fact that $SU(3)$ and $SU(2)$ are non-Abelian Lie groups, whereas $U(1)$ is an Abelian Lie group, has the important consequence that the weak and strong gauge bosons carry weak and strong 'charge', respectively, and necessarily interact with themselves, whereas the photon does not. A compact summary of the three generations of matter fermions and the force-mediating gauge bosons of the SM is given in Fig. 2.1.

The Higgs boson $\phi = (\phi^+, \phi^0)$ is a weak isospin doublet and couples to the fermions via a Yukawa-type interaction, and to the electroweak gauge bosons via the covariant derivative. Its vacuum expectation value is non-zero, which means it spontaneously breaks the $SU(2)_c$ symmetry of the vacuum, in the process giving mass to all fermions (except the neutrinos), and all but one gauge bosons. This is an impor-

[3] In principle, gauge bosons have to be massless, since an explicit mass term violates gauge invariance [13, chapter 13].

tant aspect of the SM, since an explicit mass term for Dirac (or Majorana) fermions in the Lagrangian would violate $SU(2)_L$ invariance (due to the parity-violating property of weak interactions) [13, chapter 22]. A schematic illustration of the way the SM particles interact with each other is given in Fig. 2.2.

2.1.2 Lagrangian

The SM Lagrangian[4] can be grouped as follows

$$\mathcal{L} = \mathcal{L}_{\mathrm{QCD}} + \mathcal{L}^b_{\mathrm{EW}} + \mathcal{L}^f_{\mathrm{EW}} + \mathcal{L}^b_{\mathrm{H}} + \mathcal{L}^f_{\mathrm{H}} \tag{2.3}$$

where the bosonic electroweak Lagrangian

$$\mathcal{L}^b_{\mathrm{EW}} = -\frac{1}{4}\boldsymbol{W}_{\mu\nu}\cdot\boldsymbol{W}^{\mu\nu} - \frac{1}{4}B_{\mu\nu}B^{\mu\nu}{}^{5} \tag{2.4}$$

describes the kinetic energies and self-interactions of the gauge vector fields $W^{\pm}, Z, \gamma$, its fermionic counterpart

$$\mathcal{L}^f_{\mathrm{EW}} = \bar{\psi}_L\gamma^\mu\left(\mathrm{i}\partial_\mu - \frac{g}{2}\boldsymbol{\tau}\cdot\boldsymbol{W}_\mu - \frac{g'}{2}YB_\mu\right)\psi_L + \bar{\psi}_R\gamma^\mu\left(\mathrm{i}\partial_\mu - \frac{g'}{2}YB_\mu\right)\psi_R \tag{2.5}$$

contains the kinetic energies of the matter fields and their interactions with the gauge fields, and the bosonic and fermionic Higgs terms

$$\mathcal{L}^b_{\mathrm{H}} = \left[\left(\mathrm{i}\partial_\mu - \frac{g}{2}\boldsymbol{\tau}\cdot\boldsymbol{W}_\mu - \frac{g'}{2}YB_\mu\right)\phi\right]^\dagger\left[\left(\mathrm{i}\partial_\mu - \frac{g}{2}\boldsymbol{\tau}\cdot\boldsymbol{W}_\mu - \frac{g'}{2}YB_\mu\right)\phi\right] + \mu^2\phi^\dagger\phi - \frac{\lambda}{4}(\phi^\dagger\phi)^2 \tag{2.6}$$

$$\mathcal{L}^f_{\mathrm{H}} = -\left(G_1\bar{\psi}_L\phi\psi_R + G_2\bar{\psi}_L\phi_{\boldsymbol{C}}\psi_R + h.c.^{6}\right) \tag{2.7}$$

describe the couplings of the gauge bosons and the matter fermions with the Higgs, respectively, and thus their masses. In these equations

$$\boldsymbol{W}^{\mu\nu} = \partial^\mu\boldsymbol{W}^\nu - \partial^\nu\boldsymbol{W}^\mu - g\boldsymbol{W}^\mu\times\boldsymbol{W}^\nu \tag{2.8}$$

[4] Strictly speaking, $\mathcal{L}$ is the Lagrangian density.
[5] Einstein's sum convention is assumed throughout this dissertation.
[6] hermitian conjugate.

$$B^{\mu\nu} = \partial^\mu B^\nu - \partial^\nu B^\mu \tag{2.9}$$

where $\boldsymbol{W}^\mu$ is the weak isospin gauge boson isotriplet[7] and B^μ the weak hypercharge gauge boson isosinglet, together mediating the electroweak interaction, with coupling constants g and g', respectively. The $\boldsymbol{\tau}/2$ are matrix representations of the $SU(2)_L$ generators, and Y refers to the weak hypercharge quantum number. ψ_L denotes a left-handed fermion (quark or lepton) isodoublet, and ψ_R a right-handed fermion isosinglet; ϕ is the Higgs boson isodoublet. The Higgs potential is characterized by its parameters μ^2 and λ, and is responsible for creating the non-zero vacuum expectation value. The color and weak isospin group representations, and some relevant quantum numbers of the SM fermions and bosons are listed in Tables 2.1 and 2.2, respectively.

Free quarks are not observed in nature; a process called *confinement* guarantees that they are always bound into color-neutral hadrons. The hadrons themselves are divided into two groups, depending on their spin: baryons, bound states of three quarks,[8] are fermions which, together with leptons, form the basis of all matter; and mesons, unstable bound states of a quark and an antiquark, which have integer spin and are thus bosons. Selected properties of the mesons relevant to this analysis are listed in Table 2.3.

2.1.3 Discrete symmetries of the SM

Symmetry considerations play a crucial role in physics due to the profound connection between symmetries and conserved quantities, as formulated in Noether's theorem [16]. In addition to the continuous gauge symmetries discussed above, invariance under discrete transformations (or the lack thereof) also play an important role in the SM. These discrete transformations are parity $P : (t, \boldsymbol{x}) \rightarrow (t, -\boldsymbol{x})$, which inverts spatial coordinates of a system, effectively reversing the handedness of space, time reversal

[7] The multiplet classification 'iso-' refers to the weak isospin gauge group $SU(2)_L$.
[8] or three antiquarks, in which case they are called anti-baryons

Table 2.1: Various quantum number assignments and group representations of the SM fermions.

Field	spin ($\hbar$) S	$SU(3)_c \times SU(2)_L$ representation	isospin T_3	hypercharge Y	charge (e) Q
lh. neutrino ν_L^ℓ	1/2	1×2	1/2	-1	0
rh. neutrino ν_R^ℓ	1/2	1×1	0	0	0
lh. charged lepton ℓ_L	1/2	1×2	-1/2	-1	-1
rh. charged lepton ℓ_R	1/2	1×1	0	-2	-1
lh. up-type quark u_L	1/2	3×2	1/2	1/3	2/3
rh. up-type quark u_R	1/2	3×1	0	4/3	2/3
lh. down-type quark d_L	1/2	3×2	-1/2	1/3	-1/3
rh. down-type quark d_R	1/2	3×1	0	-2/3	-1/3

Table 2.2: Various quantum number assignments and group representations of the SM bosons. The shaded area refers to the electroweak part after symmetry breaking.

Field	spin ($\hbar$) S	$SU(3)_c \times SU(2)_L$ representation	isospin T_3	hypercharge Y	charge (e) Q
gluon g	1	8×1	0	0	0
hypercharge field B^μ	1	1×1	0	0	-[a]
isospin field $\boldsymbol{W}^\mu$	1	1×3	+1,0,-1	0	-[a]
photon field A^μ	1	$1 \times 1_Q$[b]	-[a]	-[a]	0
weak field $W^\pm$, Z^0	1	$1 \times 1_Q$[b]	-[a]	-[a]	+1,-1,0
Higgs ϕ^+	0	1×2	1/2	1	1
Higgs ϕ^0	0	1×2	-1/2	1	0

[a] Not well-defined.

[b] $SU(2)_L$-symmetry is broken; 1_Q refers to the singlet representation of the electromagnetic gauge group $U(1)_Q$.

Table 2.3: Selected properties of the SM mesons relevant to this analysis. Mesons are $q\overline{q}$ bound states with spin 0 or 1. If the orbital angular momentum is l, then the parity P is $(-1)^{l+1}$, and the charge conjugation C is $(-1)^{l+s}$. In terms of J^{PC} multiplets, the $l = 0$ states are the pseudoscalars (0^{-+}) and the vectors (1^{--}). The orbital excitations $l = 1$ are the scalars (0^{++}), the axial vectors (1^{++}) and (1^{+-}), and the tensors (2^{++}) [14]. I refers to the isospin multiplet the meson belons to.

Meson	Quark content	$I(J^{PC})$	mass (GeV/c^2)
π^0	$(u\bar{u} - d\bar{d})/\sqrt{2}$	$1(0^{-+})$	0.1350
$\pi^{\pm}$	$u\bar{d}$	$1(0^{-+})$	0.140
$K^{\pm}$	$u\bar{s}$	$\frac{1}{2}(0^{-+})$	0.494
ω^a	$\approx (u\bar{u} + d\bar{d})/\sqrt{2}$	$0(1^{--})$	0.782
D^0	$u\bar{c}$	$\frac{1}{2}(0^{-+})$	1.865
D^{*0}	$u\bar{c}$	$\frac{1}{2}(1^{--})$	2.007
$B^{\pm}$	$u\bar{b}$	$\frac{1}{2}(0^{-+})$	5.279

[a] The light quark isoscalar states with the same J^{PC}, i.e. η and η' in the peudoscalar and ω and ϕ in the vector meson nonet, are mixtures of the $SU(3)_f$ wave functions $\psi_8 = (u\bar{u} + d\bar{d} - 2s\bar{s})/\sqrt{6}$ and $\psi_1 = (u\bar{u} + d\bar{d} + s\bar{s})/\sqrt{3}$. These mixing relations can be expressed in terms of the $(u\bar{u} + d\bar{d})$ and $s\bar{s}$ components. It is found experimentally that the ω is nearly pure $(u\bar{u} + d\bar{d})$ [14, 15].

$T : (t, \boldsymbol{x}) \rightarrow (-t, \boldsymbol{x})$, and charge conjugation C, which conjugates internal quantum numbers of particles, effectively exchanging particles and antiparticles.

Although any relativistic field theory must be invariant under continuous Lorentz transformations, it need not be invariant under P, T, or C [17, chapter 3.6]. It is known experimentally, that C, P, and T symmetries are independently conserved by the strong and the electromagnetic interaction, but C and P are violated separately by the weak interaction. This is built into the SM by means of the vector-axial vector $(V - A)$ structure of the weak force, which acts only on left-handed fermions. The combined transformation *CP* however is a symmetry of an earlier form of the SM (and thus also of weak interactions) with only two generations of fermions. In fact, the observation of *CP* violation in the neutral kaon system prompted Kobayashi and Maskawa [4] to propose the existence of an additional set of fermions, based on the realization that a *CP*-violating phase is only possible with three fermion generations. Furthermore, the CPT theorem [18] requires any Lorentz-invariant, local quantum field theory with a unique vacuum state to be invariant under CPT, assuming the validity of the spin-statistics theorem [19, 20]; *CP* violation thus implies T violation, i.e. a fundamental directionality of time.

2.1.4 Flavor mixing and the CKM matrix

The quark part of Eq. 2.7, summed explicitly over three generations of up- and down-type quarks, is *a priori* not necessarily diagonal in the weak interaction family index i:

$$\mathcal{L}_{\mathrm{H}}^{q} = -(a_{ij}\bar{q}_{Li}\phi d_{Rj} + b_{ij}\bar{q}_{Li}\phi_{\boldsymbol{C}} u_{Rj} + h.c) \tag{2.10}$$

After symmetry breaking, it acquires mass terms that can be made hermitian and diagonal by suitable unitary transformations [21]:

$$\mathcal{L}_{\mathrm{H}}^{q} = -\left(1 - \frac{H}{v}\right)[m_u \bar{u}u + \ldots + m_b \bar{b}b] \tag{2.11}$$

where the Lagrangian Higgs field ϕ has been expanded about its vacuum expectation value $\langle 0|\,\phi\,|0\rangle = (0, v/\sqrt{2}) = (0, \sqrt{2\mu^2/\lambda})$, and the expansion parameter H is interpreted as the physical Higgs field [22]. Taking advantage of the linear recombination of $\boldsymbol{W}^{\mu}$ and B^{μ} after symmetry breaking, Eq. 2.5 can be split into a term that involves transitions between different members of left-handed fermion doublets, which induce changes in charge quantum number (and are thus called charged currents), and a neutral current term that acts only between right-handed singlets or the same members of a (left-handed) doublet. In terms of the new flavor-eigenstate basis, the neutral current part is diagonal (since the transformation matrices are unitary), meaning that the neutral current interactions do not change the flavor of the quarks. This is not true for the charged current part however, which can be written as

$$\mathcal{L}^{q}_{\mathrm{cc}} = -\frac{g}{\sqrt{2}}\bar{u}_{L\alpha}\gamma^{\mu}V_{\alpha\beta}d_{L\beta}W^{+}_{\mu} + h.c. \tag{2.12}$$

where $V_{\alpha\beta}$ is unitary and known as the Cabibbo-Kobayashi-Maskawa (CKM) matrix [3, 4]. It expresses the fact that (charged) weak interactions mix quark flavor eigenstates. Comparing the *CP*-conjugate of the first term in Eq. 2.12,

$$(\mathbf{CP})\bar{u}_{L\alpha}\gamma^{\mu}V_{\alpha\beta}d_{L\beta}W^{+}_{\mu}(\mathbf{CP})^{-\mathbf{1}} = \bar{d}_{L\alpha}\gamma^{\mu}V_{\alpha\beta}u_{L\beta}W^{-}_{\mu} \tag{2.13}$$

with its hermitian conjugate term,

$$\left[\bar{u}_{L\alpha}\gamma^{\mu}V_{\alpha\beta}d_{L\beta}W^{+}_{\mu}\right]^{\dagger} = \bar{d}_{L\alpha}\gamma^{\mu}V^{*}_{\alpha\beta}u_{L\beta}W^{-}_{\mu} \tag{2.14}$$

it becomes clear that *CP* violation in weak interactions arises from complex CKM matrix elements. The charged current Lagrangian is diagonal in the mass eigenstate basis $(u, c, t\,|\,d, s, b) \rightarrow (u, c, t\,|\,d', s', b')$ with:

$$\begin{pmatrix} d' \\ s' \\ b' \end{pmatrix} = \begin{pmatrix} V_{ud} & V_{us} & V_{ub} \\ V_{cd} & V_{cs} & V_{cb} \\ V_{td} & V_{ts} & V_{tb} \end{pmatrix} \begin{pmatrix} d \\ s \\ b \end{pmatrix} \tag{2.15}$$

The nine constraints for the CKM matrix elements from the unitarity condition leave three real parameters (mixing angles) and six phases; five of these six phases can be absorbed into the original unitary transformations of the six quark fields without changing the mass terms in Eq. 2.11, leaving one overall irreducible phase (since a uniform phase rotation of all six quarks leaves V invariant). The three mixing angles are small and satisfy a definite hierarchy, so that the CKM matrix can be approximated by the Wolfenstein parametrization [23]:

$$V_{\text{CKM}} = \begin{pmatrix} 1-\lambda^2/2 & \lambda & A\lambda^3(\rho - \mathrm{i}\eta) \\ -\lambda & 1-\lambda^2/2 & A\lambda^2 \\ A\lambda^3(1-\rho-\mathrm{i}\eta) & -A\lambda^2 & 1 \end{pmatrix} + \mathcal{O}(\lambda^4) \tag{2.16}$$

where all four parameters are real, with $A \simeq 1$, $\lambda \simeq 0.22$, and $(\rho - \mathrm{i}\eta)$ is the only complex factor and thus proportional to the irreducible phase. Six out of the nine original unitarity constraints

$$V^\dagger_{ik} V_{kj} = V^*_{ki} V_{kj} = \delta_{ij} \tag{2.17}$$

are homogeneous, and may be represented graphically in the complex plane as three closed triangles.[9] For two of these triangles, one side is found experimentally to be much shorter than the other two, and so they almost collapse to a line. One triangle however has sides of roughly equal length, and is related to coefficients that are relevant for the B system. This triangle, called the Unitary Triangle (UT), is shown in Fig. 2.3, scaled so that its base is of unit length and with $V_{cd}V^*_{cb}$ chosen to be real. The apex of the UT can be identified with the Wolfenstein parameters by $(\bar{\rho} = (1-\lambda^2/2)\rho, \bar{\eta} = (1-\lambda^2/2)\eta)$. Since CP is violated for $\eta \neq 0$, the area of the UT corresponds to the magnitude of CP violation in the SM.

A similar analysis can be carried out in the leptonic sector, leading to leptonic flavor mixing in charged currents via the leptonic analogue of the CKM matrix, called

[9] Three of the six homogeneous equations are just complex conjugates of the other three.

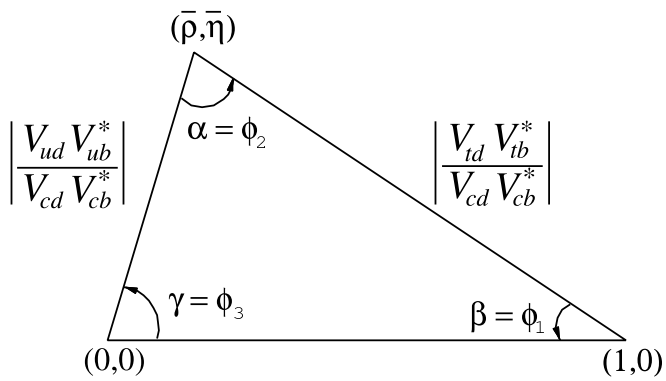

Figure 2.3: The normalized unitarity triangle. The phase convention is such that $V_{cd}V_{cb}^*$ is real and unity [14].

the MNS matrix [24], and to lepton mass terms similar to Eq. 2.11. If the neutrino masses vanish — or, more generally, if their mass eigenvalues are all equal — the neutrino fields can be redefined by another unitary transformation so as to reduce the charged current term to family-diagonal form. This links the question whether neutrinos are massive or massless to neutrino flavor mixing.

2.2 Semileptonic B meson decays

Figure 2.4 depicts the results of many measurements of the various CKM matrix elements, which overconstrain the UT and thus test the consistency of the SM and are sensitive to additional sources of CP violation from new physics. Decays of B^0 mesons to CP eigenstates, e.g. $B^0 \to J/\psi K_S^0$, provide the cleanest channel to study CP asymmetry in terms of the parameter $\sin 2\beta$ [25]. The uncertainty in the length of the left side of the UT, which complements the $\sin 2\beta$ measurement, is dominated by its least precisely known factor $|V_{ub}|$. In this dissertation we measure $|V_{ub}|$ through the decay channel $B \to \omega \ell \nu_\ell$.

At tree level,[10] weak decays of B mesons can occur via hadronic, semileptonic, or purely leptonic channels. In hadronic processes, complications arise from the fact that the quarks are bound by the strong force to color-singlet hadrons with non-perturbative quark-gluon interactions. In semileptonic and leptonic decays the effects of the strong interaction can be isolated into hadronic currents, so that, for the semileptonic case, the decay amplitude may be written as

$$\mathcal{M} = \frac{G_F}{\sqrt{2}} V_{qb} L_\mu H^\mu \tag{2.18}$$

where G_F is the Fermi constant and V_{qb} is the CKM matrix element appropriate to $b \to q$ transitions [26]. The leptonic and hadronic currents are given by

$$L^\mu = \bar{\psi}_\ell \gamma^\mu (1 - \gamma^5) \psi_\nu \tag{2.19}$$

[10] Tree level means to lowest order in perturbation theory.

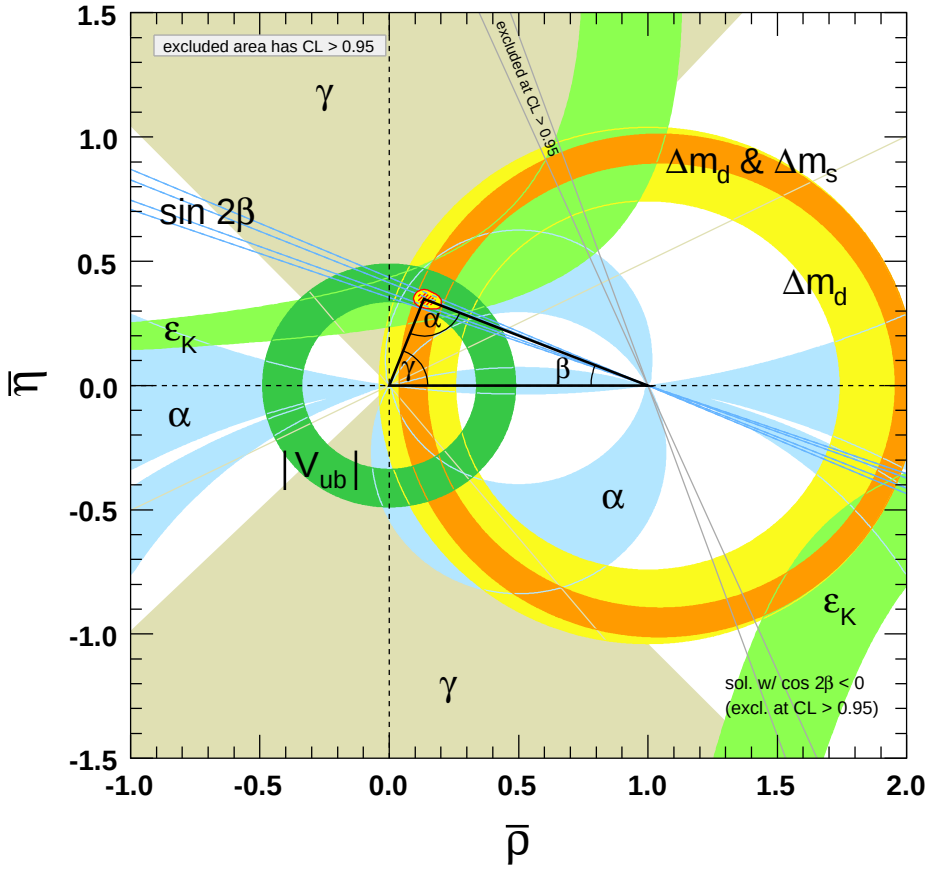

Figure 2.4: Constraints on the UT from various measurements. The shaded areas have 95% confidence level [14].

$$H^{\mu} = \langle f | \, \bar{q}\gamma^{\mu}(1-\gamma^{5})b \, | B \rangle \tag{2.20}$$

where $\bar{\psi}$ and ψ are the usual Dirac spinors, b ($\bar{q}$) is the fermion field annihilation (creation) operator for the b (q) quark, and $|B\rangle$ and $|f\rangle$ refer to the initial and final hadronic states, respectively. Calculation of the hadronic currents is challenging, since the matrix elements have to be taken between the physical final hadronic states, which contain non-perturbative strong interaction contributions, rather than between free quarks. These difficult-to-calculate quantities are typically absorbed into a set of Lorentz-invariant *form factors*, which describe the probability of having a particular meson in the final state. Effective field theory methods are used to separate non-perturbative long-distance contributions (the eventual hadronization of the quarks) from the short distance part of the decay (the weak transition of the b quark), which can be treated perturbatively.

The magnitude of V_{ub} is most accessible through the charmless semileptonic decay $b \to u\ell^{-}\bar{\nu}_{\ell}$ — or, in terms of observable hadrons, $B \to X_u \ell \nu_{\ell}$, where X_u is one or more charmless particles. When a specific final state meson X_u is explicitly reconstructed, the decay is said to be *exclusive*, as opposed to *inclusive* measurements, where all possible final states are considered and the kinematics of an event are used to distinguish the desired decay mode from other transitions. These methods complement each other due to the different theoretical uncertainties involved.

2.2.1 Inclusive charmless decays

In an inclusive approach, all possible final hadronic states X_u are considered, ignoring the details of the indivdual decay chains that contribute to the semileptonic rate. For an inclusive process, it suffices to consider only the short distance part of the decay, with the subsequent hadronization taking place with unit probability. This is known as parton-hadron duality. Due to the relative massiveness of the lightest charmed final state hadron (the D meson), the kinematic spectra of charmed and charmless semileptonic B decays differ significantly. In order to suppress large background contributions

from CKM-favored $B \to X_c \ell \nu_\ell$ transitions, one typically takes advantage of this fact by measuring the partial decay rate in regions of phase space kinematically not accessible to charmed transitions. Whereas the total inclusive decay rate can be calculated with good precision (less than 5% uncertainty) using Heavy Quark Expansion[11] (HQE) [28], HQE convergence is poor in the regions just mentioned, requiring the introduction of a non-perturbative *shape function* [29]. The shape function describes the distribution of the light-cone momentum of the b quark inside the B meson and is a universal property of B mesons to leading order; it can thus be measured through other processes, such as $B \to X_s \gamma$ [30], and the results applied to the calculation of the partial $B \to X_u \ell \nu_\ell$ decay rate.

2.2.2 Exclusive charmless decays

Exclusive charmless semileptonic decays offer a complementary means of determining $|V_{ub}|$. Experimentally, the specification of the final state provides better background rejection at the expense of lower yields as compared with inclusive decays. Theoretically, the calculation of the form factors is challenging, but brings in a different set of uncertainties from those encountered in inclusive decays: at lowest order in perturbation theory, the transition amplitude factorizes completely into leptonic and hadronic parts, with form factors characterizing the non-perturbative strong interaction effects in the hadronic matrix elements.

Typical semileptonic approaches fall into three basic categories:

- Charged lepton momentum endpoint measurements, typically limited to regions above the kinematic charm threshold, where theoretical uncertainties are large [31].

- Neutrino reconstruction techniques, where the missing momentum is recovered,

[11] A systematic expansion in inverse powers of the b-quark mass, based on the Operator Product Expansion framework [27].

allowing the determination of the momentum transfer q^2 and providing additional background rejection [32].

- *Tagged* measurements, in which the other B meson in the event is fully reconstructed, making the full range of signal-side variables available [33]. Tagged analyses typically suffer from low statistics, but offer better signal discrimination, as compared to untagged approaches.

A summary of $|V_{ub}|$ measurements using different techniques is shown in Fig. 2.5. The average is computed using only inclusive measurements at the B-factories. The exclusive measurements are all less than the inclusive ones; this could be due to dominant uncertainties coming from the limited knowledge of form factors. Figure 2.6 shows more current results of exlusive measurements of $|V_{ub}|$.

2.3 Hadronic form factors

As mentioned before, calculation of the hadronic currents is typically approached by introducing form factors; the properties of the final state meson dictate which technique may be used to calculate these hadronic form factors. For a meson containing one heavy and one light quark, HQE is a powerful tool for handling certain QCD calculations, including form factor calculations. For charmless semileptonic decays with two light quarks in the final state, HQE does not apply. Since this dissertation is concerned with the exclusive charmless semileptonic decay channel $B \to \omega \ell \nu_\ell$, other techniques must be applied.

2.3.1 Form factors and helicity amplitudes

A schematic representation of the decay $B \to \omega \ell \nu_\ell$ is given by the Feynman diagram of Fig. 2.7, where the initial and final state quarks are bound in a B and an ω meson, respectively. For a transition from a pseudoscalar B meson to a final state with

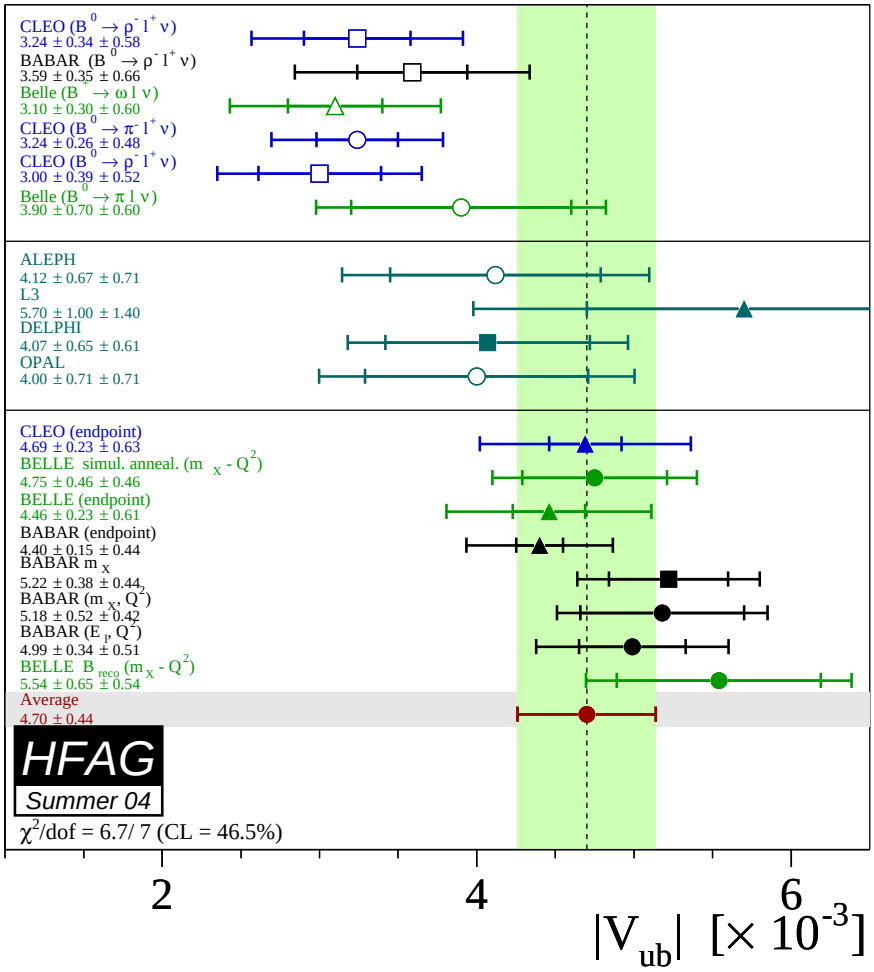

Figure 2.5: Current measurements and world average (as of summer 2004) of $|V_{ub}|$, as obtained by HFAG [9]. The results are from exclusive (top) and inclusive (bottom) measurements at B-Factories, and from inclusive measurements at LEP (middle).

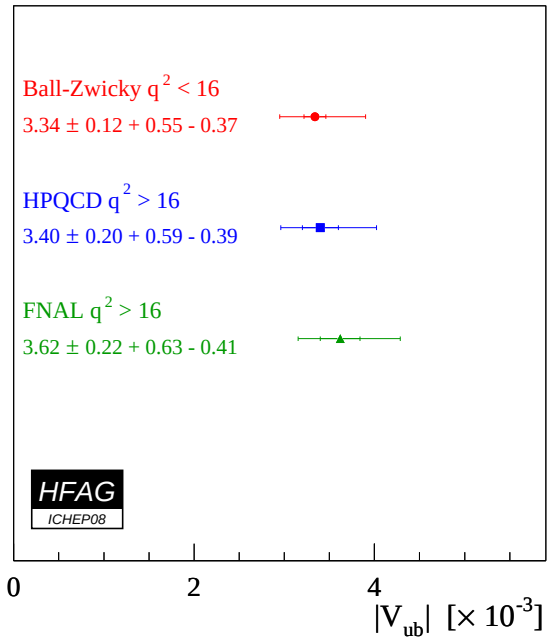

Figure 2.6: Exclusive measurements (as of summer 2008) of $|V_{ub}|$, as obtained by HFAG [9]. The quoted errors on $|V_{ub}|$ are experimental and theoretical, respectively.

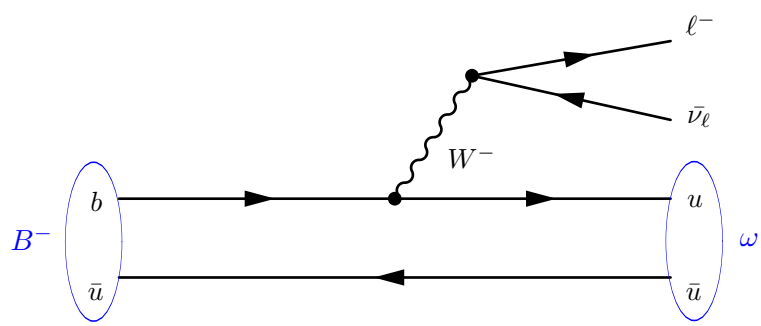

Figure 2.7: Tree level Feynman diagram for the weak semileptonic decay $B^- \to \omega \ell^- \bar{\nu}_\ell$.

a single vector meson (like the ω), the hadronic current (2.20) has both vector V_μ and axial vector A_μ contributions and may be written in terms of the polarization vector ϵ^μ of the vector meson as

$$\langle V(p_V,\epsilon)|\,(V-A)_\mu\,|B(p_B)\rangle = \epsilon_{\mu\nu\rho\sigma}\epsilon^{*\nu}p_B^\rho p_V^\sigma \frac{2V(q^2)}{m_B+m_V} - \mathrm{i}\epsilon^*_\mu(m_B+m_V)A_1(q^2)$$
$$+\,\mathrm{i}(p_B+p_V)_\mu(\epsilon^* p_B)\frac{A_2(q^2)}{m_B+m_V} + \mathrm{i}q_\mu(\epsilon^* p_B)\frac{2m_V}{q^2}[A_3(q^2)-A_0(q^2)] \quad (2.21)$$

where p_B (m_B) and p_V (m_V) are the four-momenta (masses) of the B meson and the vector meson, respectively, $q = p_B - p_V$ is the momentum transfer, and $V(q^2)$ and $A_i(q^2)$ are the four semileptonic form factors [34]. It is convenient to express the decay amplitude in terms of a helicity basis (effectively that of the virtual W). The three[12] helicity amplitudes are given by [35]:

$$H_\pm(q^2) = (m_B+m_V)\left[A_1(q^2) \mp \frac{2m_B|\boldsymbol{p}_V|}{(m_B+m_V)^2}V(q^2)\right] \quad (2.22a)$$

$$H_0(q^2) = \frac{m_B+m_V}{2m_V\sqrt{|q^2|}} \times \left[(m_B^2-m_V^2-q^2)A_1(q^2) - \frac{4m_B^2|\boldsymbol{p}_V|^2}{(m_B+m_V)^2}A_2(q^2)\right] \quad (2.22b)$$

where $\boldsymbol{p}_V$ is the vector meson three-momentum. The differential decay rate $\mathrm{d}\Gamma$, in the limit of a massless charged lepton, is then given by

$$\frac{\mathrm{d}\Gamma(B\to V\ell\nu)}{\mathrm{d}q^2\mathrm{d}\cos\theta_{W\ell}} = |V_{ub}|^2\frac{G_F^2|\boldsymbol{p}_V|q^2}{128\pi^3 m_B^2}\times \left[(1-\cos\theta_{W\ell})^2\frac{|H_+|^2}{2} + (1+\cos\theta_{W\ell})^2\frac{|H_-|^2}{2} + \sin^2\theta_{W\ell}|H_0|^2\right] \quad (2.23)$$

where $\theta_{W\ell}$ is the angle between the direction of the charged lepton in the virtual W rest frame and the direction of the W in the B rest frame. Understanding the form factors (and thus the helicity amplitudes) is critical to the extraction of $|V_{ub}|$ from measured branching fractions as well as the realistic simulation of the data.

[12] Only three out of the four original form factors are independent.

2.3.2 Form factor calculations

A number of QCD calculation schemes for the form factors exist:

- Quark models like ISGW [36] calculate hadronic current matrix elements at one of the extreme values $q^2 = 0$ or $q^2 = q^2_{\text{max}}$ by postulating forms for the meson wavefunctions, and then extrapolate the q^2 dependence by a phenomenological ansatz. The ISGW2 model [37] is the default *BABAR* model for the simulation of resonant hadronic states for all charmless semileptonic decays.

- Lattice QCD (LQCD) involves the formulation of an effective action on a discrete space-time lattice, and Monte Carlo evaluation of resulting path integrals [13, chapter 16]. LQCD calculations are most reliable in the high q^2 regime, since at small values of q^2 the de Broglie wavelength of the final state meson is large and may interfere with the finite volume of the lattice.

- The method of light-cone sum rules (LCSR) [38, 39] provides a non-perturbative approach to form factor calculations in the low to intermediate q^2 range, in which suitable correlation functions can be expanded around the light cone [34]. QCD sum rules relate these functions to form factors and other parameters, which can be determined empirically or calculated by other means.

Unitarity and analyticity requirements can be used to constrain the shape of the form factors and thus their interpolations between different q^2 regions [40, 41].

2.4 Extraction of $|V_{ub}|$ from $B \to \omega\ell\nu$

Since the differential decay rate 2.23 is proportional to $|V_{ub}|$, it is straightforward to extract $|V_{ub}|$ from the measured branching fraction

$$\mathcal{B}(B \to \omega\ell\nu) = \frac{\Gamma(B \to \omega\ell\nu)}{\Gamma(B \to \text{ anything})} = \Gamma(B \to \omega\ell\nu) \cdot \tau_B \tag{2.24}$$

where τ_B is the B meson lifetime. In terms of a partial branching fraction $\Delta\mathcal{B}$ measured in a given q^2 range, $|V_{ub}|$ can be extracted with the following relation:

$$|V_{ub}| = \sqrt{\frac{\Delta\mathcal{B}(B \to \omega\ell\nu)}{\tau_B \Delta\zeta}} \tag{2.25}$$

where $\Delta\zeta$ is the reduced partial decay rate (taken over the same q^2 range as $\Delta\mathcal{B}$) calculated by means of some theoretical form factor model:

$$\Delta\zeta = \frac{1}{|V_{ub}|^2} \int_{q^2_{\mathrm{min}}}^{q^2_{\mathrm{max}}} \frac{\mathrm{d}\Gamma_{\mathrm{FF}}}{\mathrm{d}q^2} \mathrm{d}q^2 \tag{2.26}$$

Chapter 3

The Detector

3.1 The *BABAR* experiment

The primary physics goal of the *BABAR* experiment is the systematic study of *CP*-violating asymmetries in the decay of neutral B mesons to *CP* eigenstates. Secondary goals include precision measurements of decays of bottom and charm quark mesons and of τ leptons, as well as branching fractions of rare B meson decays and other aspects of the Standard Model. It operates at the Positron-Electron Project II (PEP-II) asymmetric-energy e^+e^- storage ring of the SLAC National Accelerator Laboratory in Menlo Park, California.

To maximize the production of B mesons, the PEP-II collider operates at a center-of-mass (CM) energy of 10.58 GeV, the mass of the $\Upsilon(4S)$ resonance. The $\Upsilon(4S)$ decays almost exclusively to $B\overline{B}$ pairs and thus provides an ideal laboratory for the study of B mesons. The small Q-value of the $\Upsilon(4S) \to B\overline{B}$ decay results in B mesons almost at rest in the CM frame.

3.2 The linear accelerator and PEP-II

The PEP-II B Factory is an e^+e^- collider fed by a 3.2 km linear accelerator (linac) using radio-frequency (RF) cavity resonators. It consists of a pair of storage rings of 2.2 km circumference which collide a beam of 9.0 GeV electrons in the high-energy ring (HER) with a counter-circulating beam of 3.1 GeV positrons in the low-energy

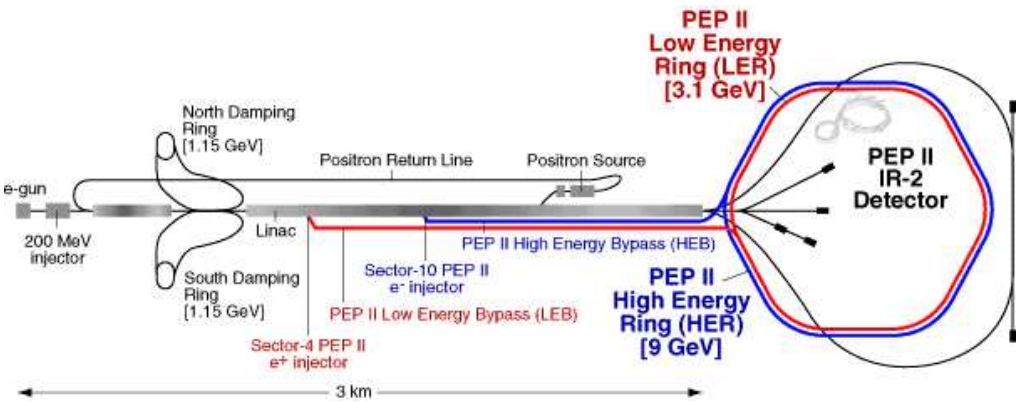

Figure 3.1: Schematic of the linear accelelerator and PEP-II.

ring (LER). Its design luminosity of 3×10^{33} cm^{-2}s^{-1} at the CM energy of 10.58 GeV was exceeded in 2001, and by 2006, peak luminosities above 12×10^{33} cm^{-2}s^{-1} were recorded. The asymetry in the beam energies enables the study of the decay time difference of the two B mesons: the $\Upsilon(4S)$ system is generated with a Lorentz boost of $\beta\gamma = 0.56$ with respect to the laboratory frame. This translates a difference in the B meson lifetimes (important for the measurement of CP-violation effects) into a spatial separation of their decay verteces that is within the resolving power of the vertex tracking system.[1]

The linac consists of an electron gun plus injector, a pre-accelerator, two damping rings, the main linac, and a positron source. A schematic representation of the linac and the PEP-II collider is given in Fig. 3.1. The electrons are produced from a filament by thermal emmision and fed into the linac by a static electric field, where they are accelerated to approximately 1 GeV before they enter the north damping ring. In the damping ring, the emittance[2] of the beam is reduced (damped) via synchrotron radiation and subsequent longitudinal acceleration. The damped beam is returned to the linac and accelerated to the collision energy of 9.0 GeV.

For positron production, half of the electrons are accelerated almost the entire

[1] With the given boost and a B meson lifetime of about 1.5 ps, the mean separation is ≈ 250 μm.
[2] The *emittance* is a measure of a beam's extension and divergence.

length of the linac to 30 GeV and steered into a tungsten target. Positrons from the resulting electromagnetic shower are focused and returned to the source end of the linac for damping in the south damping ring and subsequent acceleration to 3.1 GeV.

Electrons and positrons are injected into PEP-II at collision energies. As they circulate in their two separate storage rings, they are bent and focused by magnets and accelerated by RF cavities to compensate for energy loss due to synchroton radiation. As they enter the interaction region, the beams are focused and steered into head-on collision by a pair of dipole magnets (labeled B1 in Fig. 3.2) and a series of quadrupole magnets (Q1, Q2, and Q4 in Fig. 3.2). Head-on collisions are made possible by the asymmetric beam energies, which allow for magnetic separation of the beams. After the collision, the beams are quickly separated to avoid spurious collisions between out-of-phase bunches, and steered back into their respective rings. Some of the design specifications of the PEP-II storage rings are summarized in Table 3.1.

3.3 The *BABAR* detector

The study of B decays typically involves the partial or full reconstruction of the decay chain down to the final state particles: charged hadrons ($\pi^{\pm}$, $K^{\pm}$, p), neutral hadrons (π^0, K^0_S, K^0_L, n), charged leptons ($e^{\pm}$, $\mu^{\pm}$), and photons (γ). Intermediate states are reconstructed as composites of the final state particles. Reconstruction of the decay chain and the decay kinematics is rarely unambiguous, and requires efficient and accurate particle identification (PID) over a wide kinematic range. The following performance parameters were identified to meet these and other requirements:

- Efficient tracking of particles with transverse momentum (p_T) between ~ 60 MeV/c and ~ 4 GeV/c, with p_T-resolution of $\sim 0.5\%$.
- Detection of photons and neutral pions with energies between ~ 20 MeV and ~ 5 GeV, with energy (angular) resolution of the order of a few % (mrad).

Table 3.1: Selected PEP-II design parameters [42].

Parameter	**Symbol**	**Units**	**LER**	**HER**
Energy/particle	E	GeV	3.1	9.0
Beam current	I^+, I^-	A	2.16	0.75
Number of bunches	N_b		1658	
Bunch spacing	$2\lambda_{\mathrm{RF}}$ [a]	m/ns	1.26/4.2	
Bunch length	σ_{s0}	mm	9.87	11.5
Revolution frequency	f_{rev}	kHz	136.3	
RF frequency	f_{RF}	MHz	476.0	
Harmonic number	h		3492	
RF cavities	N_C		6	20
RF power	P_{RF}	MW	1.85	3.73
Synchrotron frequency	f_s	kHz	4.55	6.12
Betatron frequencies	f_x/f_y	kHz	77.7/87.5	84.1/86.8
Transverse emittances	$\epsilon_{x0}/\epsilon_{y0}$	nm·rad	64/2.6	48/1.9
Longitudinal emittance	ϵ_{s0}	μm·rad	7.59	7.06
IP beta functions	β_x^*/β_y^*	m	0.50/0.015	
IP rms sizes	σ_x^*/σ_y^*	μm	157/4.70	
IP rms divergences	$\sigma_x^{'*}/\sigma_y^{'*}$	μrad	314	
Luminosity	L	$\mathrm{cm}^{-2}\mathrm{s}^{-1}$	3×10^{33}	

[a] λ_{RF} is the bucket spacing (every other bucket is filled).

- Resolution of the vertex of fully reconstructed B decays of 80 μm along the z-axis and 100 μm in the transverse plane.

In order to maximize the geometric acceptance for the boosted $\Upsilon(4S)$ decays, the whole detector is offset relative to the beam-beam interaction point (IP) by 370 mm in the direction of the lower energy beam (less for the SVT), and most subsystems have a somewhat asymmetric design. To meet the above mentioned criteria, the *BABAR* detector consists of five subdetectors which provide measurements of particle trajectories and their main interactions with matter: ionization, emission of Čerenkov radiation, and production of electromagnetic (and hadronic) showers. The six[3] major subsystems and their major functions are (in order of increasing distance from the interaction region):

- Silicon Vertex Tracker (SVT): Precise tracking of charged particles near the interaction region; measurement of ionization energy loss.
- Drift Chamber (DCH): Precise measurements of momenta and trajectories of charged particles, and measurement of ionization energy loss $\mathrm{d}E/\mathrm{d}x$ for charged particle identification (PID).
- Detector of Internally Reflected Čerenkov radiation (DIRC): Measurement of charged particles' velocities for PID.
- Electromagnetic Calorimeter (EMC): Detection and energy measurement of photons, and electron identification.
- The superconducting coil, which provides a 1.5 T solenoidal magnetic field.
- Instrumented Flux Return (IFR): Detection and identification of muons and neutral hadrons.

[3] including the magnet

Table 3.2: Production cross sections for the principal physics processes at $E_{\mathrm{CM}} = 10.58$ GeV [43]. The e^+e^- cross section is the effective cross section expected within the experimental acceptance.

Event type $e^+e^- \to$	Cross section (nb)
$b\overline{b}$	1.05
$c\overline{c}$	1.30
$s\overline{s}$	0.35
$u\overline{u}$	1.39
$d\overline{d}$	0.35
$\tau^+\tau^-$	0.94
$\mu^+\mu^-$	1.16
e^+e^-	~ 40

All detector components except for the IFR are embedded inside the 1.5 T magnetic field of the superconducting solenoid; the curvature of a charged track in this magnetic field allows determination of its charge and momentum. A schematic of the detector is shown in Figures 3.2 and 3.3. The polar angle coverage extends to 350 mrad in the forward direction and 400 mrad in the backward direction.

Since the average momentum of charged particles produced in B decays is less than 1 GeV/c, the precision of the measured track parameters is heavily influenced by multiple scattering. Similarly, the detection efficiency and energy resolution of low energy photons are severely impacted by material in front of the calorimeter. Thus, special care has been taken to keep material in the active region of the detector to a minimum. The distribution of material in the various detector systems is shown in Fig. 3.4 in units of radiation lengths X_0. Each curve indicates the material that a particle traverses before it reaches the first active element of a specific subsystem.

Most of the data are recorded at the peak of the $\Upsilon(4S)$ resonance, referred to as *on-peak* data. Cross sections for the main processes active at the $\Upsilon(4S)$ resonance are summarized in Table 3.2. The production of quark pairs other than $b\overline{b}$ or of lepton pairs is usually referred to as *continuum* production. Continuum production rates exceed $b\overline{b}$

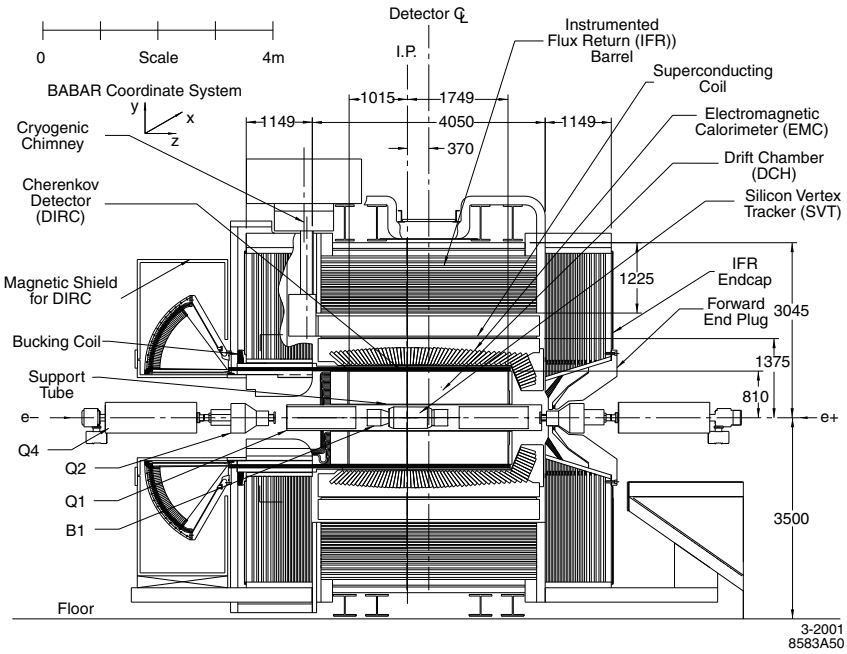

Figure 3.2: Longitudinal view of the *BABAR* detector.

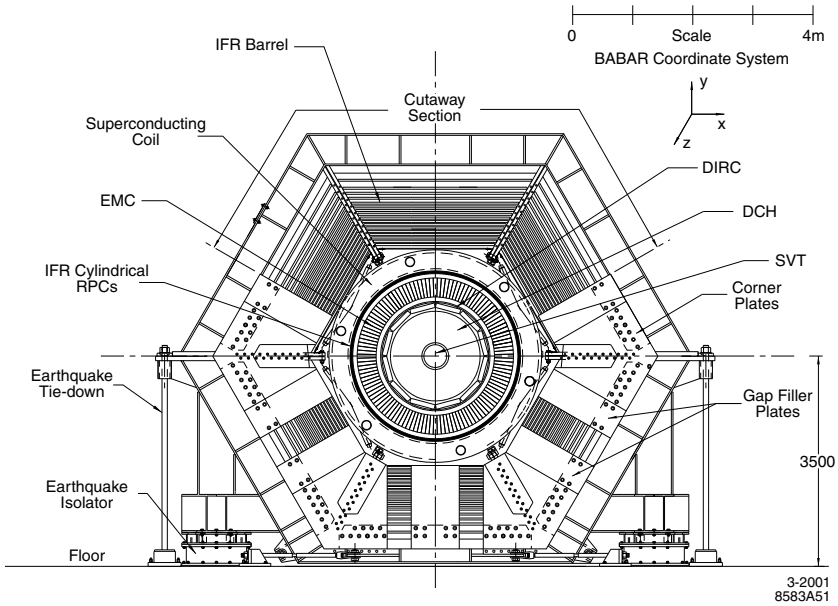

Figure 3.3: Transverse cross-section of the *BABAR* detector.

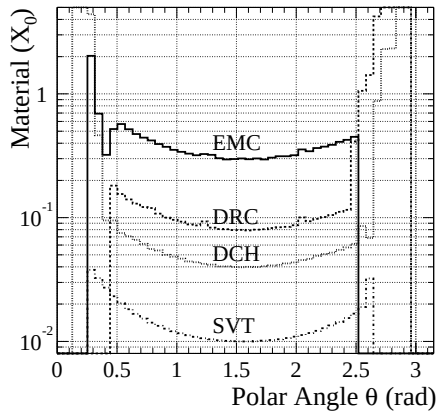

Figure 3.4: Amount of material (in units of X_0) in the *BABAR* detector.

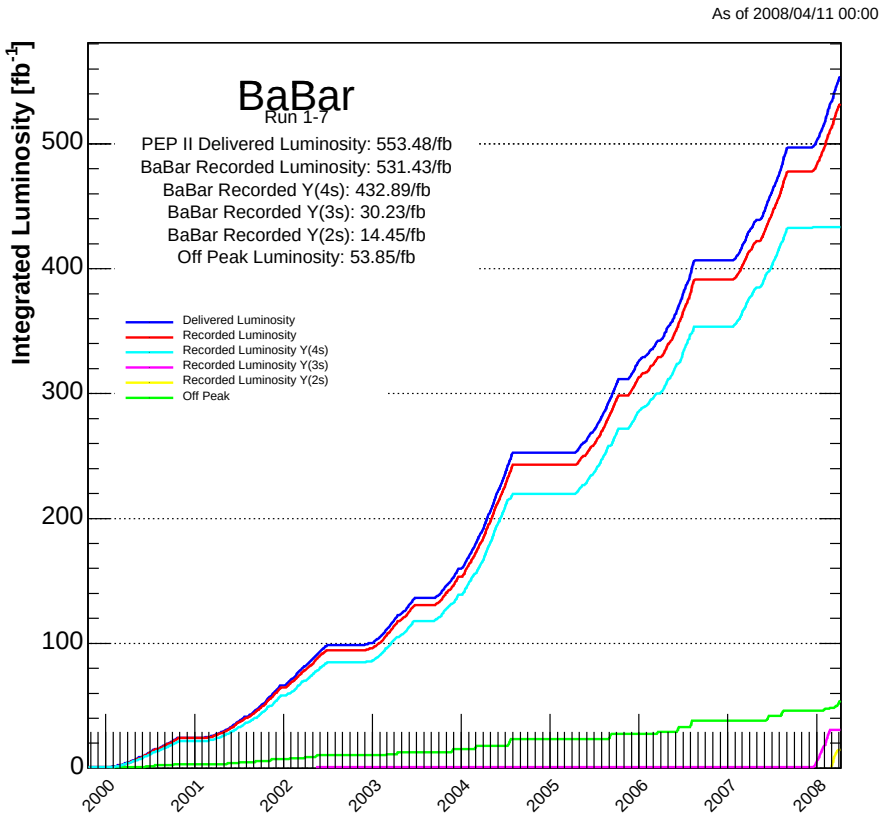

Figure 3.5: Integrated luminosity delivered by PEP-II and recorded by *BABAR*.

production rates at the resonance, with Bhabha scattering ($e^+e^- \to e^+e^-$) being the most dominant one. In order to allow studies of the non-resonant background, about 10% of the data are taken at a center-of-mass energy 40 MeV below the $\Upsilon(4S)$ mass, where the $B\overline{B}$ cross-section is nil, referred to as *off-peak* data. During typical operation, PEP-II delivered several hundred pb^{-1} of integrated luminosity per day, of which 95% was recorded by *BABAR*. A total of 433 fb^{-1} of data were recorded[4] at the $\Upsilon(4S)$ peak from October 1999 to October 2007, which — given the $e^+e^- \to \Upsilon(4S)$ cross section of about 1.05 nb[5] — corresponds to 465×10^6 $B\overline{B}$ pairs [44]. Figure 3.5 shows the luminosity delivered by PEP-II and recorded by the *BABAR* detector during the entire period of operation.

The following sections give an overview of the various *BABAR* detector components and their performance; a more detailed description of the detector may be found elsewhere [45]. Table 3.3 at the end of this chapter summarizes and compares the coverage, segmentation, and performance of the individual *BABAR* detector systems.

3.3.1 SVT

The SVT is the innermost *BABAR* detector subsystem, designed for the detection of charged particles and the precise measurement of their trajectories and decay vertices near the interaction point. Because of the presence of the 1.5 tesla magnetic field from the solenoid, the SVT must also provide standalone tracking for low transverse momentum (50–120 MeV/c) particles, which cannot be measured reliably by the DCH.

The SVT consists of five concentric cylindrical layers (at least three are necessary to determine the circular projection of a helix onto the transverse plane) of double-sided silicon strip sensors around the beampipe, with a radius of 3.2 cm for the innermost and 14.4 cm for the outermost layer. The inner three layers are organized into six straight

[4] Recorded luminosity is computed online from the number of luminosity triggers produced by the L3 trigger (see Section 3.3.6).

[5] not including the production of $b\bar{b}$ jets, for which the b and $\bar{b}$ quarks don't form an intermediate bound state.

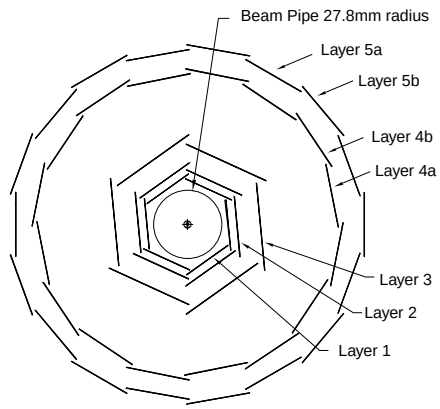

Figure 3.6: Transverse cross section of the SVT.

modules, whereas layers four and five contain 16 and 18 modules with tapered ends to increase the crossing angle for tracks near the edges of the acceptance region and to minimize the amount of silicon needed for the desired solid angle coverage. The outer two layers are located farther from the beam axis to better link SVT hits with DCH hits. This is shown in Fig. 3.6 and 3.7.

Each module consists of several 300 μm thick double-sided planar sensors (340 total), with ϕ strips running parallel to the beam axis on one side, and z strips running transverse to it on the other side. When a charged particle passes through the silicon, electron/hole pairs are created, separated by the applied voltage of 35–45 V, amplified and read out. The resolution depends on track angle and varies between layers. At normal incidence, the z-resolution changes from 15 μm for inner layers to 35 μm for outer layers; the ϕ-resolution varies correspondingly from 10 to 20 μm, see Fig. 3.8. The acceptance angle is 350 mrad in the forward direction and 520 mrad in the backward direction, corresponding to geometrical acceptance of 90% of the solid angle in the CM system. Within this acceptance region, the SVT achieves a total tracking efficiency of 97%. The ten layers of the SVT (counting each side separately) also provide ionization energy loss ($\mathrm{d}E/\mathrm{d}x$) measurements to supplement those provided by the DCH; a 2σ separation between kaons and pions can be achieved up to momenta of 500 MeV/c, and

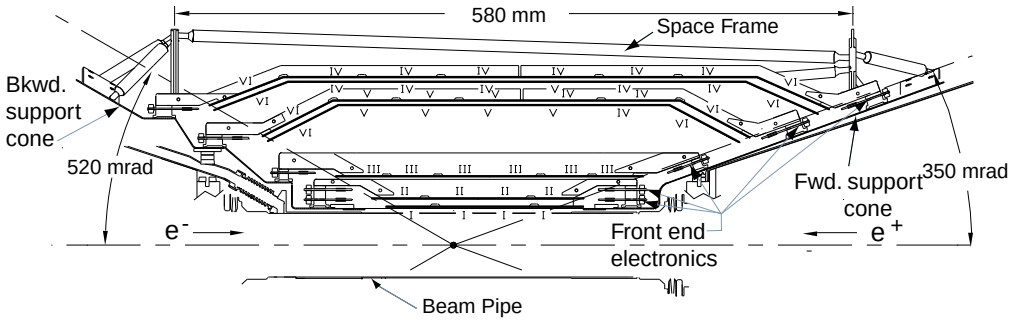

Figure 3.7: Longitudinal cross section of the SVT.

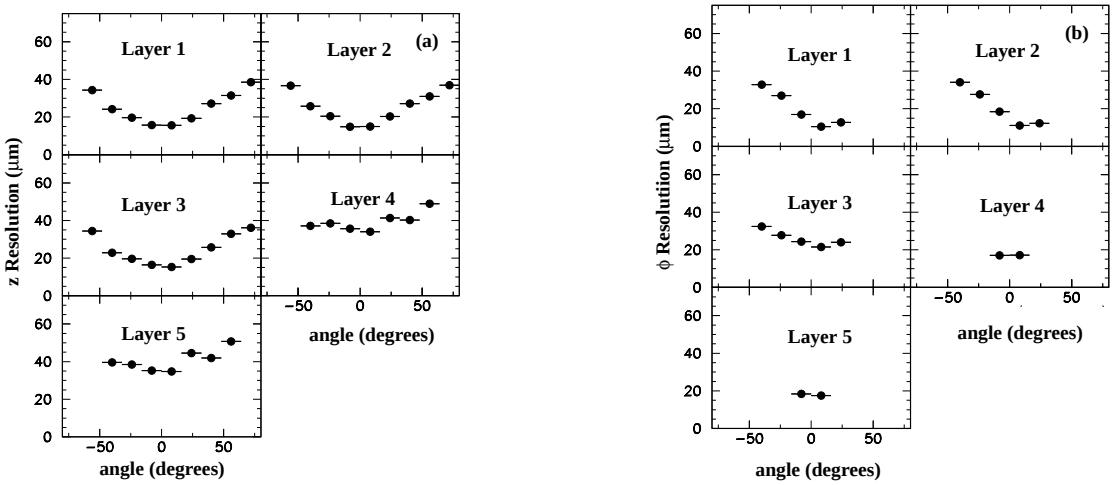

Figure 3.8: SVT hit resolution in the z (left) and ϕ (right) coordinate, as a function of track incident angle, plotted separately for each layer.

between kaons and protons beyond 1 GeV/c.

3.3.2 DCH

The drift chamber is the detector's primary tracking device (complemented by the SVT), designed for the detection of charged particles and measurement of their momenta, as well as the reconstruction of the decay vertices of long-lived particles such as K_S^0 and Λ^0, which decay mostly outside the SVT. In addition, the DCH provides particle identification (PID) through measurement of a particle's energy loss $\mathrm{d}E/\mathrm{d}x$ as it passes through the DCH. This capability complements the DIRC in the barrel region, whereas in the extreme forward and backward directions, and for low-momentum particles, the DCH is the main PID device.

The DCH is a 280 cm long cylinder surrounding the SVT, with inner radius of 23.6 cm and outer radius of 80.9 cm, as depicted in Fig. 3.9. Because of the asymmetric beam energies, its center is offset by 37 cm from the IP, leading to a polar angle acceptance of $17.2^\circ < \theta < 152.6^\circ$ in the laboratory frame. The volume is divided into 7104 hexagonal drift cells running along the length of the DCH in 40 concentric layers, which are grouped

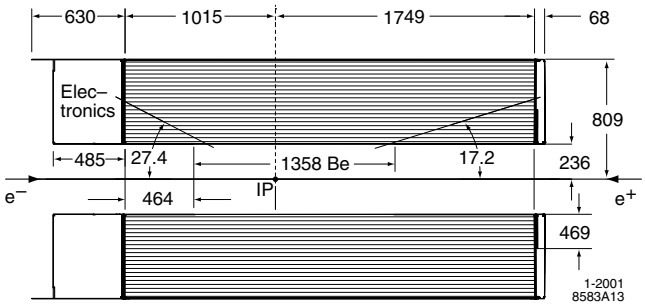

Figure 3.9: Longitudinal cross section of the DCH.

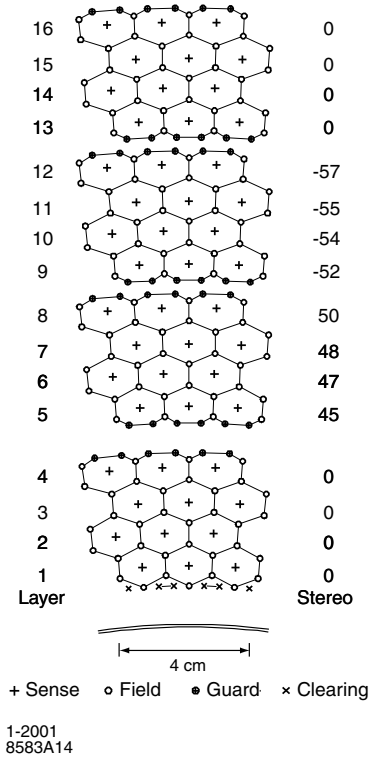

Figure 3.10: Schematic layout of the drift cells for the four innermost superlayers.

by four into ten superlayers. Four *axial* (A) superlayers run parallel to the z-axis, whereas six *stereo* superlayers are strung with a small angular offset with respect to the z-axis - alternating with positive (U) and negative (V) angles - to enable the extraction of additional longitudinal position information, with a resolution of less than 1 mm. The ten superlayers are arranged in the pattern AUVAUVAUVA, with stereo angles increasing radially from ± 45 mrad to ± 76 mrad. The entire volume is filled with a mixture of helium (80%) and isobutane (20%); helium was chosen over argon to minimize mutiple scattering.

Each drift cell has dimensions of 11.9 mm (radial) and 19.0 mm (azimuthal) and consists of a central sense wire surrounded by six field-shaping wires, which are shared with adjacent cells. The 20 μm diameter tungsten-rhenium sense wires are gold-plated and kept at a positive voltage of $\sim$ 1930 V, and the gold-plated aluminum field wires are held at ground potential. Cells on the boundary of a superlayer have two gold-coated aluminum guard wires, held at 340 V, to ensure uniform gain of boundary and inner cells. Two sets of clearing wires run along the DCH's inner and outer walls to collect charges generated by photon conversion. Figure 3.10 shows a schematic layout of the drift cell design and layer arrangement.

A charged particle passing through the DCH ionizes the gas, thereby losing some of its energy; the amount of energy loss is related to the amount of charge released in the gas. The ionized gas molecules within a cell drift towards a field wire and the resulting free electrons are accelerated toward a sense wire, colliding with and ionizing more gas molecules along the way and thus creating an avalanche of free electrons, with a typical avalanche gain of 5×10^4. The free electrons quickly achieve a constant terminal velocity, which allows the extraction of spatial information about a particle's path through a cell from ion drift times. Figure 3.11 shows the relationship between the measured drift time and the drift distance as determined from samples of e^+e^- and $\mu^+\mu^-$ events. The resulting single cell position resolution as a function of the drift

distance, averaged over all cells in layer 18, is shown in Fig. 3.12.

The DCH is contained within the 1.5 T magnetic field of the superconducting solenoid, so that charged particles traverse it on a helical trajectory. A particle's transverse momentum p_T can be determined via its track curvature with a resolution given by

$$\sigma_{p_T}/p_T = (0.13 \pm 0.01)\% \cdot p_T + (0.45 \pm 0.03)\% \tag{3.1}$$

with p_T in GeV/c, where the constant term represents the multiple scattering limit (see Fig. 3.13). The average DCH tracking efficiency is 98% for $p_T > 200$ MeV/c and $\theta >$ 500 mrad, as shown in Fig. 3.14.

The ionization energy loss $\mathrm{d}E/\mathrm{d}x$ of a relativistic charged particle passing through matter is given by the Bethe-Bloch equation [46]; because it depends on the particle's velocity, it can be combined with knowledge of the particle's momentum (from its trajectory) to determine its mass and thus provide PID. Figure 3.17 compares $\mathrm{d}E/\mathrm{d}x$ measurements from the DCH, as inferred from the charge deposition in each cell, to their Bethe-Bloch predictions for six particle species. The $\mathrm{d}E/\mathrm{d}x$ resolution achieved by the DCH for low-momentum tracks ($p_T < 700$ MeV/c) is 7.5%, enabling an excellent pion/kaon separation.

3.3.3 DIRC

The Detector of Internally Reflected Čerenkov light (DIRC) is designed to provide PID for higher-momentum charged hadrons, supplementing the lower-momentum PID from the DCH. It is a new type of ring-imaging Čerenkov detector utilising the fact that angles are preserved upon total internal reflection. When a charged particle traverses a medium faster than the speed of light in that medium, it emits a light cone at the characteristic Čerenkov angle $\cos\theta_c = 1/(\beta n)$ with respect to its trajectory, which depends on the index of refraction n of the medium and the velocity $\beta = v/c$ of the

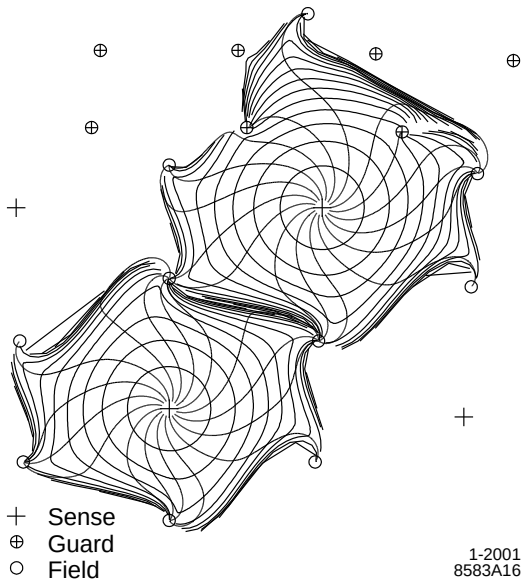

Figure 3.11: Contours of equal ion drift times in cells of layers 3 and 4 of an axial superlayer.

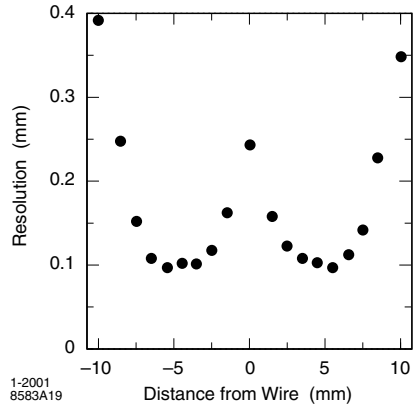

Figure 3.12: DCH position resolution as a function of drift distance for layer 18.

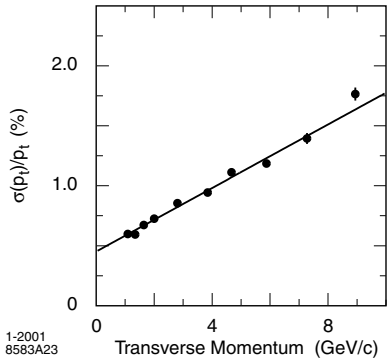

Figure 3.13: DCH resolution in the transverse momentum p_T.

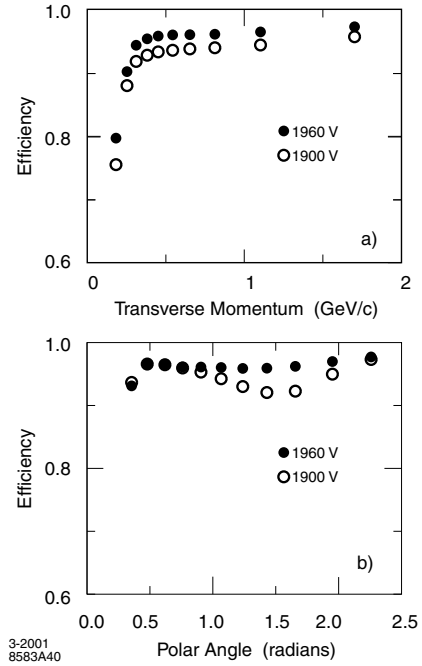

Figure 3.14: Track reconstruction efficiency in the DCH as a function of transverse momentum p_T (top) and polar angle ϕ (bottom).

particle. Combining the velocity with momentum information from the tracking system allows the particle's mass (and hence its type) to be determined.

The DIRC consists of the radiator barrel between the DCH and the EMC and the stand-off box (SOB) behind the rear IFR doors, see Fig. 3.15. The radiator consists of 144 bars of fused silica (quartz) with refractive index $n = 1.473$ (in the wavelength region from 300 to 600 nm), which function both as light guides and as a medium for Čerenkov radiation. Each bar is 1.7 cm thick, 3.5 cm wide, and 490 cm long, and is constructed by gluing four shorter bars end-to-end. Twelve bars each are grouped into twelve aluminum bar boxes, which are arranged in a dodecagonal barrel of 84 cm radius coaxial with the beampipe, extending along the entire length of the DCH and back through the IFR doors into the SOB, covering polar angles from 25.5° to 141.4° and 93% of the azimuth. For charged particles traversing the radiator with $\beta \lesssim 1$, some of the Čerenkov photons will always be captured by total internal reflection (regardless of the angle of incidence) and propagate along the bar. Only the rear end of the detector is instrumented with photon detectors to minimize interference with other detector systems (due to the beam energy asymmetry, particles are produced preferentially forward in the lab frame), so a mirror is placed at the front end of the bars. A fused silica wedge is glued at the backward end of the bars so that the lower image of the Čerenkov ring is reflected onto the upper image, reducing the size of the required detection surface by a factor of two.

At the DIRC imaging region on the backward end of the detector, Čerenkov photons exit the wedge and expand into the SOB filled with 6,000 liters of purified, deionized water with refractive index $n = 1.346$ similar to that of quartz. At the backplane of the SOB, the photons are collected by a dense array of 10,752 photomultiplier tubes (PMTs) of diameter 2.82 cm — divided into twelve sectors of 896 PMTs each, matching the twelve bar boxes — located 1.17 m from the ends of the silica bars, see Fig. 3.16. Except for the refraction at the fused silica/water boundary, the Čerenkov angle is preserved during the light transport process. Position and arrival-time of PMT signals

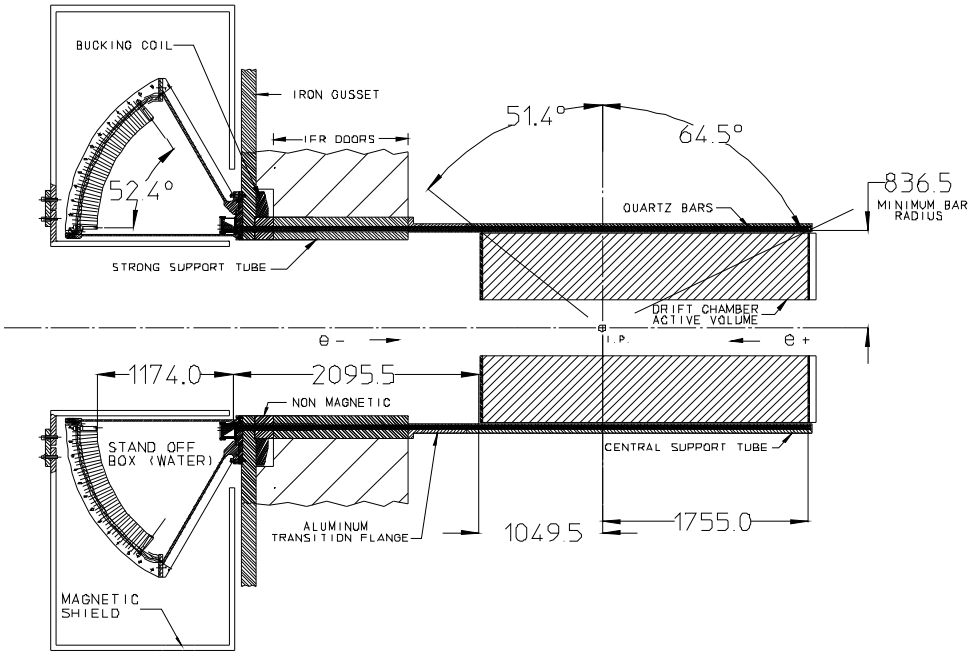

Figure 3.15: Longitudinal cross section of the DIRC.

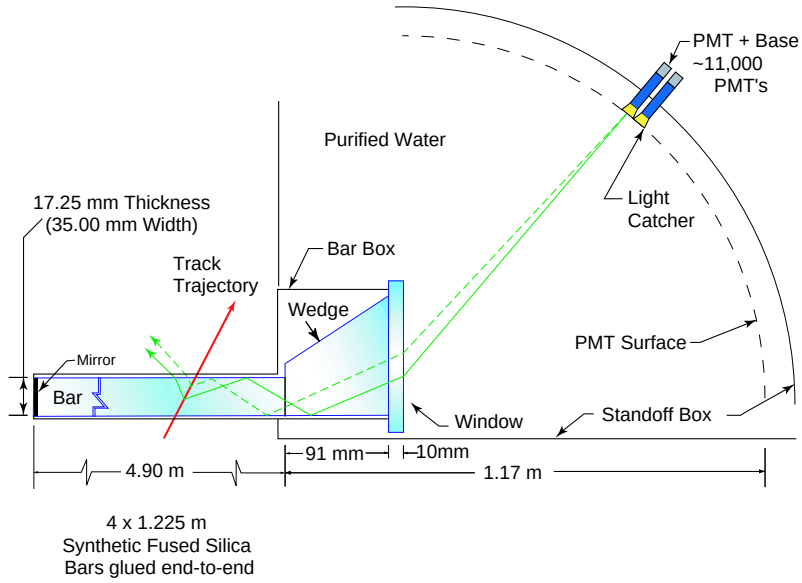

Figure 3.16: Schematics of the top half of the DIRC radiator barrel and imaging region.

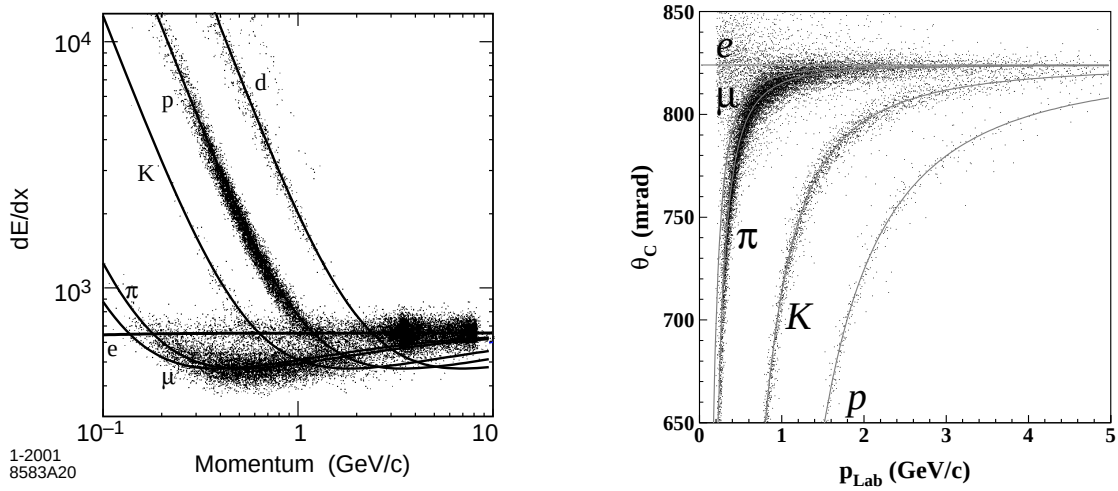

Figure 3.17: PID: Measurements of $\mathrm{d}E/\mathrm{d}x$ in the DCH (left), and of the Černkov angle θ_C in the DIRC (right), both as a function of track momentum. The lines represent predictions for several particle species.

recorded within the readout window of a given track are then combined with spatial information for that track obtained from the tracking system to calculate the Čerenkov angle and resolve the forward-backward and wedge ambiguities. The DIRC achieves single photon Čerenkov angle resolution of about 10.2 mrad, which translates to an average resolution on the track Čerenkov angle of 2.5 mrad. At the high-momentum end of the DIRC's functional window (around 4.0 GeV/c), the difference in the Čerenkov angle of pions and kaons is 3.5 mrad, as shown in Fig. 3.17. At this momentum, the DIRC is able to separate the two species to around 3σ. This separation power increases for lower momenta up to $\sim 8\sigma$ at 2.0 GeV/c.

3.3.4 EMC

The EMC is designed to measure electromagnetic showers with excellent efficiency and good energy and angular resolution over the energy range from 20 MeV to 9 GeV, allowing the detection of photons from π^0 and η decays as well as from electromagnetic and radiative processes. The EMC is also the primary source for electron identification

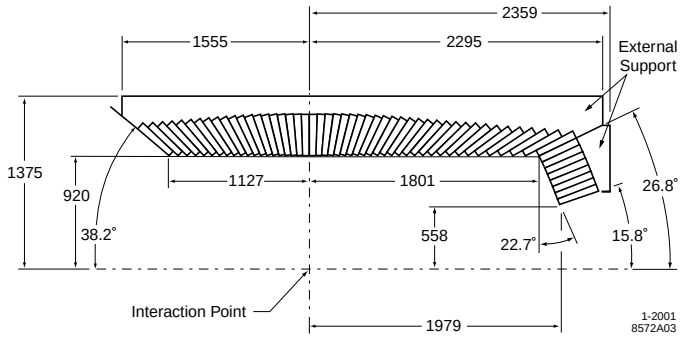

Figure 3.18: Longitudinal cross section of the EMC, indicating the arrangement of the 56 crystal rings. Only top half is shown.

through information about the shape of the electromagnetic showers (hadrons that interact in the calorimeter produce a shower that is much more spread out than that originating from an electron). Incident photons and electrons induce photon conversion ($\gamma \rightarrow e^+e^-$) and bremsstrahlung radiation ($e^\pm \rightarrow e^\pm\ \gamma$), leading to a cascading shower of low-energy particles which are eventually absorbed by the EMC's medium, so that all of the initial particle's energy is deposited in the calorimeter and re-emitted as visible scintillation light.

The calorimeter consists of 6580 thallium-doped (0.1%) cesium iodide (CsI(Tl))crystals which feature a small Moliére radius ($R_m = 3.8$ cm) for good angular resolution and a short radiation length (1.85 cm) to allow for full shower containment with a relatively compact design. Additionally, the high light yield and the emission spectrum of CsI(Tl) permit efficient use of silicon photodiodes which operate well in high magnetic fields.

The EMC consists of a cylindrical barrel located between the DIRC radiator barrel and the magnet cryostat, and a conic forward end-cap, which together cover a polar angle region between $15.8° < \theta < 141.8°$. The barrel part has an inner radius of 91 cm and an outer radius of 136 cm, containing 48 rings of 120 identical crystals. In the endcap, 820 crystals are divided into eight polar angle rows with a segmentation in ϕ varying between 80 and 120 crystals, as shown in Fig. 3.18. To account for the

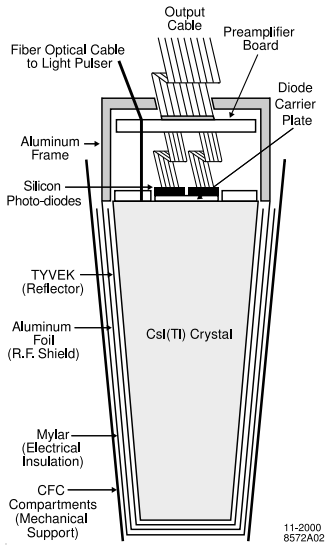

Figure 3.19: Schematic view of an EMC crystal assembly.

asymmetric beam energies, which lead to higher energies at smaller polar angles, the crystal length increases from 29.6 cm (15.1 X_0) in the backward direction to 32.4 cm (17.6 X_0) in the forward endcap. The crystals are almost square frusta[6] with a typical front face of 4.7×4.7 cm^2 and back face of 6.1×6.0 cm^2. A pair of silicon photodiodes is mounted at the rear face of each crystal to collect the scintillation light (see Fig. 3.19).

Since the energy deposited by a single particle is scattered over many crystals, a clustering algorithm is applied. The EMC is calibrated at low energies (~ 6 MeV) with a radioactive source and with Bhabha scattering events at higher energies, for which the dependence of energy on the polar angle is known. The overall energy resolution is shown in Fig. 3.20 and may be parametrized by

$$\frac{\sigma_E}{E} = \left(\frac{2.32 \pm 0.30}{\sqrt[4]{E(GeV)}} \oplus (1.85 \pm 0.12) \right) \% \tag{3.2}$$

where the sum is in quadrature. The first term, dominant at low energies, encompasses statistical fluctuations in scintillation photon yield and beam generated backgrounds, and the constant term is associated with light leakage and absorption in the material in front of or between the crystals. The angular resolution is determined from symmetric π^0 and η decays to be

$$\sigma_\theta = \sigma_\phi = \left(\frac{3.87 \pm 0.07}{\sqrt{E(GeV)}} \oplus (0.00 \pm 0.04) \right) mrad \tag{3.3}$$

which gives a resolution of about 12 mrad at low and 3 mrad at high photon energies, see Fig. 3.21. The overall calorimeter efficiency is about 96% for detecting photons with energy above 20 MeV.

The EMC serves also as the primary electron identification system. The two main methods to discriminate between electrons, muons, and hadrons rely on the ratio E/p of the shower energy deposited in the EMC to the track momentum (close to unity for

[6] A frustum is the portion of a solid - usually a cone or pyramid - which lies between two parallel planes cutting it.

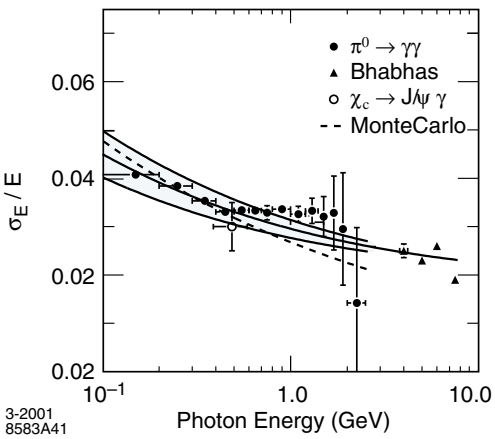

Figure 3.20: Energy resolution of the EMC measured for photons and electrons from various processes.

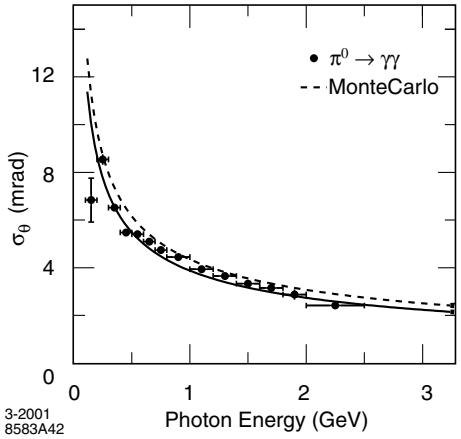

Figure 3.21: Angular resolution of the EMC for photons from π^0 decays.

electrons), and on the longitudinal and lateral distribution of the shower energy in the EMC. In addition, the $\mathrm{d}E/\mathrm{d}x$ energy loss in the DCH and the DIRC Čerenkov angle are required to be consistent with the electron hypothesis. Figure 3.25(a) shows the efficiency for electron identification and the pion misidentification probability.

3.3.5 IFR

Surrounding the EMC is a large iron yoke that serves as a flux return for the solenoid magnet. The flux return is instrumented to detect deeply penetrating particles such as muons and neutral hadrons (mostly K_L^0's and neutrons) that interact with the steel of the flux return. The IFR consists of a hexagonal barrel around the EMC and two two flat endcap doors, covering the polar angle region from 20° to 154° in the laboratory frame. Each section in the barrel (endcap) is composed of 19 (18) layers of detectors - resistive plate chambers (RPCs) that were later partially replaced by limited streamer tubes (LSTs) - sandwiched between layers of steel, as shown in Fig. 3.22. The steel plates increase in thickness from 2 cm in the inner nine plates to 10 cm for the outermost plates, motivated by the fact that thin absorber plates improve muon and K_L^0 detection only for the first absorption length, allowing thicker absorbers and less readout layers at larger distances. The total thickness of the steel plates amounts to 65 cm (60 cm) in the barrel (endcaps) at normal incidence. Two additional layers of cylindrical RPCs are located between the EMC and the magnet cryostat to detect particles exiting the EMC.

The planar[7] RPCs are constructed in modules of 320 cm × 130 cm and consist of two 2 mm bakelite sheets, coated with graphite on their external surfaces, and held 2 mm apart by spacers. The space between the sheets is filled with a mixture of 56.7% argon, 38.8% freon, and 4.5% isobutane. The graphite surfaces are held at a potential difference of $\sim$ 8 kV and protected by an insulating mylar film, as shown in Fig. 3.23.

[7] cylindrical RPCs feature a different layout, but operate similarly.

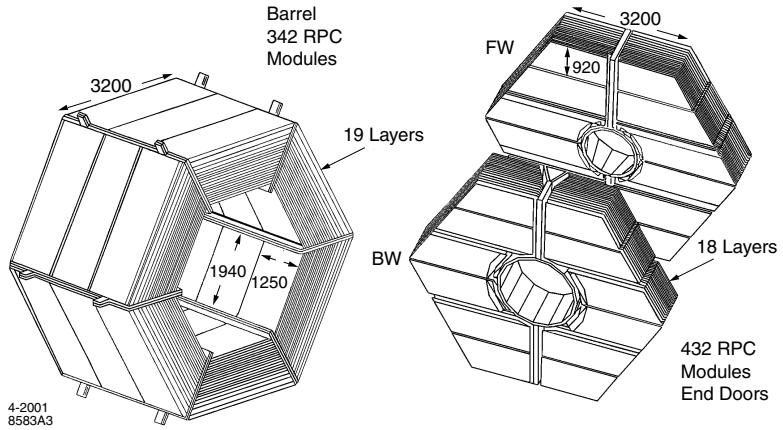

Figure 3.22: The IFR barrel and forward (FW) and backward (BW) endcaps.

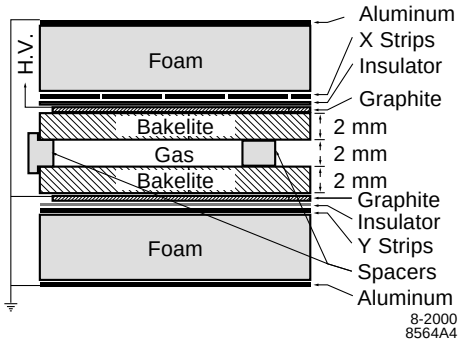

Figure 3.23: Cross section of a planar RPC with the schematics of the HV connections.

Ionizing high-energy particles traversing the gas volume create a discharge between these two surfaces, which is picked up by capacitive aluminum strips running parallel and perpendicular to the beam, providing both ϕ and z coordinates of the location of the discharge.

Linseed oil was used to coat the inner bakelite surfaces, and degradation of this and the graphite surfaces contributed to efficiency losses as the experiment progressed. Therefore, LSTs were installed to replace all RPCs in the barrel. Two sextants were replaced in the summer of 2004, and the remaining four sextants in the summer of 2006, during major downtimes. The 19 layers of RPCs were replaced by twelve layers of LSTs and six layers of additional brass absorbers.[8] The brass absorbers were installed in every second layer starting with the fifth to increase the total absorption length (and compensate for the loss of absorption in the outermost steel layer).

An LST consists of seven (eight) cells with a cross-section of 15×17 mm^2, arranged side-by-side in a PVC housing to form 3.5 m long and 13.5 (15.4) cm wide individual modules (see Fig. 3.24). Each cell has a 100 μm gold-plated beryllium copper wire running down its center, and is filled 3.5% argon, 8% isobutane, and 88.5% carbon dioxide. The wires are held at high voltage of $\sim$ 5.5 kV. The operational principle is

[8] the outermost layer of RPCs was physically inaccessible.

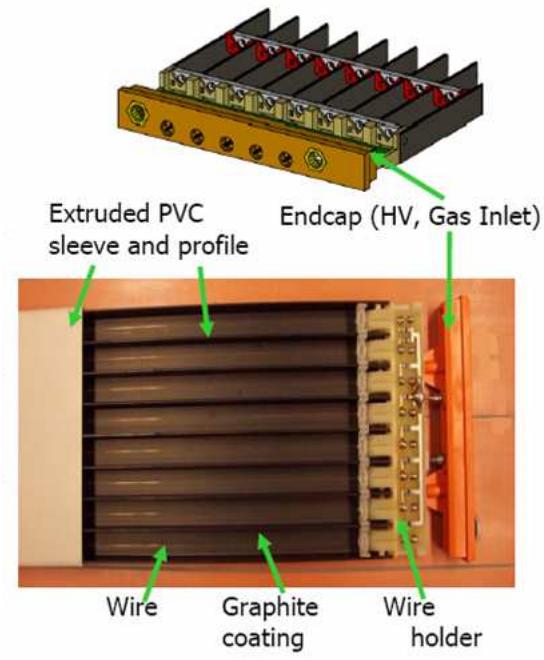

Figure 3.24: Picture and schematic drawing of a LST module.

analogous to that of the RPCs: streamers produced by ionizing high-energy particles passing through the gas volume are detected and read-out by the wire, providing the ϕ-coordinate. The streamer also induces a pulse on a series of conducting strips running perpendicular to the wires (z-planes), placed below the LST modules, providing the z-coordinate.

While muon identification relies almost entirely on the IFR, other detector systems provide additional information. Information from the IFR is combined with tracks identified by the SVT and DCH that meet the criteria for minimum ionizing particles in the EMC. Muon efficiencies close to 90% can be achieved for tracks with momentum between 1.5 and 3 GeV, see Fig. 3.25(b). IFR clusters not associated with charged tracks can be identified as K_L^0 mesons with an angular resolution of roughly 60 mrad, but no energy information. If the K_L^0 also interacts in the EMC, this resolution is improved by a factor of two.

3.3.6 Trigger

The task of data acquisition presents a challenge in high luminosity experiments: at the design luminosity of PEP-II, background rates[9] are typically around 20 kHz, compared to the (design) $b\overline{b}$ production rate of 3.2 Hz. The *BABAR* trigger system was developed to reject background events with sufficient efficiency that the remaining events can be written to disk at a managable rate of 120 Hz. The total trigger efficiency is required to exceed 99% for $B\overline{B}$ events and 95% for continuum events. The trigger is implemented as a two-tiered system: the hardware-based Level 1 (L1) trigger reduces beam-induced background rates to less than 2 kHz, followed by the software-based Level 3 (L3) trigger, which runs together with the acquisition software and has an output rate limited to 120 Hz by the downstream storage and processing capability.

[9] background rates are defined via events with at least one track found in the DCH with $p_T > 120$ MeV/c/ or at least one cluster found in the EMC with $E > 100$ MeV.

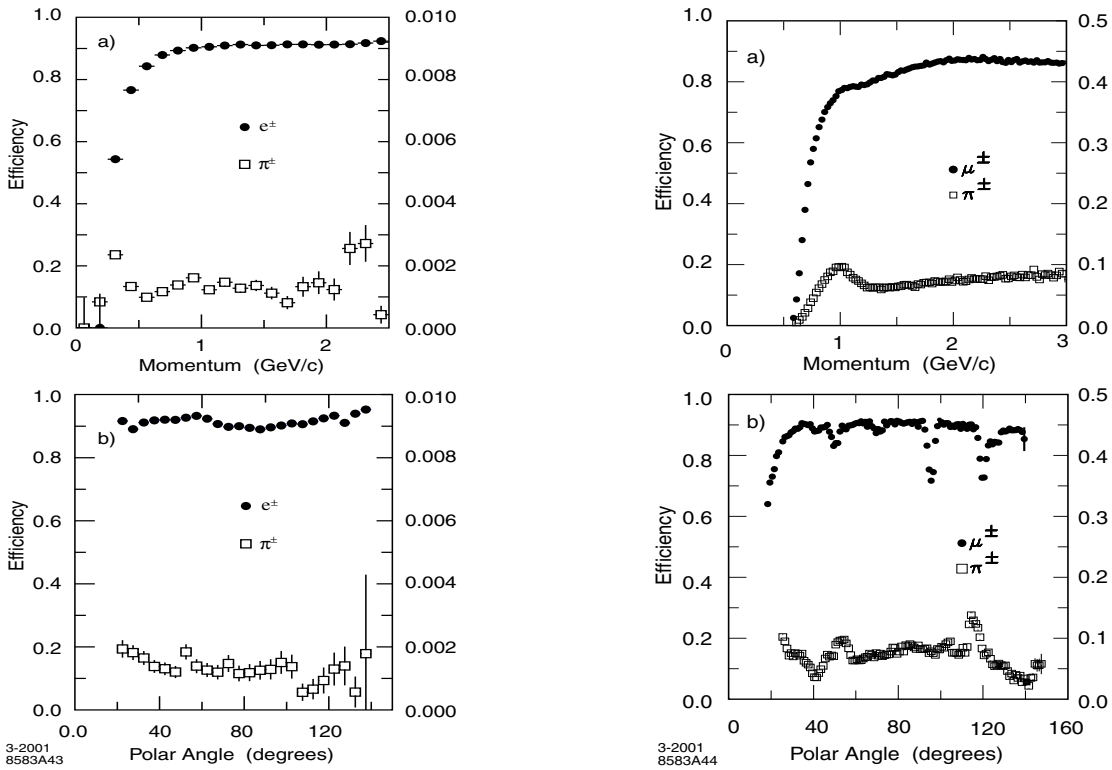

(a) Electrons (b) Muons

Figure 3.25: Lepton identification and pion misidentification probability as a function of momentum (top) and polar angle (bottom), as determined by the EMC for electrons (a), and by the IFR for muons (b). Note the different scales for identification and misidentification on the left and right ordinates.

The L1 trigger is implemented via hardware boards housed in several VME crates and consists of three subtriggers:

- The input data to the DCH trigger (DCT) consists of one bit for each of the 7104 DCH cells, updated every 269 ns. Track segments are formed from clusters of cell hits in each superlayer, and assembled into full tracks by the binary link tracker (BLT). The transverse momentum discriminator (PTD) then checks these tracks against some configurable p_T threshold values.
- The EMC trigger (EMT) divides the EMC into 280 towers, sums up the energies of all its crystals above a 20 MeV threshold every 269 ns, and forms clusters from various combinations of adjacent towers.
- The IFR trigger identifies $e^+e^- \rightarrow \mu^+\mu^-$ events and cosmic rays by checking for coincident hits in at least four IFR layers. This is used primarily for diagnostic purposes.

The DCT and EMT outputs are used to form L1 *primitives* which are sent to the Global Trigger (GLT) for time-alignment and some additional processing, e.g. matching BLT tracks with EMT clusters. The maximum L1 response latency for a given collision is 12 μs as determined by the FEE data buffer. The z_0 distribution of all accepted L1 tracks as reconstructed by L3 is shown in Fig. 3.26 and illustrates how a large fraction of the L1 tracks originate from backgrounds.

The software-based L3 trigger is an online application that acts primarily as an event filter and is responsible for making a logging decision based on the output of the L1 trigger. It involves a basic reconstruction of the event through a track finding algorithm for the DCH and a clustering algorithm for the EMC. The kinematics and topology of the reconstructed event allow the event to be categorized for acceptance or rejection, or any other special category needed for luminosity determination, diagnostics, or calibration.

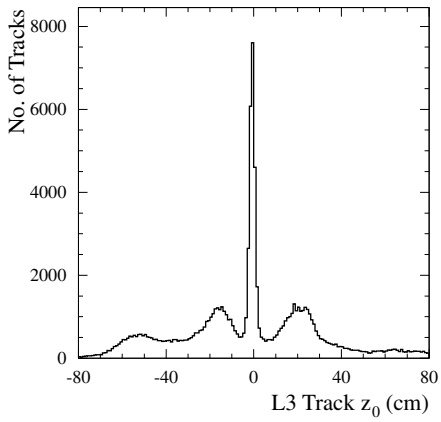

Figure 3.26: Distribution of z_0 for L1 tracks, reconstructed by L3. Tracks produced near the IP ($z = 0$) correspond to physics events, whereas the peaks around $z = \pm 20$ cm correspond to a flange joint in the beam pipe.

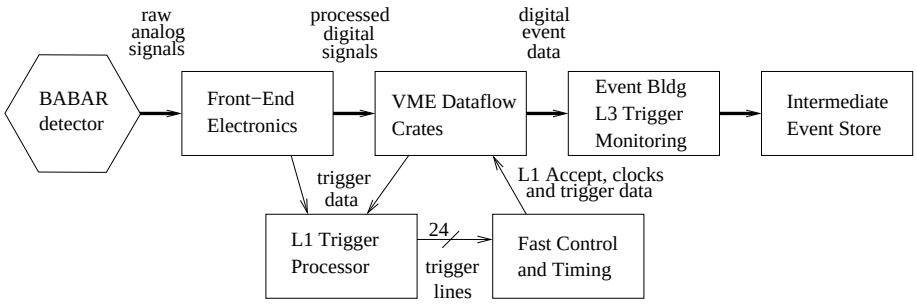

Figure 3.27: Schematic diagram of the data acquisition at *BABAR*.

3.3.7 Data acquisition

All subdetector systems share a common electronics architecture and utilize standard *BABAR* interfaces to the data acquisition electronics and software. The front-end electronics (FEE) for any detector component are mounted directly on the detector system. The FEE chain digitizes the detector signals, buffers the digitized output, and forwards that information to the trigger system. Once triggered, the output of an FEE is transferred to storage via read-out modules (ROMs), which connect to the FEE circuits via fiber optic cables and provide the standard interface between the detector-specific electronics of the FEEs and the fast-control and timing system (FCTS) as well as the event builder. Subsystem-specific feature extraction, in which the relevant features of the raw data are extracted, is also done in the ROMs.

The data acquisition and computing systems responsible for the transport of event data from the detector FEEs to mass storage with a minimum of dead-time are shown in Fig. 3.27. The decision to read out the front-end data from the detector subsystems is made by the FCTS based primarily on information from the L1 trigger. These systems also interface with the trigger to enable calibrations and testing. Other parts of the these systems provide for the control and monitoring of the detector and supporting facilities. Events that pass the L3 trigger are sent to the logging manager which writes the data to an extended tagged container (XTC) file. The XTC files are processed by online prompt reconstruction (OPR), and reconstructed events are written to *BABAR*'s Root-based event store (kanga).

Table 3.3: Overview of the coverage, segmentation, and performance of the *BABAR* detector systems. The notation (C), (F), and (B) refers to the central barrel, forward, and backward components of the system, respectively. The coverage in the laboratory frame is specified in terms of the polar angles θ_F (forward) and θ_B (backward). Performance numbers are quoted for 1 GeV/c particles, except where noted otherwise. The tracking performances for the SVT and DCH are quoted for a combined Kalman fit.

System	θ_F (θ_B)	No. Channels	No. Layers	Segmentation	Performance
SVT	20.1° (150.2°)	150K	5	50–100 μm $r-\phi$ 100–200 μm z	$\sigma_{d_0} = 55$ μm $\sigma_{z_0} = 65$ μm
DCH	17.2° (52.6°)	7,104	40	6–8 mm drift distance	$\sigma_\phi = 1$ mrad $\sigma_{\tan\lambda} = 0.001$ $\sigma_{p_T}/p_T = 0.47\%$ $\sigma(\mathrm{d}E/\mathrm{d}x) = 7.5\%$
DIRC	25.5° (141.4°)	10,752	1	35 × 17 mm^2 ($r\Delta\phi \times \Delta r$) 144 bars	$\sigma_{\theta_C} = 2.5$ mrad per track
EMC(C)	27.1° (140.8°)	2 × 5,760	1	47 × 47 mm^2 5,760 crystals	$\sigma_E/E = 3.0\%$ $\sigma_\phi = 3.9$ mrad
EMC (F)	15.8° (27.1°)	2 × 820	1	820 crystals	$\sigma_\theta = 3.9$ mrad
IFR(C)	47° (123°)	22K+2K[b] 9,726[c]	19+2[b] 12[c]	20–38 mm	90% $\mu^\pm$ eff. 6–8% $\pi^\pm$ mis-id.
IFR(F)	20° (47°)	14.5K	18	28–38 mm	(loose selection, 1.5–3.0 GeV/c)
IFR(B)	123° (154°)	14.5K	18	28–38 mm	

[b] central barrel outfitted with RPCs
[c] central barrel outfitted with LSTs

Chapter 4

Dataset

4.1 On-peak and off-peak data

The analysis presented in this dissertation is based on the full *BABAR* dataset collected from 1999-2008 at the PEP-II asymmetric-energy collider of the SLAC National Accelerator Laboratory. *On-peak* data refers to data collected at a CM energy of 10.58 GeV, the mass of the $\Upsilon(4S)$ resonance. The Υ system is the system of bottomonium states with $J^{PC} = 1^{--}$, bound states of a b and a $\bar{b}$ quark, which exhibit a spectrum of various excitation levels. As shown in Fig. 4.1, the $\Upsilon(4S)$ resonance is the first state above the $B\overline{B}$ production threshold, and thus can decay into pairs of B mesons via the strong interaction. The following physics processes contribute to the *BABAR* data:

- $e^+e^- \to \Upsilon(4S) \to B\overline{B}$
- $e^+e^- \to q\overline{q}\ (\gamma)$ where $q = u, d, s, c$ (continuum)
- $e^+e^- \to e^+e^-\ (\gamma)$ (QED continuum). The cross section for Bhabha scattering is approximately a factor of 40 larger than that for $B\overline{B}$ production; these events are used for detector calibration, but not included in the main dataset for analyses.
- $e^+e^- \to \mu^+\mu^-$, $\tau^+\tau^-$ (QED contunuum). Lepton pair production.
- Other pure QED processes such as $e^+e^- \to 2\gamma$.

On-peak data includes events of all the types mentioned above, with their relative frequencies given by the corresponding cross sections described in Table 3.2. The integrated luminosity[1] of the on-resonance data is 426 fb^{-1}, corresponding to 467.8 million $B\overline{B}$ pairs [44]. An additional integrated luminosity of 44.5 fb^{-1} was recorded 40 MeV below the $\Upsilon(4S)$ resonance. This *off-peak* data is below the $B\overline{B}$ production threshold (see Fig. 4.1), and therefore makes a good sample for studying *continuum* background events $e^+e^- \to f\bar{f}$ and their contributions to the on-peak data, where f may be any of the charged leptons or lighter quarks u, d, s, or c. The breakdown of the luminosity for each *Run*[2] is listed in Table 4.1.

4.2 Monte Carlo simulations

In order to understand the performance of the detector, study the signature of the desired signal mode, and evaluate backgrounds, the *BABAR* collaboration simulates the above mentioned physics processes and the response of the detector with Monte Carlo (MC) techniques. The production of Monte Carlo simulated data is performed in three stages. First, physical processes are simulated by an event generator (most importantly EvtGen for B physics and Jetset for continuum) and all particles and their four-momenta are recorded [49]. The particles are then propagated through a model of the *BABAR* detector. Interactions between these particles and the material of the detector are simulated using the GEANT4 simulation toolkit [50]. Finally, the detector response is simulated and digitized, yielding signals which mimic those collected from the detector electronics. Real background events are mixed with simulated events to more closely reproduce the data. The usual trigger and reconstruction algorithms are then applied to the event.

MC data sets are designed to reproduce the data as closely as possible, including

[1] This integrated luminosity is computed offline with the bookkeeping tool `BbkLumi` and gives a more accurate result than the online estimate quoted in Section 3.3.

[2] A Run is a period of continuous data taking between major detector downtimes.

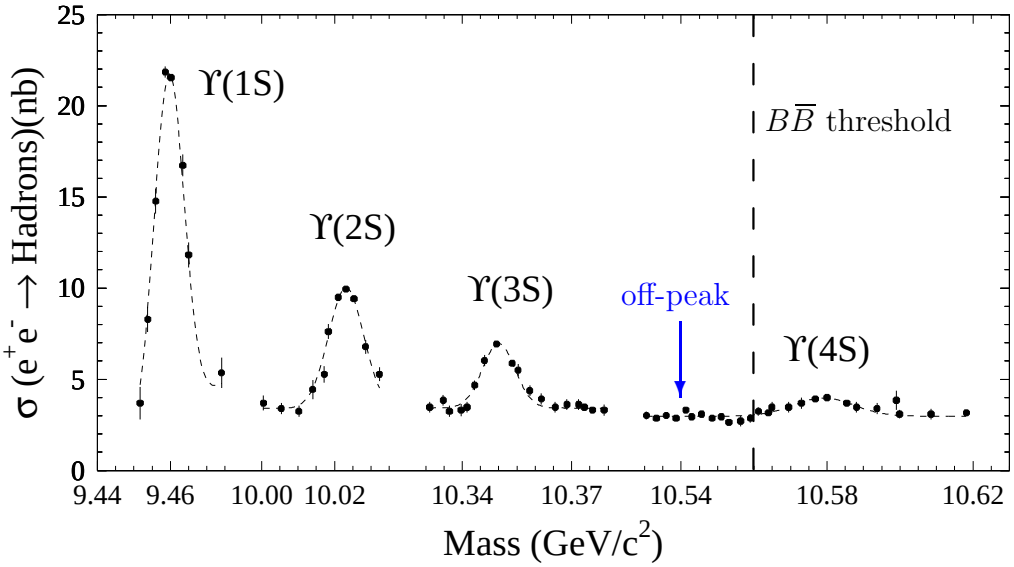

Figure 4.1: Total e^+e^- annihilation cross section into hadrons at the first four S-wave Υ resonances as a function of CM energy, as measured at CESR [47, 48]. The $\Upsilon(4S)$ is the third radial excitation of the spin $S = 1$ ground state. Its larger width is evidence that it is just above the threshold for strong decays into $B\overline{B}$ pairs, as indicated by the dashed line. The CM energy for *off-peak* data taking is also indicated in blue. Note that the abscissa is broken up into segments.

Table 4.1: Data samples used in the analysis (based on release 22d).

Dataset	Luminosity (fb^{-1})	$N_{B\bar{B}}$ (10^6)	Number of events recorded (10^6)	Number of events skimmed (10^6)
Run 1 on-peak	20.40	22.39	280.3	9.54
Run 2 on-peak	61.08	67.39	917.8	29.7
Run 3 on-peak	32.28	35.57	485.1	16.3
Run 4 on-peak	100.3	110.5	1483	50.6
Run 5 on-peak	133.3	147.2	1970	65.3
Run 6 on-peak	78.75	84.77	1233	35.4
total on-peak	426.1	467.8	6369	206.8
Run 1 off-peak	2.62	-	32.56	0.52
Run 2 off-peak	6.92	-	96.76	1.48
Run 3 off-peak	2.47	-	34.19	0.56
Run 4 off-peak	10.12	-	137.2	2.29
Run 5 off-peak	14.49	-	195.1	3.16
Run 6 off-peak	7.88	-	111.9	1.55
total off-peak	44.5	-	607.8	9.56

the detector and other conditions at the time. Thus they are broken into Run cycles similar to the data sets that indicate which data sets they are intended to model.

MC simulation production is performed as a combination of all possible decays of a given particle, with relative frequencies according to their respective branching fractions (*generic* modes), or as a *signal* mode, where the particle is constrained to decay in the specific decay mode of interest, to allow studying the expected signature of that particular decay. The size of the MC samples typically exceeds the $B\overline{B}$ data sample by at least an order of magnitude for signal modes, and about a factor of three for generic $B\overline{B}$ events. For this analysis, the signal mode $B^{\pm} \to \omega l^{\pm}\nu$ (`SP-4761`) is generated with a flat q^2 distribution. Although a flat q^2 distribution is not very physical,[3] the exact (or even approximate) shape of the distribution for the signal decay is not well known, and varies depending on the specific theoretical model used to calculate the form factors. It was thus chosen to use a flat q^2 distribution to avoid introducing a bias in favor of any particular theoretical model. The other B meson decays generically. The various MC samples used in this study are outlined in Table 4.2 for generic MC samples and in Table 4.3 for the MC signal mode.

4.3 Skim

Both data and Monte Carlo simulation samples are reduced in size by the `BToDlnu` skim [51] before analysis. Skimming refers to the process of filtering events for a subset that satisfies certain selection criteria. This skim applies some loose cuts to filter events for inclusive $B \to Dl\nu(X)$ semi-leptonic decays, where the X is either nothing or a soft pion or photon. Both charged and neutral B decays, and thus both neutral and charged D modes, are considered.

Events are initially chosen via a set of filters and preselectors and suitable compos-

[3] see e.g. Fig. B.1 for the q^2 spectrum of the form factors in the framework of the LCSR model described in Section 2.3.2.

Table 4.2: MC samples used in this analysis (release 22d).

MC sample	Number of events generated (10^6)	Number of events skimmed (10^6)	Cross-section (nb)	Equivalent luminosity (fb^{-1})
generic B^+B^-				
Run 1	36.97	9.87	0.55	67.2
Run 2	103.1	28.1		187.5
Run 3	49.77	13.5		90.5
Run 4	168.0	45.5		305.4
Run 5	244.2	65.8		444.0
Run 6	68.02	17.2		123.7
total B^+B^-	670.1	180.0		1218.3
generic $B^0\overline{B}^0$				
Run 1	37.20	9.65	0.55	67.6
Run 2	103.4	27.4		187.9
Run 3	50.56	13.4		91.9
Run 4	167.3	44.1		304.2
Run 5	244.8	64.1		445.1
Run 6	68.15	16.7		123.9
total $B^0\overline{B}^0$	671.4	175.4		1220.6
continuum background $c\bar{c}$				
Run 1	58.9	5.61	1.30	45.3
Run 2	168.8	17.2		129.8
Run 3	84.0	8.68		64.6
Run 4	252.8	25.9		194.5
Run 5	366.8	37.3		282.2
Run 6	104.8	9.26		80.6
total $c\bar{c}$	1036	104.0		707.0
continuum background $u\bar{u}$, $d\bar{d}$, $s\bar{s}$				
Run 1	47.2	1.54	2.09	22.6
Run 2	130.9	5.15		62.2
Run 3	66.9	2.84		32.0
Run 4	213.4	8.73		102.1
Run 5	317.8	12.8		152.1
Run 6	84.4	2.40		40.4
total uds	859.7	33.46		411.4
continuum background $\tau^+\tau^-$				
Run 1	20.4	0.101	0.94	21.7
Run 2	55.6	0.310		59.1
Run 3	28.0	0.166		29.8
Run 4	90.0	0.549		95.7
Run 5	132.2	0.809		140.6
Run 6	68.1	0.400		72.4
total $\tau^+\tau^-$	394.3	2.335		419.3

Table 4.3: MC signal sample used in this analysis (release 22d).

MC signal mode $B \to \omega\ell\nu$	Number of events generated (10^3)	Number of events skimmed (10^3)	Equivalent luminosity[b] (fb^{-1})
Run 1	105	59.6	329
Run 2	314	180	984
Run 3	165	93.8	517
Run 4	506	286	1586
Run 5	664	373	2082
Run 6	208	114	652
total $B \to \omega\ell\nu$	1962	1106	6150

[b] The cross-section is $2 \times 2 \times 1.45 \cdot 10^{-4} \times 0.55\, nb$ [14]: the first factor of 2 takes into account that, in quoted branching fractions, ℓ refers to an electron *or* a muon, not the sum of both; the second factor of 2 arises since either B meson can decay in the signal mode; $1.45 \cdot 10^{-4}$ is the $B \to \omega\ell\nu$ branching fraction used in the event generator; $0.55\, nb$ is the B^+B^- cross-section.

ite candidates are taken from relevant lists in the event. Suitable D^0 and D^+ candidates are reconstructed in certain modes, and combined with soft pions to form D^{*0} and D^{*+} candidates. Additionally, a suitable lepton matching the flavor of the $D^{(*)}$ candidate and having a minimum CM momentum of 800 MeV/c is required. Events with no viable $D^{(*)}\ell$ candidates are rejected. The skim reduces the sample size to about 25% for generic $B\overline{B}$ Monte Carlo or less for other modes.

4.4 Data structure

The raw data collected by the *BABAR* detector is just a collection of digitized detector hits from each subdetector, which are used to reconstruct pattern-recognition objects, such as SVT and DCH tracks, and EMC and IFR clusters. These pattern-recognition objects are then used to reconstruct charged and neutral particle candidates by *online prompt reconstruction* (OPR). The output of OPR is stored in *BABAR*'s main database, the *Event Store*. Most of the event information is stored either as lists of particle candidates, or as tag variables that describe the overall event. The particle candidate lists produced by OPR, most notably `ChargedTracks` and `CalorNeutral`, serve as buidling blocks for more specialized lists produced at run-time, which can be lists of composite particles or more refined lists, such as those passing a given particle identification (PID) selector. The candidate lists used in this analysis will be discussed in Section 6.1.

Chapter 5

Event Selection

Due to the sheer volume of data collected at *BABAR* (Table 4.1), it is impractical to process the full data set at once. By selecting events that are likely to contain the physical process under investigation over several successive stages with increasingly tighter requirements, demands on CPU time and disk space can be reduced significantly. Applying the `BToDlnu` skim as described in the previous section is the first stage, and the event selection described in this section is the second stage in this process (to be followed by the explicit reconstruction of all final state candidates in Section 6). The goal of the event selection is to remove as many background events as possible, while keeping most of the signal events, just by examining event variables, i.e. variables that describe the event as a whole.

An example of a typical reconstructed signal event is shown in Fig. 5.1. In this case, a negative B meson decays into a negative muon, a neutral ω (which itself decays further into one neutral and two charged pions), and an unobserved neutrino. The trajectories of the three charged final state particles are reconstructed by linking SVT and DCH hits (and, to a lesser extent, EMC clusters), whereas the presence of a neutral π^0 is inferred from the energy deposited in the EMC by its two γ daughters.

Most of the event information, as stored in the *Event Store*, is categorized in one of two formats: lists of particle candidates containing information about specific objects that are associated with a potential particle, and tag variables that describe the overall

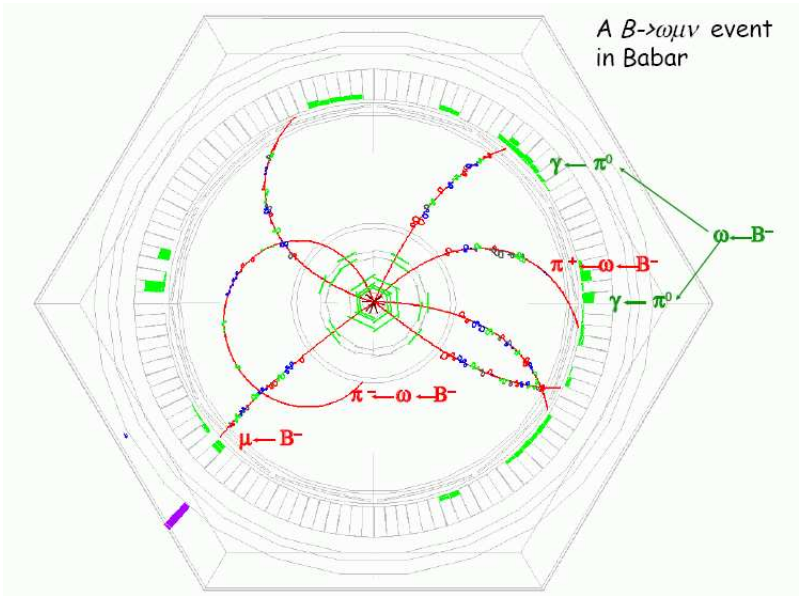

Figure 5.1: Display of a $B \to \omega\mu\bar{\nu}$ event in the *BABAR* detector, produced with the HEP Event Display application HepRApp using MC simulation of a signal decay. The tag B decay is not specified. The view is along the z-axis of the detector. SVT hits and EMC clusters are depicted green, and tracks inferred from DCH hits are shown in red.

event. These tag variables, and basic properties of some particle candidates are used in the event selection. The criteria used for this event selection can be categorized in the following three groups:

- Event topology: B mesons from a $\Upsilon(4S)$ decay are produced nearly at rest so that their decay products are distributed rather uniformly, whereas $q\overline{q}$ events have a more jet-like structure, with the angular distributions of the jets peaked along the beam axis. A suitable variable to distinguish between these different event shapes is the second normalized Fox-Wolfram moment $R2$, which vanishes for isotropic events and is equal to unity for completely collimated events [52]. The distribution of $R2$ for various event types with 100,000 events each is shown in Fig. 5.2. We impose the loose requirement that $R2$ be no greater than 0.7.

- Candidate multiplicity: These cuts are driven mostly by the need to be able to reconstruct the full set of final state candidates, but also provide some significant background suppression. On both the tag and the signal side, at least three charged tracks are required. More specifically, at least three pions and one kaon from their respective lists are needed to reconstruct the hadrons on the tag and signal side, which then need to be combined with one charged lepton on each side for the full final state reconstruction. Lepton pair events in particular have a much lower multiplicity of charged tracks than $B\overline{B}$ events, as shown in Fig. 5.3. We also need at least one π^0 for the ω, which implies the presence of at least two photons in the event. We require the momenta of the π^0's daughter photons to be greater than 50 MeV/c. For a complete list of the candidate multiplicity cuts see the bottom part of Table 5.1.

- Presence of two high-momentum leptons: At least one lepton is needed to successfully reconstruct a semileptonic B decay. Since this analysis uses another semileptonic decay to tag the flavor of the other B meson, the event must con-

Table 5.1: Summary of event selection cuts. The shaded areas refer to cuts on individual candidates before cuts on the corresponding list are applied. For descriptions of the particle lists see Section 6.1.

Cut variable	Cut value
R2	≤ 0.7
Laboratory photon momentum p_γ	≥ 50 MeV/c
CM lepton momentum p^*_ℓ	≥ 0.8 GeV/c
Particle list	**Min. number of candidates**
`GoodTracksVeryLoose`	6
`GammaForPi0`	2
`pi0AllDefault`	1
`piLHLoose`	3
`KNNLoose`	1
(`eBremReco + nuNNLoose`)	2[a]

[a] of opposite charge

tain two leptons. Additionally, since the parent B mesons have opposite charges, so must their daughter leptons. Figure 5.4 shows the momentum distribution in the CM frame for various types of leptons. Since both tag and signal leptons are primary B daughters, they typically carry a higher momentum than leptons originating lower in the decay chain. We require that both leptons have a momentum of $p^*_\ell \geq 0.8\,\mathrm{GeV}/c$, as measured in the $\Upsilon(4S)$ rest frame, to suppress background mostly from secondary leptons and misidentified charged hadrons. Secondary leptons are leptons originating from the decay of a particle other than a B meson, for instance charm mesons, τ leptons, J/ψ, or from photon conversions.

The cuts applied for the event selection are summarized in Table 5.1. The efficiencies of these cuts for various data samples are listed in Table 5.2.

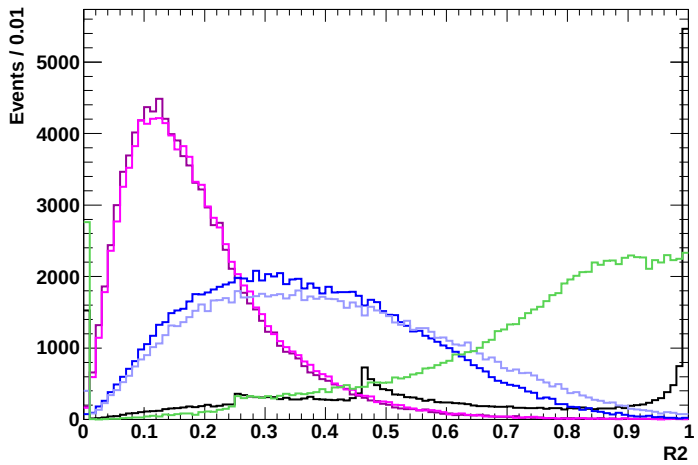

Figure 5.2: Distribution of the second normalized Fox-Wolfram moment, $R2$, for various MC and data event types, as indicated by the legend below, for 100,000 events each. Off-peak data has been scaled by a factor 1/3 because of its strong peak at $R2 = 1$ due to Bhabha scattering.

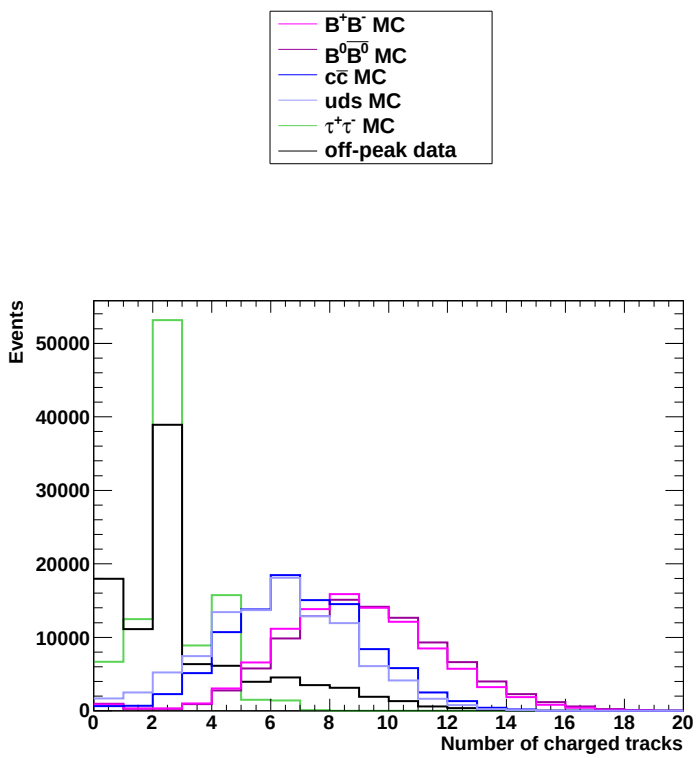

Figure 5.3: Number of charged tracks per event for various MC and data event types, as indicated by the legend above, for 100,000 events each.

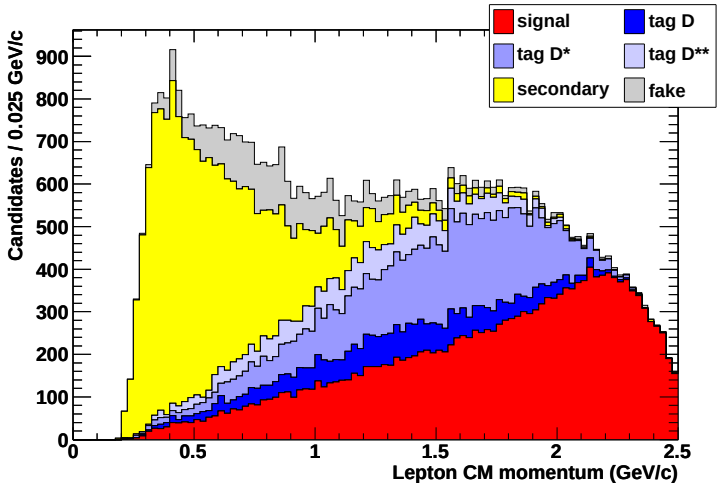

Figure 5.4: CM momentum distribution for various lepton types, as indicated by the legend.

Table 5.2: Efficiency of event selection cuts for various data samples.

Dataset	Number of events (10^6)			Efficiency
	recorded/generated	skimmed	passing event selection	(%)
on-peak data	6369	206.8	8.754	0.137
off-peak data	607.8	9.56	0.238	0.039
MC signal	1.962	1.106	0.056	2.88
B^+B^-	670.1	180.0	11.12	1.66
$B^0\overline{B}^0$	671.4	175.4	9.340	1.39
$c\bar{c}$	1036	104.0	3.264	0.315
uds	859.7	33.46	0.655	0.076
$\tau^+\tau^-$	394.3	2.335	0.002	$5.4 \cdot 10^{-4}$

Chapter 6

Candidate Selection

In this chapter we outline the details of the candidate selection process, starting with a description of the relevant candidate lists and of the criteria by which we classify the various signal and background contributions. To reconstruct and select the full set of final state candidates, we proceed in the following way: after the loose reconstruction of the tag (Section 6.3) and an independent and similarly loose reconstruction of the signal (Section 6.4), we combine both B decay hypotheses for a characterization of the full event (Section 6.5), and then select the "best" combination of final state candidates according to the criteria outlined in Section 6.6.

6.1 PID and composite lists

The primary list of charged tracks used in this analysis is the `GoodTracksVeryLoose`, which consists of the subset of tracks from the OPR list `ChargedTracks` with momentum less than 10 GeV/c (in the laboratory frame) and some additional constraints on the distance of closest approach (DOCA) of the track to the interaction point (IP). The primary electron list used is `PidLHElectrons` which employs a likelihood-based selector on tracks taken from `ChargedTracks`. The primary muon list is `muNNLoose` based on a neural network selector trained for muon-pion discrimination. For electrons, the emission of bremsstrahlung photons can have a significant effect on the measurement of its momentum by the tracking system. The standard *BABAR* bremsstrahlung recovery

algorithm [53] is used to identify those $e^{\pm} \to e^{\pm}\ \gamma$ electrons and compensate for the missing momentum carried away by the photons; the relevant list is called `eBremReco`.

Charged pions are taken from the likelihood-selector based `piLHLoose` list, and charged kaons are taken from the `KNNLoose` list, which uses a neural network selector. In both cases, $\mathrm{d}E/\mathrm{d}x$ information from the SVT and the DCH is combined with DIRC parameters like the Čerenkov angle and the number of detected photons to decide whether a given track object passes the specific selector.

All single-bump neutral clusters found in the EMC that are not matched with any track are contained in the `CalorNeutral` list. Based on this list, the `GammaForPi0` list is optimized for use in reconstructing $\pi^0 \to \gamma\gamma$ decays and requires at least 30 MeV of raw energy in the cluster and a lateral moment[1] of less than 0.8. The primary list used for reconstructing π^0 candidates is `pi0AllDefault`, which contains pairs of photons taken from `GammaForPi0` with invariant mass between 115 and 150 MeV/c^2 and (laboratory frame) energy greater than 200 MeV; it also contains merged π^0 candidates[2] with a merged π^0 consistency (derived from the cluster shape) greater than 1%.

π^0 candidates originating from a $D^{*0} \to D^0\ \pi^0$ decay have a very well defined momentum of 42.5 MeV/c in the D^{*0} rest frame, which translates into a *soft* (low momentum) π^0 in the laboratory frame. Thus, for D^{*0} reconstruction, we use the `pi0SoftDefaultMass` list, which is essentially the same as the `pi0AllDefault` list (without the merged π^0 candidates), but with a 450 MeV/c upper limit on the CM momentum of the π^0 candidates.

[1] a measure of the lateral spread of the shower.

[2] When the opening angle between the two photons is too small, the photon clusters are merged into one cluster, and their kinematic parameters cannot be extracted separately. In this case, the invariant mass of the π^0 system is estimated from the shape of the merged cluster; these candidates are referred to as merged π^0 candidates [54].

6.2 Signal and background classification

When reconstructing candidates for the charmless semileptonic decay $B \to \omega \ell \nu$, a variety of other physics processes mimic a signal decay and end up in the sample of selected candidates. We divide the signal and background candidates into a set of sources based on the origin of the charged lepton candidate.

- Signal/tag: We differentiate three classes of signal and tag candidates; for all of them the lepton originates from the correct decay. Events with wrongly assigned leptons are rare and typically don't survive the final candidate selection (see Section 6.6); thus they are not afforded a separate class.
  - True signal/tag: the hadron originates from the correct signal or tag decay.
  - Combinatorial signal/tag: the hadron has been incorrectly selected, in many cases from the decay products of the other B meson in the event.
  - Cross-feed tag: the tag hadron has been reconstructed in a certain tag decay mode, but belongs to one of the other reconstructed tag decay modes.
- $B \to X_u \ell \nu$ background: We differentiate two different sources of this background:
  - Exclusive $B \to X_u \ell \nu$ decays other than the signal decay.
  - Inclusive $B \to X_u \ell \nu$ decays involving more than one hadron.
- $B\overline{B}$ background: We differentiate three classes of $B\overline{B}$ background:
  - Primary leptons: the lepton originates from a leptonic or semileptonic B decay; for the tag reconstruction, signal decays are considered background, and vice versa.
  - Secondary leptons: the leptons originates from the decay of a particle other than a B meson, for instance a charm meson, τ lepton, J/ψ, or from photon

conversions.

  * Fake leptons: the lepton candidate is a misidentified charged hadron; this background is dominated by fake muons.

- Continuum background: We differentiate two different sources of continuum background:

  * True leptons: the lepton originates from a leptonic or semileptonic decay of a hadron produced in $e^+e^- \to q\overline{q}$ or $e^+e^- \to \ell^+\ell^-$ processes.

  * Fake leptons: the lepton candidate is a misidentified charged hadron.

The most dominant background comes from $B \to X_c\ell\nu$ decays, for which the inclusive branching fraction is roughly a factor of 50 larger; another significant contribution comes from continuum background events. The $B \to X_u\ell\nu$ decays have much smaller branching fractions, but their properties are very similar to the signal decay and are therefore difficult to discriminate against.

6.3 Tag reconstruction

By reconstructing the B meson recoiling against the signal B, its flavor, and thus the flavor of the signal B, is determined. This technique is called *flavor tagging*, and the recoiling B meson is referred to as the *tag* B. We reconstruct the tag B in the semileptonic charm decay $B \to D^{(*)}\ell\nu$, where $D^{(*)}$ can be a D, D^*, or D^{**} meson. By D^{**} we indicate orbitally excited D mesons with angular momentum $L = 1$ that decay mainly to $D^{(*)}\pi$ final states; this includes resonant and non-resonant $D^{(*)}\pi\ell\nu$ decays. The four known D^{**} states are $D_1(2420)$, $D_2^*(2460)$, $D_0^*(2400)$, and $D_1'(2430)$ [55]. The branching fractions for the semileptonic charm B decays relevant to this anlysis are listed in Table 6.1.

Since the tag B is charged, its charmed meson daughter must be neutral; we therefore only reconstruct neutral D or D^* mesons (in principle, neutral D^{**} mesons

Table 6.1: Branching fractions for charm semileptonic B decays relevant to this analysis. For D^{**}, branching fractions for specific subsequent D^{**} decays ($D^{**0} \to D^{(*)+}\pi^-$) are given in [9], which are combined with D^{**} branching fractions from [55] to give the overall $B \to D^{**}\ell\nu$ branching fractions quoted. The three contributions do not add up to the sum since not all D^{**} states are known.

Decay mode	$\mathcal{B}$ (%)	Ref.
$B^- \to D^0\ell^-\bar{\nu}_\ell$	2.24 ± 0.11	[9]
$B^- \to D^{*0}\ell^-\bar{\nu}_\ell$	5.68 ± 0.19	[9]
$B^- \to D^{**0}\ell^-\bar{\nu}_\ell$	1.43 ± 0.12	
$B^- \to D_1^0\ell^-\bar{\nu}_\ell$	0.44 ± 0.03	[9, 55]
$B^- \to D_2^{*0}\ell^-\bar{\nu}_\ell$	0.41 ± 0.05	[9, 55]
$B^- \to D_0^{*0}\ell^-\bar{\nu}_\ell$	0.38 ± 0.08	[9, 55]
$B^- \to D_1'\ell^-\bar{\nu}_\ell$	0.20 ± 0.06	[9, 55]
$B^- \to D\ell^-\bar{\nu}_\ell$ anything	9.8 ± 0.7	[14]

Table 6.2: Branching fractions for the hadronic D decay modes used in this analysis [14].

Decay mode	$\mathcal{B}$ (%)	Mass window (MeV/c^2)
$D^0 \to K^- \pi^+$	3.91 ± 0.05	± 20
$D^0 \to K^- \pi^+ \pi^0$	14.0 ± 0.5	± 30
$D^0 \to K^- \pi^+ \pi^+ \pi^-$	$8.14^{+0.20}_{-0.18}$	± 20

can also decay in charged modes $D^{(*)\pm}\pi^{\mp}$; however, due to their small contributions, these modes are not considered in this analysis). We reconstruct neutral D^0 candidates in the following three modes:

- $D^0 \to K^- \pi^+$
- $D^0 \to K^- \pi^+ \pi^0$, with $\pi^0 \to \gamma\gamma$
- $D^0 \to K^- \pi^+ \pi^+ \pi^-$

The branching fractions for these three modes are presented in Table 6.2. In reconstructing these D mesons, we initially apply a loose cut of $1.815 \leq m_D \leq 1.915\,\mathrm{GeV}/c^2$, which will later be tightened to the values listed in the same Table (see Section 6.5). Additionally, we require the vertex probability[3] of the D candidate to be at least 0.1%. The masses of the reconstructed D meson candidates are shown in Fig. 6.1 for the three different modes separately.

At this stage, all candidates in the wide D mass range from 1.815 to 1.915 GeV/c^2 are kept and combined into a single list. Members of this list are matched with a π^0 candidate from the `pi0SoftDefaultMass` list to form a D^* candidate. The sharp momentum peak of the π^0 daughter manifests itself in very well defined mass difference between a D^* and its D daughter, also shown in Fig. 6.1. If this mass difference deviates more than 5 MeV/c^2 from its nominal value of 142.1 MeV/c^2 [14], the D^* candidate is

[3] the probability that the candidate's daughters originated from a common vertex, based on a χ^2 test.

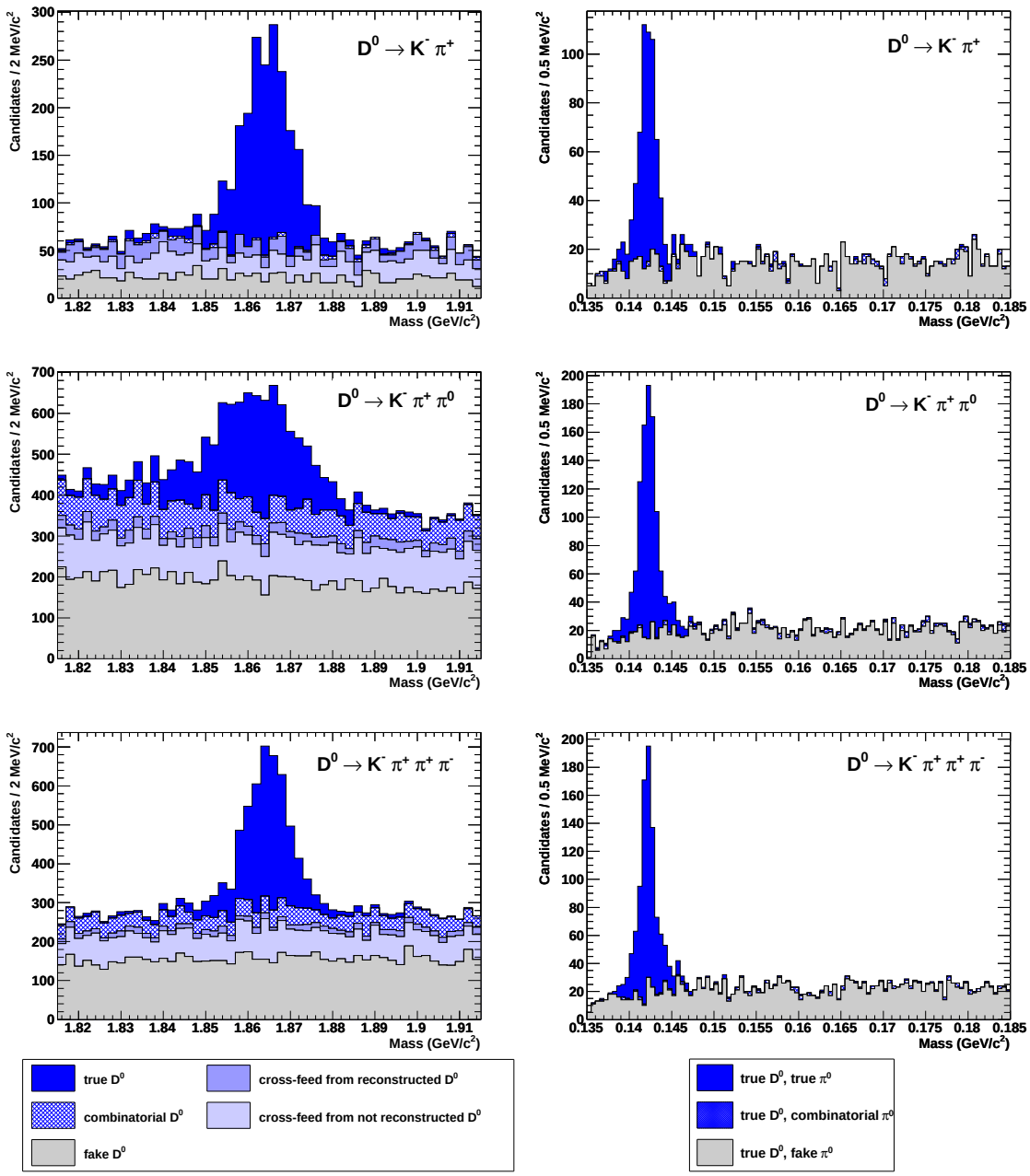

Figure 6.1: Mass of D candidates (left column) and mass difference between D^* candidates and their corresponding D daughters (right column) for $K^-\ \pi^+$ (top), $K^-\ \pi^+\ \pi^0$ (center), and $K^-\ \pi^+\ \pi^+\ \pi^-$ (bottom) modes, respectively. The various D candidates are described in the legends, where a distinction is made for cross-feed from the other two of the three reconstructed D decay modes, and cross-feed from all other D decay modes.

rejected.

Since the event contains at least one lepton of each charge, D or D^* candidates of both flavors can be combined with a lepton to form a $D^{(*)} - \ell$ candidate. This lepton must have the same charge as the K daughter of the D candidate. We refer to this $D^{(*)} - \ell$ combination as the $Y^{(*)}$ system, which represents the tag B minus the missing and not reconstructed neutrino.

Since the beam energy is known, we can determine θ_{BY}, the angle between the Y system and its parent B meson in a $B \to Y\nu$ decay, by the relation

$$\cos\theta_{BY} = \frac{2E_B^* E_Y^* - m_B^2 - m_Y^2}{2|\boldsymbol{p_B^*}||\boldsymbol{p_Y^*}|} \tag{6.1}$$

where E_B^*, m_B, and $|\boldsymbol{p_B^*}|$ (E_Y^*, m_Y, and $|\boldsymbol{p_Y^*}|$) are the energy, mass, and absolute momentum of the B meson (Y system) in the CM frame, respectively. In arriving at this relation, the massless neutrino hypothesis was assumed.[4] If the Y system is compatible with the $B \to Y\nu$ hypothesis, the angle θ_{BY} is a physical angle, and thus $|\cos\theta_{BY}| \leq 1$, up to detector resolution.

The distribution of this variable for various Y and Y^* combinations is shown in Fig. 6.2. True tag candidates are concentrated in the physical region, except for a tail of unphysical negative values of $\cos\theta_{BY}$, which is attributed to bremsstrahlung effects of the involved electrons. A loose cut of $|\cos\theta_{BY}| \leq 5$ is applied initially to avoid correlations with the quantity $\cos^2\Phi_B$ used to extract the signal yield.[5] A significant fraction of cross-feed from the Y^* mode into the Y mode and vice versa falls into the physical region of $\cos\theta_{BY^{(*)}}$, as can be seen in the top left and bottom right part of Fig. 6.2. The bottom right plot in particular provides the rationale to limit the final candidate selection to a Y^* candidate, provided one was found, as discussed in Section 6.6.

[4] See Appendix A.1.
[5] See Section 8.1.

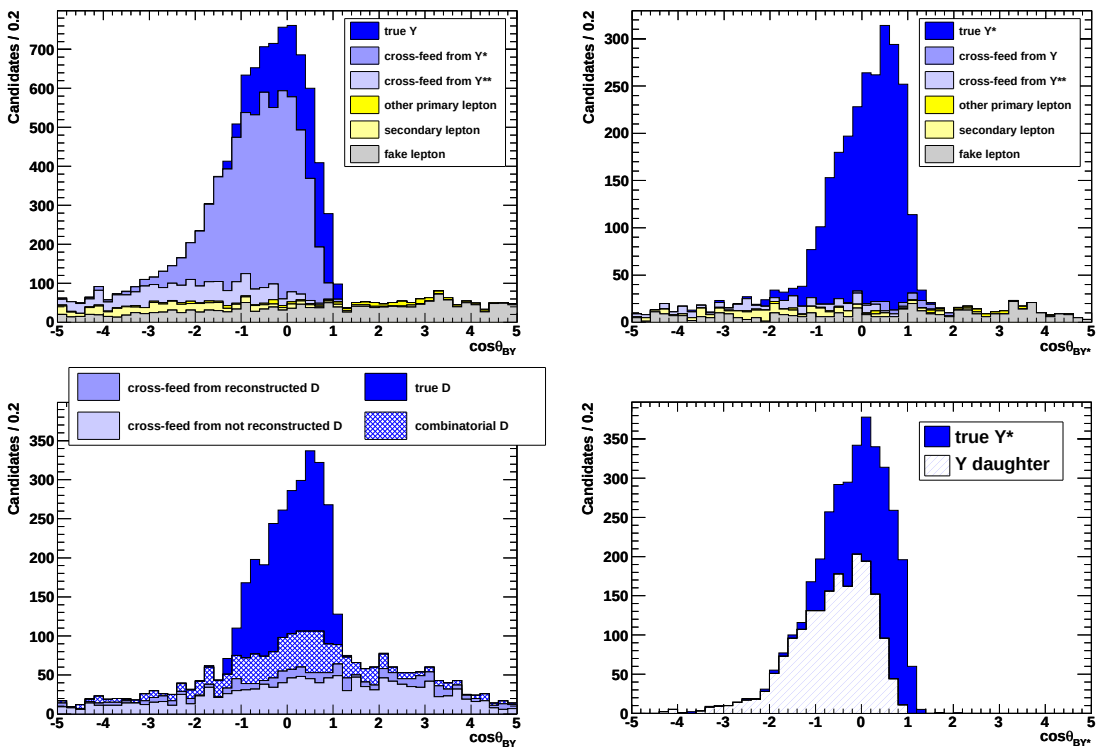

Figure 6.2: Cosine of the angle between the tag B and the Y (left column) or Y^* (right column) system. In the top row, leptons from various sources, as described in the legends, are combined with a true D (left) or D^* (right). In the bottom left, the effects of a mismatched D on a true tag lepton are shown. In the bottom right, a correctly reconstructed Y^* is compared to its corresponding Y system, to motivate the exclusion of those Y candidates from the final candidate selection, as described in Section 6.6.

6.4 Signal reconstruction

The signal side ω is reconstructed in the dominant $\omega \to \pi^+\pi^- \pi^0$ decay mode with a branching fraction of 89.2% [14]. At this point, we impose a very loose mass requirement of $0.5 < m_\omega < 1.1$ GeV/c^2 to allow for later background studies. The mass distribution of the ω candidates for signal and various background sources is shown in the left plot of Fig. 6.3. A peak at 550 MeV/c^2 from $B \to \eta\ell\nu$ decays is manifest in the $B \to X_u\ell\nu$ background, since η mesons have a sizeable branching fraction (28%) into the reconstructed signal mode $\pi^+\pi^- \pi^0$ [14].

Similar to the tag side, ω candidates can be combined with leptons to form an $\omega-\ell$ candidate, referred to as the X system, which represents the detected and reconstructed part of the signal B meson. The angle θ_{BX}, which is now the angle between the X system and its parent B meson, can be calculated in a similar fashion as was done for the tag side; its distribution is shown in the right-hand side of Fig. 6.3. The same loose cut of $|\cos\theta_{BX}| \leq 5$ is applied at this stage.

The relative momentum distribution of the hadron and the lepton is dictated by the kinematics of the particular decay channel. In general, however, the correlations between p^*_{had} and p^*_ℓ, in a given channel, are substantially different for properly reconstructed signal candidates than for combinatoric background candidates, particularly those where the lepton originated from either a $b \to c\ell\nu$ decay or a $q\overline{q}$ event. We exploit this difference to suppress background without significant signal losses. The relevant distributions for various signal and background sources are displayed in Fig. 6.4. In order to maintain a high selection efficiency, we require the condition

$$p^*_\omega + p^*_\ell \geq 2.5\,\mathrm{GeV}/c \tag{6.2}$$

The choice of this particular lower limit is motivated by the fact that the significance[6] of the cut is maximal at a value where the efficiency is unacceptably low, as illustrated in

[6] The product of purity and efficiency, up to a constant factor.

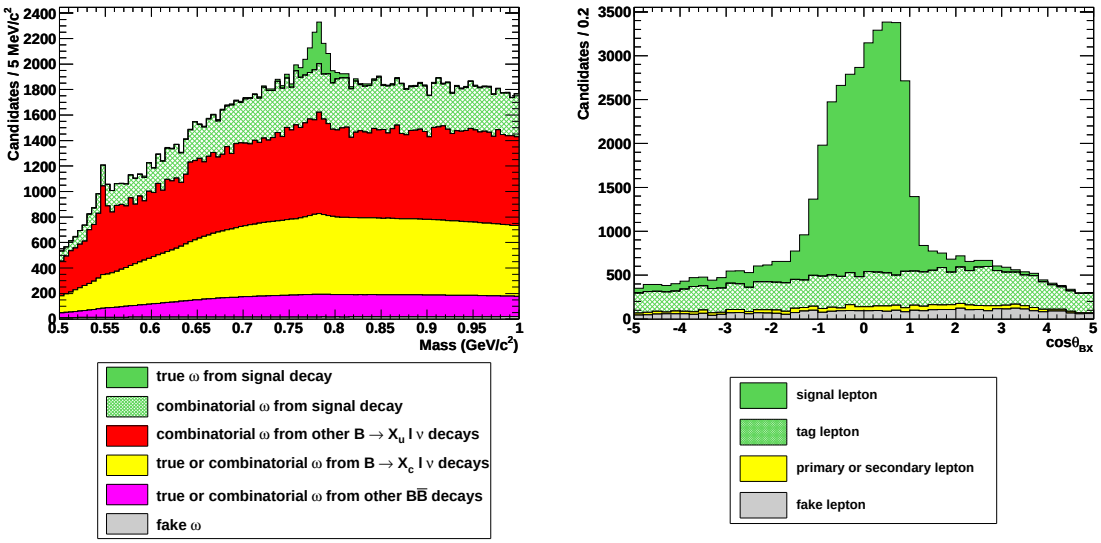

Figure 6.3: Mass of the ω candidate (left) and cosine of the angle between the signal B and the X system (right). The left plot compares true, combinatorial, and fake ω candidates from various sources, as described in the legend. Contributions from $B \to X_c \ell \nu$ and other $B\overline{B}$ decays and fake ω candidates are scaled by a factor of 10^{-3} for better illustration. On the right-hand plot, correctly reconstructed ω candidates are matched with various lepton types as listed in the legend.

Fig. 6.5. Thus a high efficiency was given priority over a potentially significant increase in purity. Studies showed that a similar constraint for the tag system is less effective and was therefore not implemented.

6.5 Event reconstruction

After the tag and signal have been reconstructed separately and quite independently, they are combined to provide a representation of the full event. Y and X systems with incompatible candidates, such as same charge leptons or overlapping tracks or neutral clusters, are excluded. The presence of two leptons in the final state allows for background from $J/\psi \to \ell^+\ell^-$ decays. We suppress this background by rejecting YX candidates that meet the following requirements:

- the two oppositely charged leptons are of the same flavor, either electrons or muons,
- their vertex probability is at least 1%,
- the cosine of the angle between them is less than 0.5: $\cos\theta_{\ell^+\ell^-} < 0.5$ (they preferentially propagate in opposite directions), and
- their invariant mass is within 30 MeV/c^2 of the J/ψ mass: $|m_{\ell^+\ell^-} - m_{J/\psi}| \leq 25\,\mathrm{MeV}/c^2$.

To motivate these cuts, the mass distribution of the lepton-lepton combination and the cosine of the angle between the two leptons are shown in Fig. 6.6. Lepton pairs from photon conversions are suppressed by rejecting YX candidates if their two leptons propagate almost collinearly in the laboratory frame, i.e. if $\cos\theta_{\ell^+\ell^-} > 0.99$ (see also Fig. 6.6).

Before making the final selection, we narrow down the list of YX candidates by imposing tighter mass requirements for both hadron candidates. The mass of the D

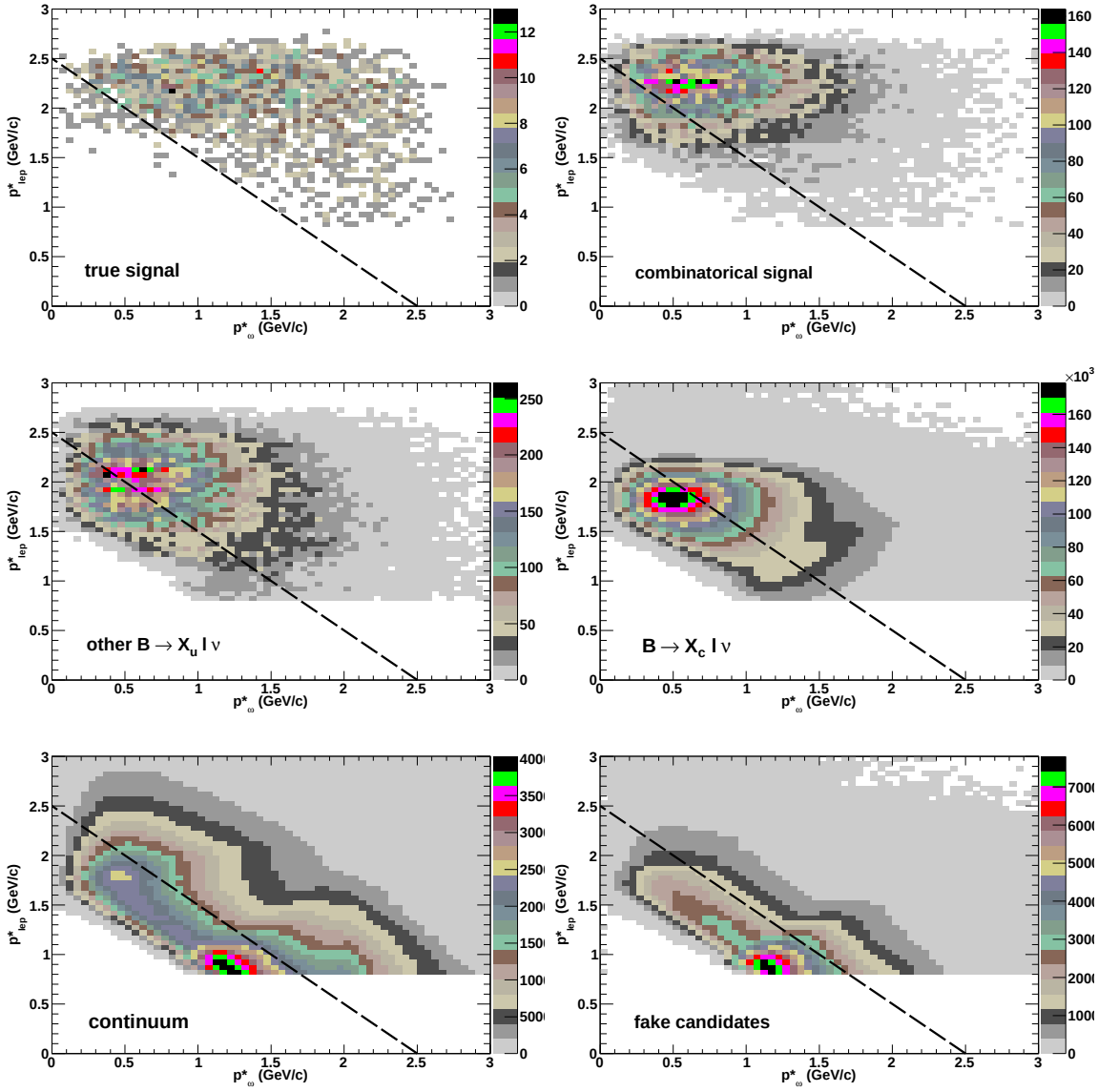

Figure 6.4: CM momentum of the lepton candidate (ordinate) versus that of the ω candidate (abscissa) for various event types. Top left = true signal, top right = combinatorical signal, center left = $B \to X_u \ell \nu$ background, center right = $B \to X_c \ell \nu$ background, bottom left = continuum background, bottom right = background from fake candidates. The dashed line indicates the lower limit cut on the sum of both momenta.

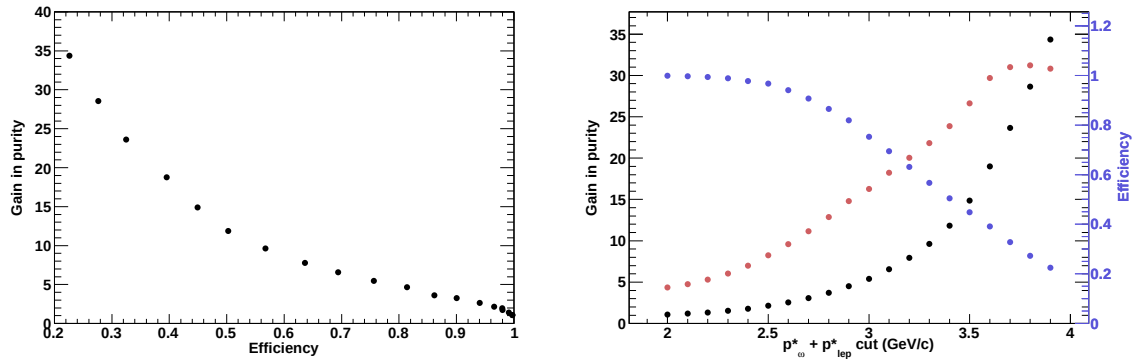

Figure 6.5: Efficiency and gain in purity of the cut on the sum of ω and lepton momentum in the CM frame. The left plot shows the gain in purity (w.r.t. the purity before the cut) vs. the efficiency of the cut. The right plot shows the gain in purity (black), efficiency (blue) and significance (auburn, in arbirtary units) as a function of the cut value.

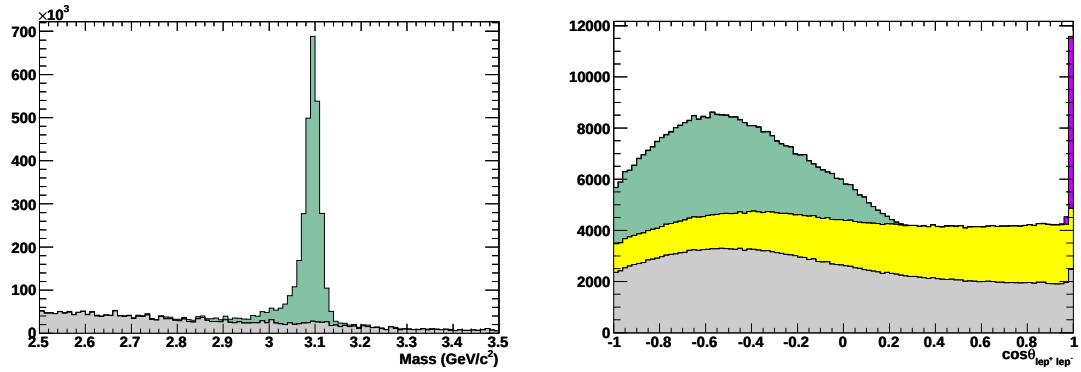

Figure 6.6: Invariant mass distribution of various lepton-lepton combinations (left) and cosine of the angle between them in the laboratory frame (right). Leptons originating from a J/ψ are depicted green, pair-produced leptons from photon conversions violet, yellow if both leptons originate from a B meson, and all other combinations are depicted gray. In the right-hand plot, the two latter contributions have been scaled by a factor 1/10 for illustration.

candidate (or the D daughter of the D^* candidate) must be within the limits listed in Table 6.2, where we allow a wider mass window for the $D^0 \to K^- \pi^+ \pi^0$ mode, due to the presence of a neutral π^0 candidate with poorer energy resolution; the ω candidate must meet the requirement $0.75 \leq m_\omega \leq 0.81\,\mathrm{GeV}/c^2$. We also place an upper limit on the cosine of the tag side angle $\theta_{BY^{(*)}}$, requiring $\cos\theta_{BY^{(*)}} \leq 2$.

Since the final state is fully reconstructed[7] as a YX candidate, there should, for a correctly reconstructed event, be no candidates left in the event that are not associated with any of the final state candidates. We will refer to those candidates as the remaining part of the event. We find the number of charged tracks in the remaining part of the event by counting all charged tracks that don't overlap with any of the identified charged final state candidates. The distribution of these remaining tracks (and the closely related sum of their charges) is shown in Fig. 6.8 for various signal and background sources.

The residual energy[8] of the event is obtained by summing up the energies of all clusters from the `GoodPhotonLoose` list that do not overlap with any of the identified neutral final state candidates; Fig. 6.9 shows its distribution for various MC data samples. Since, in the event selection, photons were required to have a minumum energy of 50 MeV,[9] the residual energy must be zero (if no photon is left in the event) or greater than this limit (if at least one photon is found).

MC studies were performed for various combinations of remaining track and residual energy cuts, the results of which in terms of efficiency and purity are illustrated in Fig. 6.10. It is clear that the efficiency mostly depends on the cut on residual energy, whereas the cut on remaining tracks has a bigger effect on the purity. We decided to require no remaining tracks in the event and the residual energy to be less than 200 MeV.

[7] except for the undetected neutrinos.
[8] not to be confused with the missing energy of the two neutrinos
[9] see Section 5.

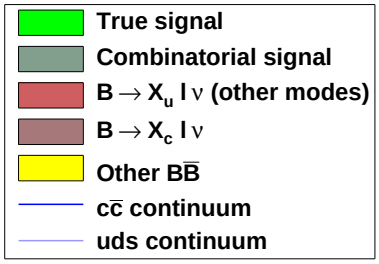

Figure 6.7: Legend for Figures 6.8 and 6.9.

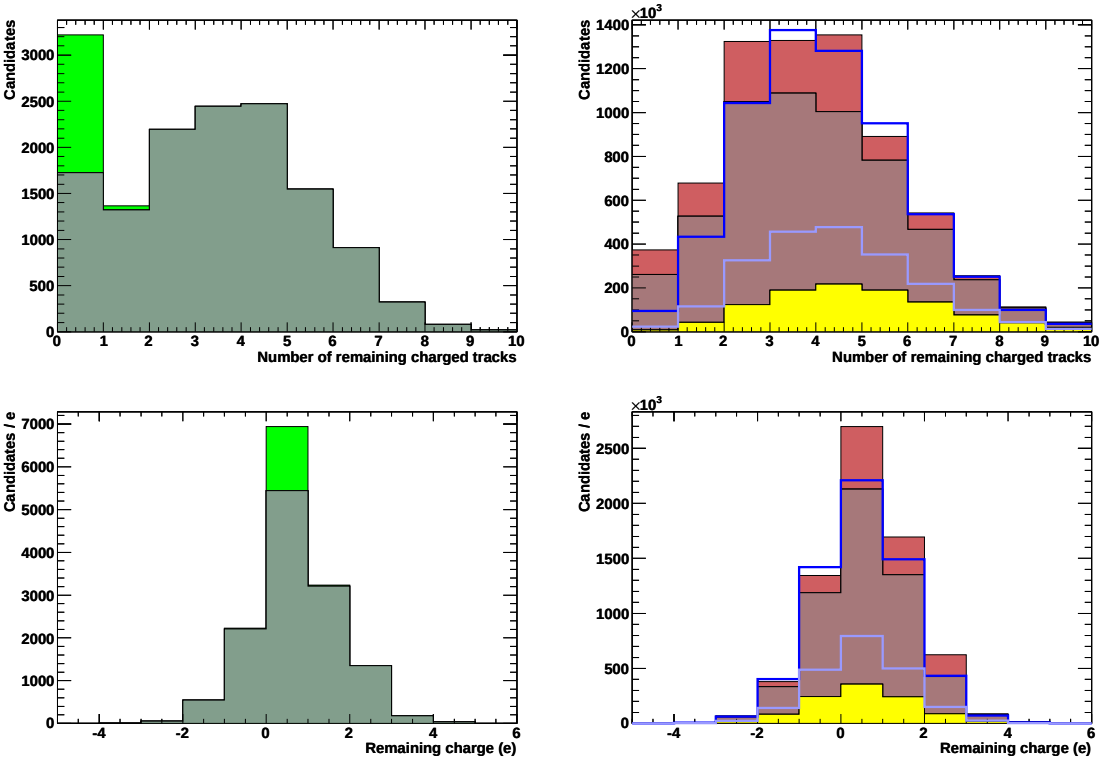

Figure 6.8: Number of charged tracks (top row) and sum of charges (bottom row) in the remaining part of the event for signal (left column) and generic $B\overline{B}$ and continuum (right column) events. For a legend see Fig. 6.7.

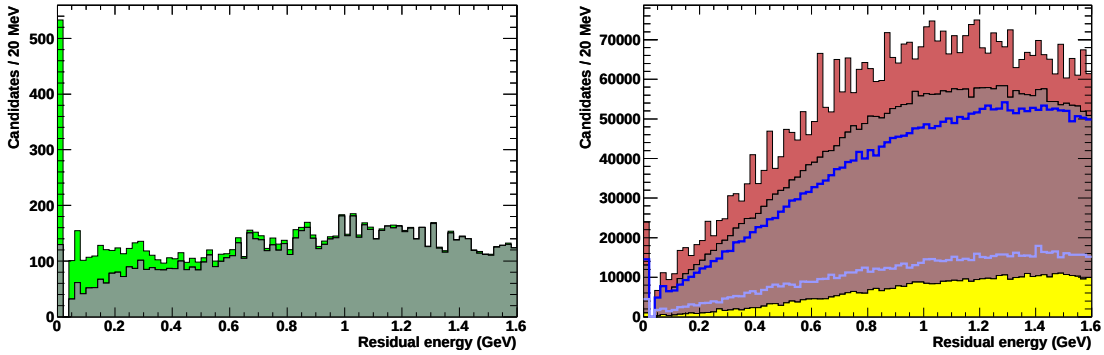

Figure 6.9: Residual energy $\sum E_\gamma$ in the remaining part of the event for signal (left) and generic $B\overline{B}$ and continuum (right) events. For the legend see Fig. 6.7. The gap below 50 MeV stems from the momentum cut applied to the photons in the event selection.

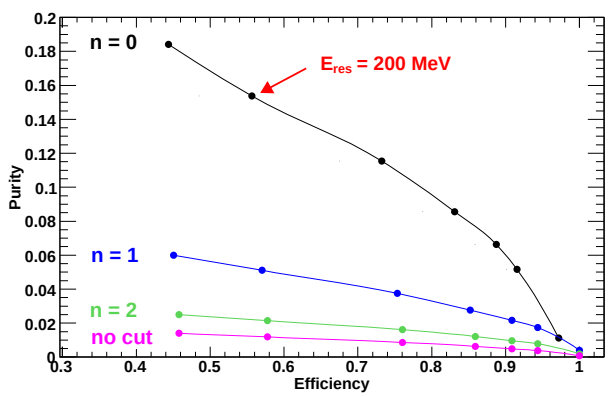

Figure 6.10: Purity vs. efficiency of remaining tracks and residual energy cuts. Each graph represents the variation of energy cuts for the indicated track cut, with $N_{\text{track}} \leq n$, and the energy cut increasing from 100 MeV on the left to 600 MeV on the right in steps of 100 MeV (the rightmost data points correspond to no energy cut). The red arrow indicates the selected combination of cuts.

6.6 Final candidate selection

If there is more than one YX candidate passing all the previous requirements, we have to choose the "best" one with an appropriate selection method. We tested several algorithms on simulated data to find the most efficient one. We found the differences between these methods rather small, and decided to use the algorithm that was simple to implement and also the most efficient one. The selection criterion that had the biggest impact was to limit the candidate pool to those containing a Y^* candidate on the tag side, provided there was such a candidate. The reconstruction efficiency for $B \to D^*\ell\nu$ decays is much smaller than for $B \to D\ell\nu$ decays because of the low reconstruction efficiency of the soft π^0 daughter of the D^*; it is also clear from Fig. 6.2 (bottom right), that the quantity $\cos\theta_{BY^{(*)}}$ is not a good discriminator between the correctly reconstructed Y^* and its (incompletely reconstructed) Y "daughter". It thus makes sense to remove from further consideration any Y candidate if a corresponding Y^* candidate passing the very selective $m_{D^*} - m_D$ cut was found.

After imposing this constraint, we select those candidates with the smallest deviation of the D mass from its nominal value. If several candidates fall into this category (for instance if the same D candidate is combined with different leptons or different X candidates), we select that candidate with the smallest absolute value of $\cos\theta_{BY^{(*)}}$ and $\cos\theta_{BX}$, in that order. Once the best candidate is selected, it is required to have the variable $\cos^2\Phi_B$[10] within the range ($\cos^2\Phi_B \leq 20$) over which the signal yield is extracted.

6.7 Efficiencies

The final selection efficiencies for the different data samples are listed in Table 6.3, for data and MC simulation. The most dominant background contributions arise

[10] See Section 8.1 for a definition of this quantity.

from CKM-favored $B \to X_c \ell \nu$ decays. The mismatch between off-peak data and $q\overline{q}$ MC efficiencies is due to the known poor modeling of simulated continuum events.

Table 6.3: Relative selection efficiencies for various data samples: shown are the number of events (unscaled) passing a given selection criterion. It shows that the most dominant background contribution comes from $B \to X_c \ell \nu$ decays.

Selection criterion	MC					data	
	signal	X_u	X_c	$B\overline{B}$	$q\overline{q}$	on-peak	off-peak
Event selection	11935	37744	18007722	2404657	3919066	8753883	237500
Final state fully reconstructed	2604	5465	3429870	780273	682608	1667720	0
$(p^*_\omega + p^*_\ell) \geq 2.5\,\mathrm{GeV}/c$	2419	4626	2119973	505297	481242	1065920	0
J/ψ veto	2405	4591	2104590	341497	479468	1001461	0
photon conversion veto: $\cos\theta_{\ell^+\ell^-} \leq 0.99$	2401	4572	2099402	338954	439119	966341	0
D mass cut	1751	3111	1404859	229226	276105	633897	0
ω mass cut	1076	797	391885	70831	74671	175763	0
$\cos\theta_{BY^{(*)}} \leq 2$	994	671	340790	58789	55961	146983	0
no remaining tracks	687	132	33553	768	2191	11556	0
residual energy cut	279	17	1305	7	38	626	0
$\cos^2\Phi_B \leq 20$	273	10	924	2	26	474	0

Chapter 7

Data Monte-Carlo Comparison

7.1 Double tag correction

The $D\ell$ tagging efficiency is known to be different in data and simulation. To take this into account, we study "double tag" events, i.e. $B\overline{B}$ events where both B mesons decay semileptonically to $D^{(*)}\ell\nu$, and then compare the efficiceny in data to that found in MC. Assuming that the tagging efficiency for each B decay is independent of the other, the data-MC correction factor for the (single) tag efficiency is

$$r_{\varepsilon}^{\text{tag}} = \sqrt{\frac{N_{\text{data}}}{N_{\text{MC}}}} \tag{7.1}$$

where N_{data} (N_{MC}) is the number of double tag events found in data (MC).

The two $D^{(*)}\ell$ tag candidates have to be charge-compatible and non-overlapping, and have to satisfy the same selection requirements outlined in section 6.3, with the same cuts applied to the tracks and photons. We also require no remaining tracks to be found in the event. It is assumed that the extra neutral energy in the event typically comes from the tag side (from $B \to D^{**}\ell\nu$ decays). Therefore, and since we found the result to be very stable with respect to variations in this cut, we impose no cut on the extra energy, for maximum statistics.

In case several double tag pairs pass all selection criteria, we find the "best" candidate pair in the following way: we find the deviation of the D candidate's mass from its nominal value, and require the sum of both differences to be minimal, and

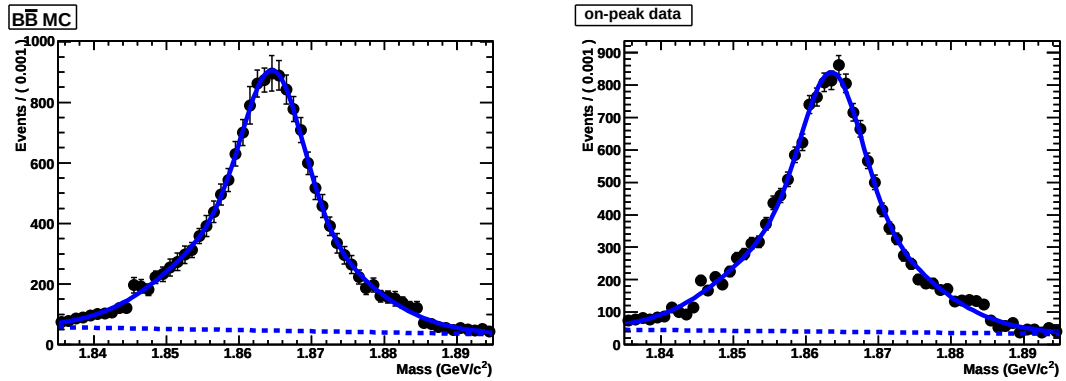

Figure 7.1: Fit of the D mass distribution for $B\overline{B}$ MC (left) and on-peak data (right) for the double tag study. The dashed line represents the background level.

similarly for the sum of the absolute values of the two $\cos\theta_{BY}$ values. The number of double tag events is found by a binned extended maximum likelihood fit of the D mass with a double Gaussian signal component and a second order polynomial for the background component. The fit results are displayed in Fig. 7.1. With the data and MC yields, $N_{\rm data} = 14618 \pm 350$ and $N_{\rm MC} = 15441 \pm 335$, we obtain

$$r_{\varepsilon}^{\rm tag} = 0.973 \pm 0.016 \tag{7.2}$$

where the error is statistical. This factor corrects for differences in tagging efficiency, including reconstruction and all tag side branching fractions.

7.2 Comparison of data and MC simulation

Figures 7.3 through 7.6 display comparisons of on-peak data to MC simulated data of certain selection variables at various stages of the selection process. In each plot, MC samples are scaled to the luminosity of the on-peak data. The color code for the various signal and background contributions is given in Fig. 7.2.

The agreement between data and MC is reasonably good for the selected final events; however, there is a clear discrepancy for those plots at an earlier stage in the event selection. This can be explained by the fact that continuum events are completely

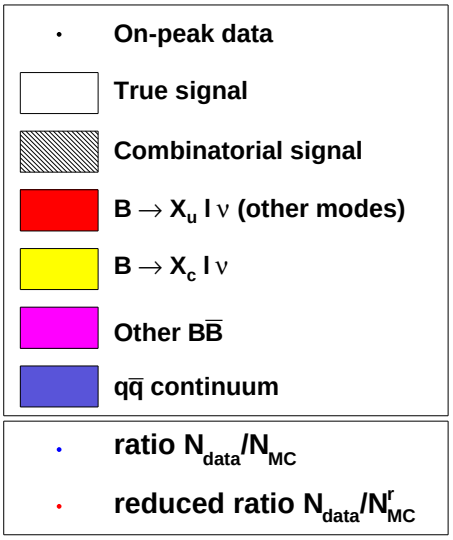

Figure 7.2: Legend for Figures 7.3 - 7.6. The top part refers to the stacked histograms, and the bottom part to the bin-by-bin ratios. See the text for an explanation of the reduced ratio.

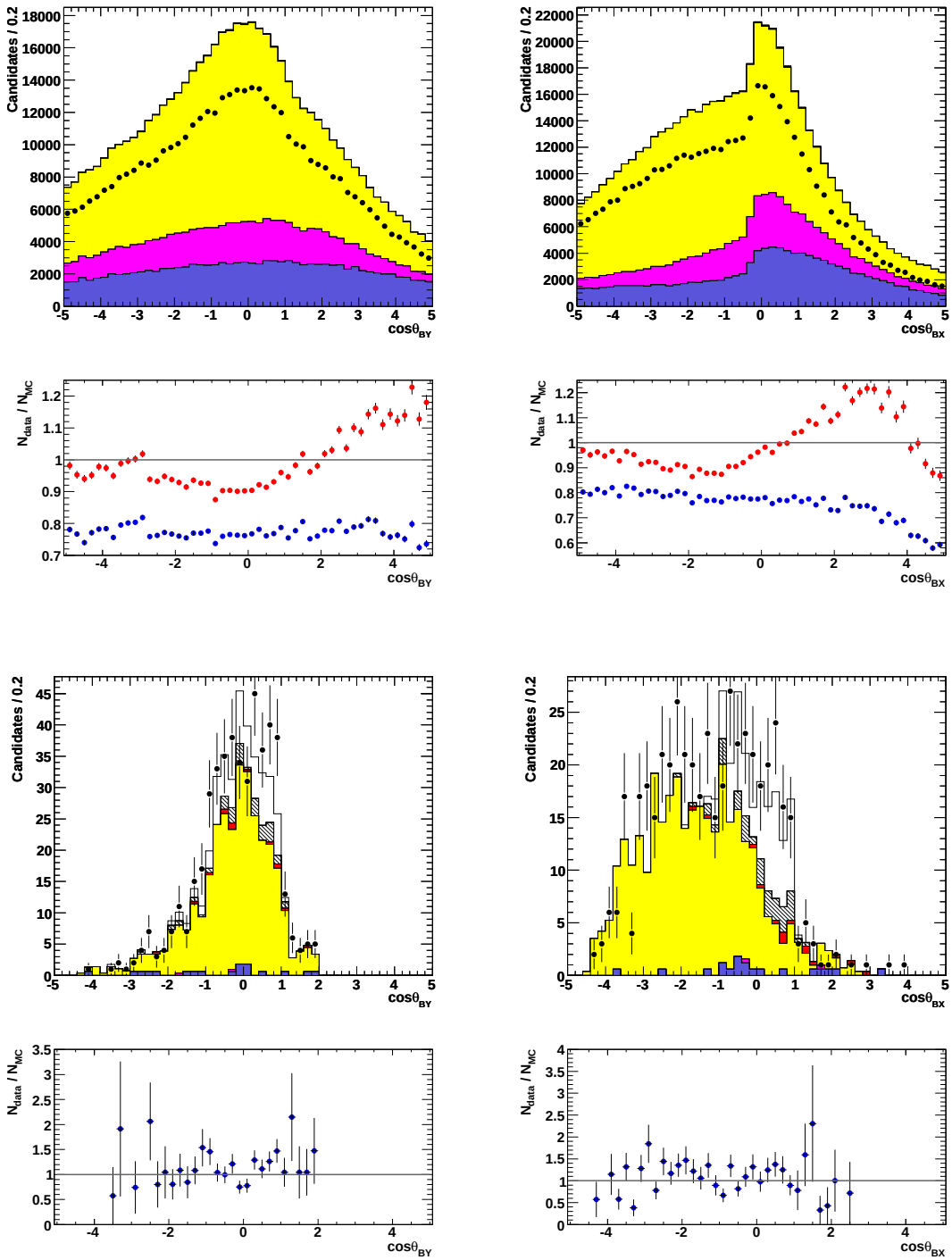

Figure 7.3: Data MC comparison of $\cos\theta_{BY}$ (left column) and $\cos\theta_{BX}$ (right column) after the ω mass cut (top row) and for the selected event (bottom row). Beneath each plot is the ratio of on-peak data over MC. For a legend see Fig. 7.2.

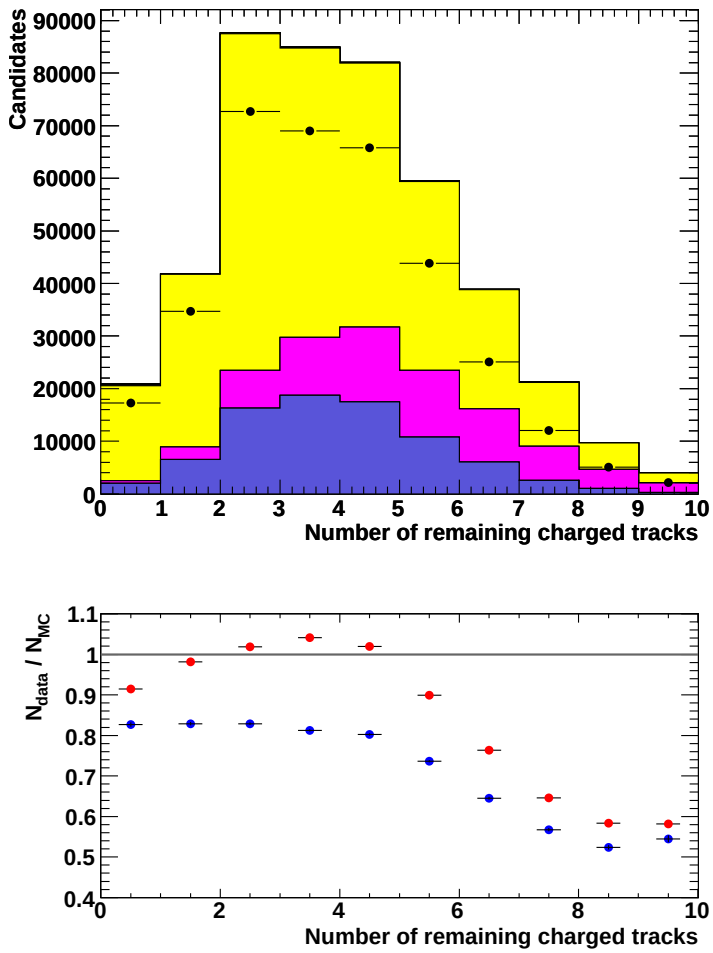

Figure 7.4: Data MC comparison of the number of remaining charged tracks before that cut is applied, and ratios of on-peak data over full and reduced MC. For a legend see Fig. 7.2.

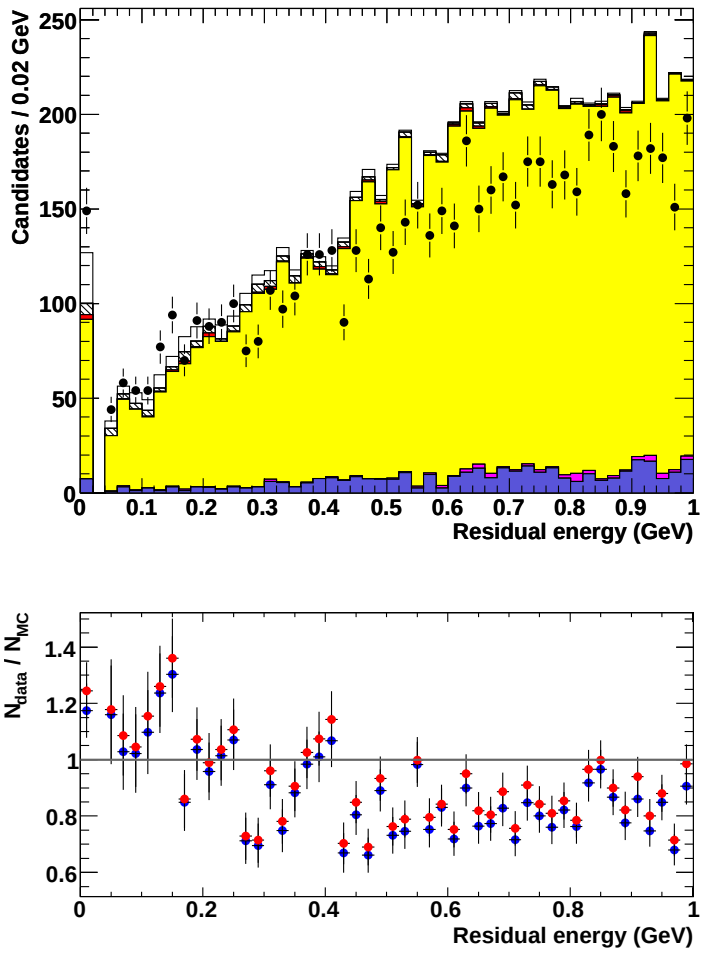

Figure 7.5: Data MC comparison of residual energy before that cut is applied, and ratios of on-peak data over full and reduced MC. For a legend see Fig. 7.2.

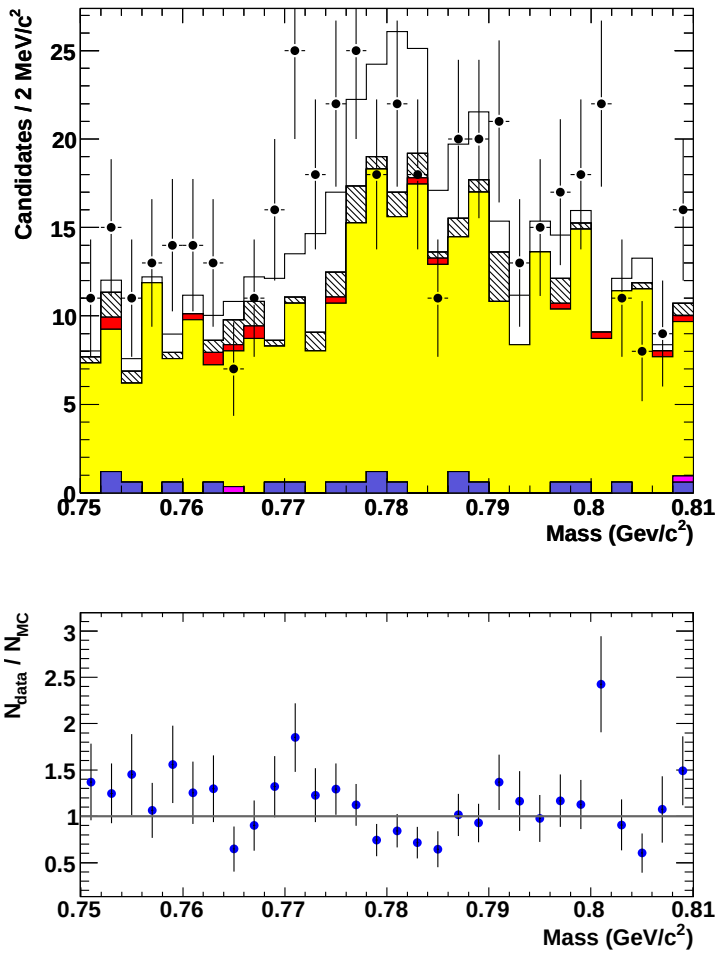

Figure 7.6: Data MC comparison of the mass of the selected ω candidate, and ratio of on-peak data over MC. For a legend see Fig. 7.2.

lacking from the final data sample (no off-peak data pass the event selection), whereas, due to its much higher luminosity, a good number of MC continuum events pass that selection. This is a manifestation of the known fact that the continuum contribution is not well modeled in the simulation.

The ratio of the number of events in on-peak data over the number of events in MC simulated data for each bin is displayed beneath each plot. The points in blue represent this ratio including contributions from all MC sources, whereas the points in red represent the *reduced* ratio, where the sum over MC sources excludes the continuum contribution.[1] The agreement between data and MC is clearly better for the reduced ratio.

[1] If there is no significant contribution from the continuum, as is the case for the selected final events, the reduced ratio is not shown.

Chapter 8

Yield Extraction

8.1 Fit method

The two momentum vectors of the reconstruced Y and X systems together define a plane. The angles between either system and its corresponding B meson (in the CM frame), θ_{BY} and θ_{BX}, were calculated in Section 6.3 using the known beam energies, so that the B direction is constrained to a cone around $\boldsymbol{p}^*_{Y(X)}$ with angle $\theta_{BY(X)}$. This information, together with the requirement that tag and signal B mesons emerge back-to-back, determines the direction of either B meson up to a two-fold ambiguity.[1] A schematic of the event kinematics is shown in Fig. 8.1.

The angle between the $Y - X$ plane and either $\boldsymbol{p}^*_B$ possibility, denoted by Φ_B, is

[1] Two nondegenerate circles on the surface of a sphere (in this case of radius $|\boldsymbol{p}^*_B|$) have at most two points of intersection.

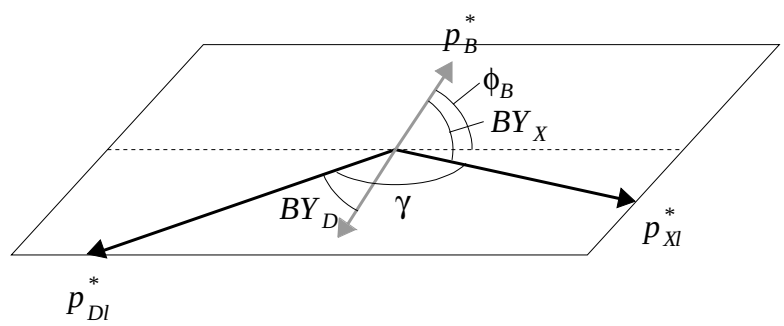

Figure 8.1: Event kinematics of a double-semileptonic decay. In the text, the angles BY_D and BY_X are referred to as θ_{BY} and θ_{BX}, respectively, and the $D\ell$ and $X\ell$ systems are referred to as Y and X, respectively.

derived in Appendix A.2 to be

$$\cos^2\Phi_B = \frac{\cos^2\theta_{BY} + 2\cos\theta_{BY}\cos\theta_{BX}\cos\gamma + \cos^2\theta_{BX}}{1-\cos^2\gamma} \tag{8.1}$$

where γ is the angle between the Y and X momenta. Events consistent with the hypothesis of two semileptonic $B \to Y(X)\ell\nu$ decays have therefore, up to experimental resolution, $\cos^2\Phi_B \leq 1$.

This quantity $x \equiv \cos^2\Phi_B$ is used as the discriminating variable to extract the signal yield. The yield is determined through a fit in the range $0 \leq x \leq 20$, where different contributions from various sources are distinguished:

- Signal events are MC generated signal events that have been correctly reconstructed on both the tag and the signal side.
- Background events are other MC $B\overline{B}$ events where the tag or the signal have not been reconstructed correctly.
- Continuum background events are those MC continuum events where both tag and signal have been incorrectly reconstructed and passed all selection criteria.
- Data events are on-peak data events such that both tag and signal candidates have been identified and passed all selection criteria.

The first three subsets are fitted independently by appropriate probability density functions (PDFs), which are normalized analytic functions that describe the shape of the specific distribution. The following PDFs are used in this analysis:

- The signal PDF is parametrized as a threshold function in the physical region ($0 \leq x \leq 1$) with finite resolution and an exponential tail:

$$\mathcal{P}_{\text{sig}} \propto \frac{1-\text{erf}[p_0\log(p_1 x)]}{2} + p_2 \mathrm{e}^{-p_3 x} \tag{8.2}$$

- The background PDF is given as an exponential with a nonnegative constant term:

$$\mathcal{P}_{\text{bkg}} \propto \mathrm{e}^{-p_4 x} + p_5^2 \tag{8.3}$$

- The continuum PDF $\mathcal{P}_{\text{cont}}$ is modeled in the same way as the background PDF:

$$\mathcal{P}_{\text{cont}} \propto \mathrm{e}^{-p_6 x} + p_7^2 \tag{8.4}$$

The on-peak data sample is an admixture of events from these three sources, with their relative contributions given by the respective yield. The fit technique used in this analysis is an extended binned maximum-likelihood fit, which maximizes the likelihood $\mathcal{L}$ that, given the data points and assuming a Poisson distribution of the number of events in each bin, the measured data is described by the underlying PDF,

$$\mathcal{L}(\{N_j\}, \boldsymbol{p}) = \prod_{b=1}^{m} \frac{\left(\sum_j N_j \mathcal{P}_j(x_b; \boldsymbol{p})\right)^{N_b} \mathrm{e}^{-\sum_j N_j \mathcal{P}_j(x_b; \boldsymbol{p})}}{N_b!} \tag{8.5}$$

where $\{N_j\}$ and $\boldsymbol{p} \equiv (p_0, p_1, \ldots, p_7)$ are the sets of yield and fit parameters, respectively (here $j = \{\text{sig}, \text{bkg}, \text{cont}\}$), m is the number of bins, N_b is the number of data events in bin b, and $\mathcal{P}_j(x_b; \boldsymbol{p})$ is the corresponding PDF for source j, integrated over bin b (and is a function of the fit parameters $\boldsymbol{p}$).

8.2 Fit result

The PDF parameters are obtained by fitting the three MC samples separately; after the fit, the fit parameters $\boldsymbol{p}$ are held constant, so as to keep the shape of the PDF fixed. The yield of the continuum background, N_{cont}, is obtained from the continuum MC sample, adjusted for luminosity, and fixed in the fit. The number of continuum background events selected, 19 from the $c\bar{c}$ sample and zero from the *uds* and $\tau^+\tau^-$ samples, yields, adjusted for luminosity, an expected number of 1.2 events for the off-peak data, consistent with the number of events selected from the off-peak sample,

Table 8.1: Fit results for signal and background yields. Luminosity-scaled MC refers to the fit results after scaling the MC dataset (referred to as raw MC, with the continuum contribution scaled to the generic $B\overline{B}$ luminosity) to match the luminosity of the on-peak data.

	raw MC		luminosity-scaled MC		data
	fit	MC Truth	fit	MC Truth	
$N_{\rm sig}$	282 ± 26	270	98 ± 15	94.5	100 ± 16
$N_{\rm bkg}$	954 ± 37	966	333 ± 22	338.1	370 ± 23
$N_{\rm cont}$	46	46	16	16	16

zero. The signal and background yields, $N_{\rm sig}$ and $N_{\rm bkg}$, are allowed to float freely in the fit. Figure 8.2 shows the results of the fit to the MC. We obtain a signal yield of $N_{\rm sig} = 282 \pm 26$ and a background yield of $N_{\rm bkg} = 954 \pm 37$ (the continuum yield $N_{\rm cont} = 46$ is fixed); the number of true signal events is 270, and the number of $B\overline{B}$ background events is 966. When scaled to the luminosity of the on-peak data, these numbers translate to those quoted in Table 8.1. These numbers are obtained from the generic $B\overline{B}$ MC sample rather than the signal MC sample, since it uses a more realistic model[2] for the signal decay q^2 spectrum. The same combination of PDFs, with their individual parameters fixed, is then fitted to the on-peak data; results are presented in Fig. 8.3, along with the luminosity-adjusted results of the MC sample for comparison.

The $\cos^2\Phi_B$ distribution is compared in Fig. 8.4 for data and the various MC contributions. The agreement is reasonably good within the limited statistics.

The reconstruction efficiency is given by

$$\begin{aligned}\varepsilon = \frac{N_{\rm sig}^{\rm MC}}{N_{\rm generated}^{\rm MC}} &= \frac{N_{\rm sig}^{\rm MC}}{4 \cdot N_{B^+B^-} \cdot \mathcal{B}(B \to \omega\ell\nu) \cdot \mathcal{B}(\omega \to \pi^+\pi^-\pi^0)} \\ &= \frac{270}{4 \cdot 670.1 \cdot 10^6 \cdot 1.45 \cdot 10^{-4} \cdot 0.892} = 7.79 \cdot 10^{-4} \qquad (8.6)\end{aligned}$$

where $N_{\rm sig}^{\rm MC}$ and $N_{\rm generated}^{\rm MC}$ refer to the number of selected true signal events and the number of generated signal events in the MC sample, respectively.[3] A factor of 2 arises

[2] based on ISGW2 (see Section 2.3.2) and PHOTOS to include final state radiation.

[3] The *BABAR* event generator assumes a branching fraction of $1.45 \cdot 10^{-4}$ for the $B \to \omega\ell\nu$ decay.

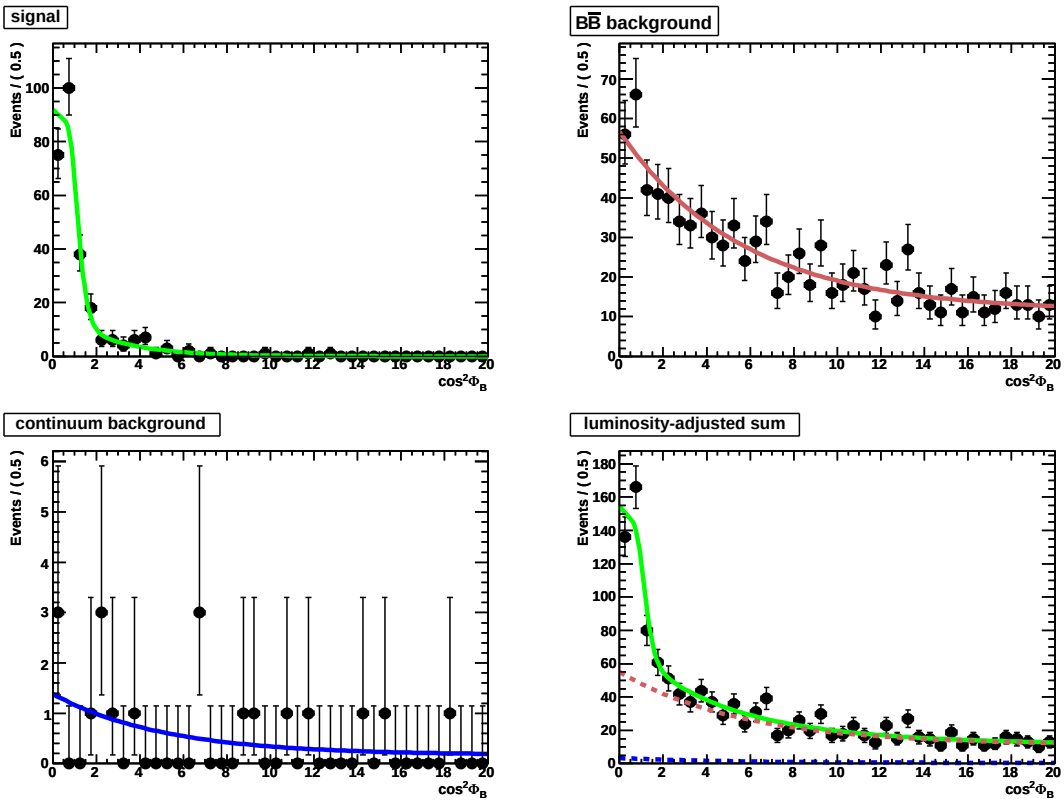

Figure 8.2: Distributions of $\cos^2\Phi_B$ for various sources and their corresponding PDFs. The PDFs are fitted separately for each source and then their parameters are fixed. The bottom right plot shows a simultaneous fit to the sum of the three contributions, with the continuum contribution scaled to the luminosity of the $B\overline{B}$ sample and its yield fixed before the fit.

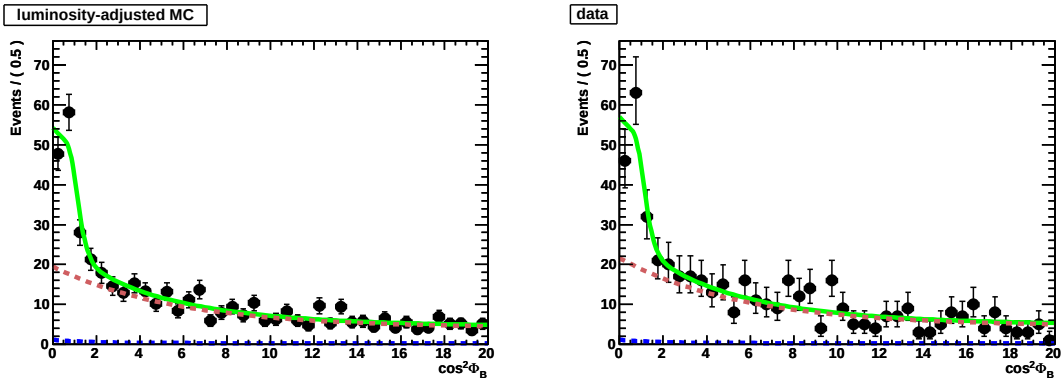

Figure 8.3: Yield extraction fit on MC and data. The PDFs are fitted separately for each source and then their parameters are fixed. The left-hand plot shows a simultaneous fit to the sum of the three MC contributions, with the luminosity scaled to the on-peak data; the right-hand plot shows the fit to the data.

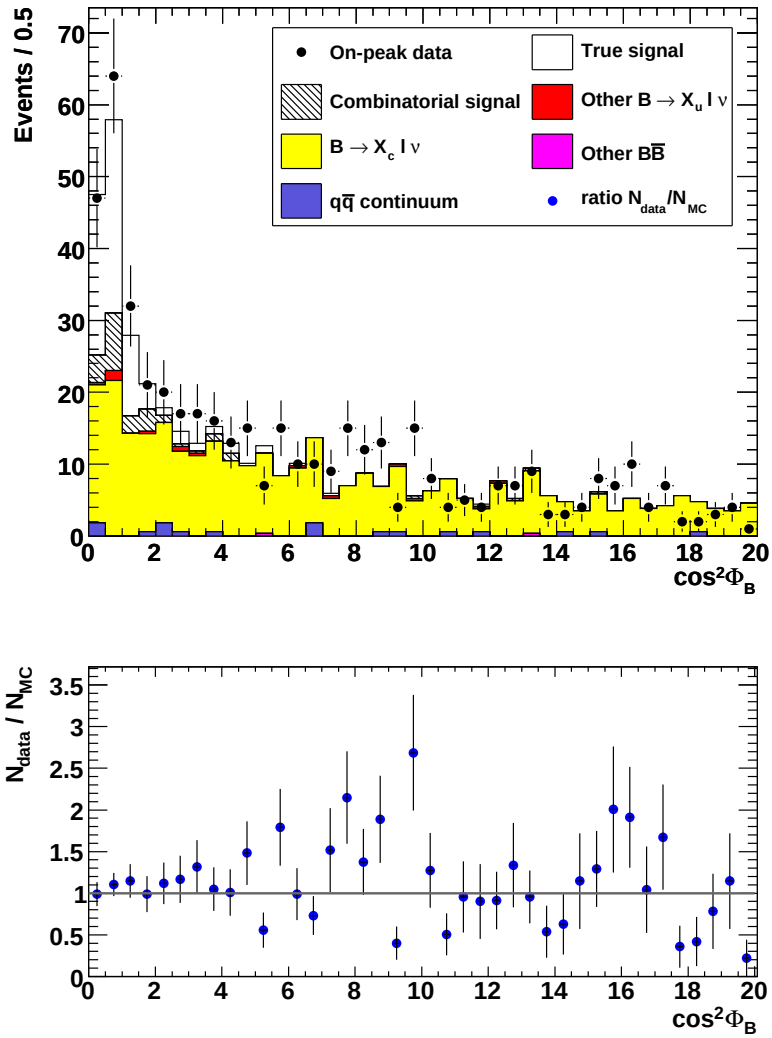

Figure 8.4: Distribution of $\cos^2 \Phi_B$ for data and MC, and bin-by-bin ratio of data over MC. The various signal and background contributions are given in the legend, and are the same as in Figures 7.3 - 7.6.

from the fact that either B meson can decay into the signal mode, and another factor of 2 from the fact that one has to add the (numerically identical) electron and muon contributions. Given the reconstruction efficiency, and using the signal yield from the data sample, $N_{\rm sig}^{\rm data} = 100$, and the tag efficiency correction factor $r_\varepsilon^{\rm tag}$ from Section 7.1, we obtain a branching fraction of

$$\begin{aligned}\mathcal{B}(B \to \omega\ell\nu) &= \frac{N_{\rm sig,true}^{\rm data}}{N_{\rm recorded}^{\rm data}} = \frac{(N_{\rm sig,measured}^{\rm data}/\varepsilon)\cdot r_\varepsilon^{\rm tag}}{2\cdot(f_{+-}/f_{00})\cdot N_{B\overline{B}}\cdot\mathcal{B}(\omega\to\pi^+\pi^-\pi^0)} \\ &= \frac{100/(7.79\cdot 10^{-4})\cdot 0.973}{2\cdot 1.064\cdot 467.8\cdot 10^6\cdot 0.892} = (1.41\pm 0.23)\cdot 10^{-4} \qquad (8.7)\end{aligned}$$

where the quoted error is statistical. Here, one factor of 2 is canceled by the fact that approximately half the $\Upsilon(4S)$ decay into neutral B meson pairs; the exact number of charged B meson pairs in the data sample is obtained by applying the correction factor $f_{+-}/f_{00} = 1.064\pm 0.029$, the ratio of the $\Upsilon(4S) \to B^+B^-$ and $\Upsilon(4S) \to B^0\overline{B}^0$ branching fractions [9].

8.3 Fit validation

The stability of the fit method with respect to variations in the number of signal or background events is tested with toy MC studies. For each toy experiment, the PDF parameters are taken from the results of the fit procedure described in the previous section. The individual signal, background, and continuum yields are fluctuated randomly around their expected value acoording to Poisson statistics; a toy MC sample is then generated as the sum of those contributions. The fit is then applied to obtain the yields $\{N_j\}$ and their associated uncertainties $\{\sigma_{N_j}\}$. The pull for the yield N_j is defined as

$$\text{pull}(N_j) = \frac{N_j - \langle N_j\rangle}{\sigma_{N_j}} \qquad (8.8)$$

and is plotted in Fig. 8.5 along with a Gaussian fit for the signal and background yields. Both show good agreement with the expected mean of zero; however, the background

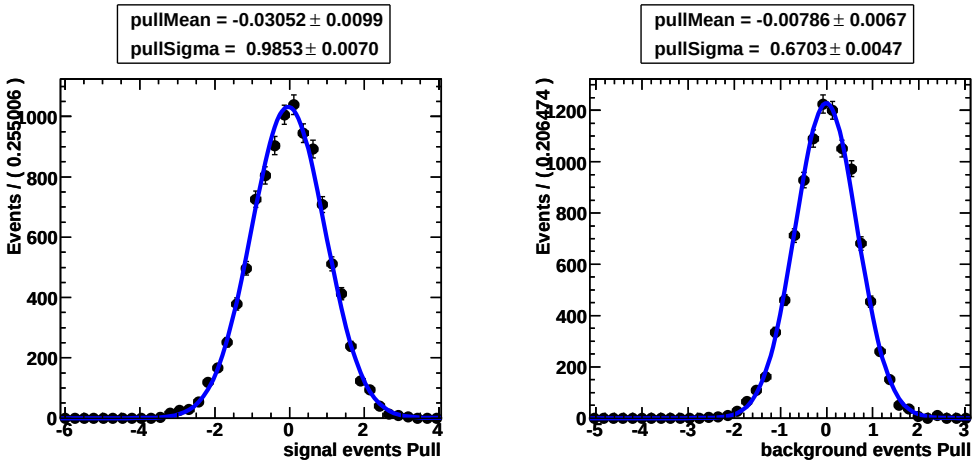

Figure 8.5: Pull distribution of signal (left) and background (right) yields for 10,000 toy MC events.

yield has a significantly smaller standard deviation than the expected unity. This is an indication that the fit error on it is overestimated.

Chapter 9

Systematic Uncertainties

9.1 Stability of the fit

We perform several tests to estimate the uncertainties related to the yield extraction of Chapter 8. Since the eight parameters p are fixed after being fit to the corresponding MC sample, we vary each parameter individually by its uncertainty and observe the stability of the fit yields. The strongest impact was found by varying the background parameters, which gave a maximum deviation of four events in the signal yield. As discussed in section 7.2, we observe a significant discrepancy between data and MC, mostly due to poor modeling of the continuum background. We therefore vary the value of the continuum yield, which is fixed in the fit, from zero to twice its nominal value, and found only small deviations.[1] Additionally, we changed the functional forms of the background and continuum PDFs to polynomials and repeated the fit; only small differences were observed. The fit bias is taken from the fit validation in Section 8.3: the 3% bias in the signal pull translates into an absolute bias of 0.5%.

9.2 Uncertainties in detector response and reconstruction

Uncertainties in the modeling of the detector response, and in the reconstruction efficiencies of charged and neutral particles, contribute to the overall systematic errors.

[1] Due to the similar functional form of the background and continuum PDFs, most of these events are absorbed into the background yield.

9.2.1 Tracking efficiency

The difference in track reconstruction efficiency between data and MC is taken as a source of systematic uncertainty. The Tau3-1 tracking efficiency method utilizes $\tau^+\tau^-$ events with a 1 vs. 3 topology to determine the tracking efficiency for each Run separately. Averaged over Run periods, it is found to be 0.539% per track for `GoodTracksVeryLoose`, which leads[2] to the quoted tracking efficiency uncertainty of 3.4%.

9.2.2 PID efficiency

In order to account for differences in efficiencies and fake rates between data and MC simulation, an analysis is typically run in *tweaking* mode. This is a special mode of running the standard PID-selection modules which modifies the output lists such that the MC efficiencies more closely match those of the data. It rejects or accepts a given particle hypothesis depending on a probability parameter derived from PID-efficiency tables for data and MC. To estimate the systematic error of the PID efficiency, the analysis is repeated without this correction, that is in *plain* mode, and compared to the original result.

9.2.3 Neutrals efficiency

To account for differences between data and MC in reconstruction efficiencies of neutral particle candidates, corrections to the energy scale and resolution are applied at run time, and an average π^0 efficiency correction is applied at ntuple level. Studies conducted by the Neutral Reconstruction AWG suggest to apply a systematic error of 3% per π^0 for the average efficiency correction. An additional systematic is incurred by neglecting the weak variation of the efficiency with π^0 momentum, estimated to be 1.5%

[2] averaged over the three reconstructed D modes with six or seven tracks, weighted by their relative abundance in the final sample.

per π^0 and added in quadrature [56, 57]. Averaging over the three tag modes with one and two π^0 candidates, respectively, in the final state, yields the quoted uncertainty of 3.8%.

9.3 Other uncertainties

The number of $B\overline{B}$ events in data is obtained by subtracting the luminosity-scaled numbers of hadronic events in on- and off-peak data samples, corrected for the $B\overline{B}$ efficiency. The uncertainty of 1.1% in that number translates directly to an error of 1.1% in the branching fraction.

The calculation of the overall reconstruction efficiency (Eq. 8.6) involves the $B \to \omega\ell\nu$ branching fraction. The impact of the uncertainties in the $B \to D^{(*)}\ell\nu$ branching fractions is estimated by varying these while preserving the total $b \to c\ell\nu$ branching fraction. The effect on the final branching fraction of the uncertainty in the ratio of the $\Upsilon(4S) \to B^+B^-$ and $\Upsilon(4S) \to B^0\overline{B}^0$ branching fractions, $f_{+-}/f_{00} = 1.064 \pm 0.029$ [9], is taken into account as well.

Table 9.1 summarizes the various contributions to the total systematic uncertainty of the measured branching fraction.

9.4 Comparison between electrons and muons

Another way to identify underlying systematic effects is to look at electrons and muons separately. In Fig. 9.1 we compare data and MC distributions of $\cos\theta_{BY}$ and $\cos\theta_{BX}$ for electrons and muons separately. The agreement between data and MC is sufficiently good, and no significant difference between electrons and muons is observed.

Table 9.1: Summary of the relative systematic errors of the branching fraction $\mathcal{B}(B^+ \to \omega\ell^+\nu)$.

Source of uncertainty	$\delta\mathcal{B}/\mathcal{B}$ (%)
Additive errors (events)	
Fit yield	4
Fit bias	0.5
Multiplicative errors (%)	
Tracking efficiency	3.4
PID efficiency	3.0
Neutral efficiency	3.8
B counting	1.1
$\mathcal{B}(\omega \to \pi^+\pi^-\pi^0)$	0.8
$\mathcal{B}(B \to D^{(*)}\ell\nu)$	2.1
f_{+-}/f_{00}	2.7
Total systematic error	8.0

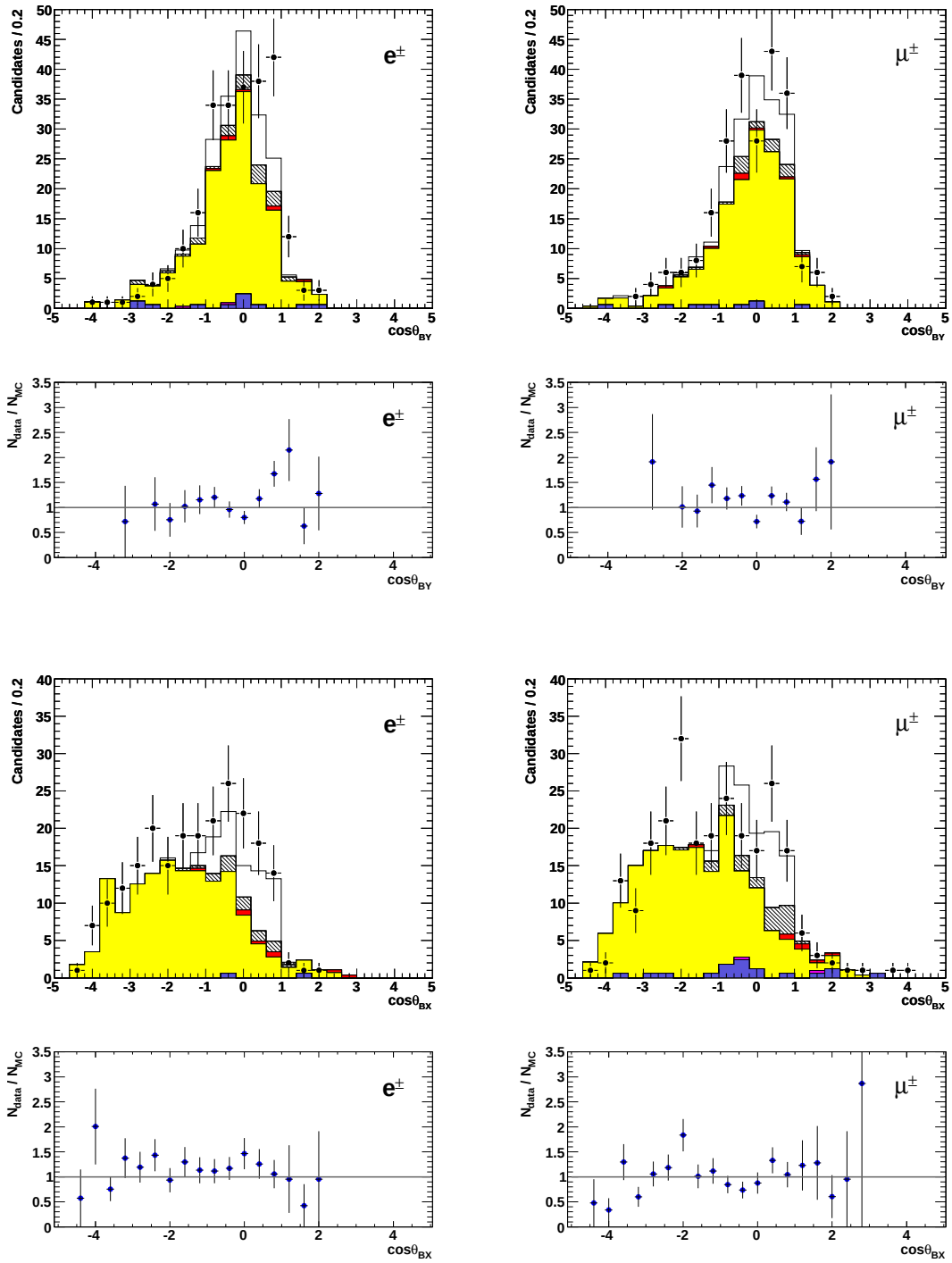

Figure 9.1: Data MC comparison of $\cos\theta_{BY}$ (top row) and $\cos\theta_{BX}$ (bottom row) for electrons (left column) and muons (right column) separately, after the final candidate selection. Beneath each plot is the ratio of on-peak data over MC. The binning has been reduced by a factor of two compared to Fig. 7.3 to take into account the lower statistics. For a legend see Fig. 7.2.

Chapter 10

Results and Discussion

10.1 Branching fraction

Using a data sample of 467.8 million $B\overline{B}$ events recorded with the *BABAR* detector, we studied the charmless semileptonic B decay $B^+ \to \omega\ell^+\nu$ with a semileptonic $B^+ \to D^{(*)}\ell^+\nu$ tag. The ω candidate was reconstructed in the dominant $\omega \to \pi^+\pi^-\pi^0$ mode. We report a total branching fraction of

$$\mathcal{B}(B^+ \to \omega\ell^+\nu) = (1.41 \pm 0.23 \pm 0.11) \cdot 10^{-4} \tag{10.1}$$

where the errors are statistical and systematic. Table 10.1 compares our result with previous measurements by the Belle and *BABAR* collaborations, respectively, employing different analysis techniques. Our result is consistent, within uncertainties, with both previous measurements.

Table 10.1: Comparison with previous results of the branching fraction $\mathcal{B}(B^+ \to \omega\ell^+\nu)$.

Measurement	$\mathcal{B}(B^+ \to \omega\ell^+\nu)$ (10^{-4})	technique
Belle [10]	$1.19 \pm 0.32 \pm 0.06$	hadronic tag
BABAR [11]	$1.14 \pm 0.16 \pm 0.08$	neutrino reconstruction
this analysis	$1.41 \pm 0.23 \pm 0.11$	semileptonic tag

10.2 Determination of $|V_{ub}|$

In order to extract the value of $|V_{ub}|$ from the measured branching fraction, we need to quantify $\Delta\zeta$ in Eq. 2.26 over the full q^2 range. Parametrizations of the q^2 dependence of the form factors, including those applicable to the hadronic $B \to \omega$ transition, are available from the method of light-cone sum rules [58]. The procedure to compute $\Delta\zeta$ in this model is outlined in Appendix B. With $\Delta\zeta = 11.87\,\mathrm{ps}^{-1}$ computed in this way and the $B^{\pm}$ lifetime $\tau_{B^{\pm}} = 1.638 \pm 0.011\,\mathrm{ps}$ [14], we obtain:

$$|V_{ub}| \ = (2.69 \pm 0.24) \cdot 10^{-3} \tag{10.2}$$

The quoted uncertainty does not include any uncertainty in $\Delta\zeta$, since uncertainty estimates of the form factor integrals are not available. The theoretical uncertainty might well be the dominant one here, since the validity of the light-cone sum rule approach in the higher q^2 range is questionable. In Table 10.2, the result for $|V_{ub}|$ is compared with various other measurements, inclusive and exclusive ones. Our result is close to similar exclusive determinations of $|V_{ub}|$, however, the discrepancy between inclusive and exclusive measurements still persists.

There seems to be an additional difference within the exclusive measurements between decays into pseudoscalar mesons (π, η, K, D) and decays into vector mesons (ρ, ω). The reason for this is probably related to the different theoretical form factors involved in the two cases, but it could also be an indication for new physics beyond the Standard Model. This interesting question could be investigated with higher statistics from a much larger dataset, which will easily be obtained e.g. by the proposed *Super B* factory currently under discussion to be built in Italy, with a projected increase in integrated luminosity of approximately two orders of magnitude compared to that recorded by *BABAR* [63]. A correspondingly larger data sample would also allow for a measurement of the branching fraction in intervals of q^2, necessary for a more precise determination of $|V_{ub}|$.

Table 10.2: Comparison of inclusive (top) and exclusive (bottom) determinations of $|V_{ub}|$ for various theoretical models. There is a general discrepancy between inclusive and exclusive results. Within the exclusive $|V_{ub}|$ determinations, there seems to be a difference between results based on $B \to$ pseudoscalar (top three) and $B \to$ vector meson (bottom three) decays.

	Theoretical model	q^2 range (Gev^2)	Decay $B \to X\ell\nu$	$\lvert V_{ub}\rvert$ (10^{-3})
inclusive	BLNP [9]			$4.06 \pm 0.15^{+0.25}_{-0.27}$
	DGE [9]			$4.25 \pm 0.15^{+0.21}_{-0.17}$
	GGOU [9]			$4.03 \pm 0.15^{+0.20}_{-0.25}$
	ADFR [9]			$3.84 \pm 0.13^{+0.23}_{-0.20}$
	BLL [9]			$4.87 \pm 0.24 \pm 0.38$
exclusive	LCSR [59]	< 16	π, K, η	$3.34 \pm 0.12^{+0.55}_{-0.37}$
	HPQCD [60]	> 16	π	$3.40 \pm 0.20^{+0.59}_{-0.39}$
	FNAL [61]	> 16	π, D	$3.62 \pm 0.22^{+0.63}_{-0.41}$
	LCSR [62]	< 16	ρ	2.75 ± 0.24
	LCSR [62]	full	ρ	2.58 ± 0.22
	LCSR[a]	full	ω	2.69 ± 0.24

[a] this analysis

Bibliography

[1] A. Sakharov, *Violation of CP Symmetry, C-Asymmetry and Baryon Asymmetry of the Universe*, Pisma Zh. Eksp. Teor. Fiz. **5**, 32 (1967); translation in JETP Lett. **5**, 24 (1967).

[2] J. Christenson *et al.*, *Evidence for the 2π Decay of the K_2^0 Meson*, Phys. Rev. Lett. **13**, 138 (1964).

[3] N. Cabibbo, *Unitary Symmetry and Leptonic Decays*, Phys. Rev. Lett. **10**, 531 (1963).

[4] M. Kobayashi and T. Maskawa, *CP-Violation in the Renormalizable Theory of Weak Interaction*, Prog. Theor. Phys. **49**, 652 (1973).

[5] A. Carter and A. Sanda, *CP Nonconservation in Cascade Decays of B Mesons*, Phys. Rev. Lett. **45**, 952 (1980).

[6] I. Bigi and A. Sanada, *Notes on the observability of CP violations in B decays*, Nucl. Phys. B **193**, 85 (1981).

[7] A. Carter and A. Sanda, *CP violation in B-meson decays*, Phys. Rev. D **23**, 1567 (1981).

[8] P. Oddone, *An Asymmetric B-Factory Based on PEP*, Annals N. Y. Acad. Sci. **578**, 237 (1989).

[9] Heavy Flavor Averaging Group, E. Barberio *et al.*, *Averages of b-hadron and c-hadron Properties at the End of 2007*, `arXiv:0808.1297 [hepex]` (2008), and recent updates: `http://www.slac.stanford.edu/xorg/hfag`.

[10] Belle Collaboration, I. Adachi *et al.*, *Measurement of exclusive $B \to X_u \ell \nu$ decays using full-reconstruction tagging at Belle*, `arXiv:0812.1414 [hep-ex]` (2008).

[11] *BABAR* Collaboration, B. Aubert *et al.*, *Measurement of the $B^+ \to \omega \ell^+ \nu$ and $B^+ \to \eta \ell^+ \nu$ Branching Fractions*, Phys. Rev. D **79**, 052011, `arXiv:0808.3524 [hep-ex]` (2008).

[12] `http://en.wikipedia.org/wiki/Standard_model.`

[13] I. Aitchison and A. Hey, *Gauge Theories in Particle Physics*, Taylor & Francis Group, New York (2004).

[14] Particle Data Group, C. Amsler *et al.*, Phys. Lett. **B667**, 1 (2008), and recent updates: `http://pdg.lbl.gov`.

[15] F. Halzen and A. Martin, *Quarks and Leptons*, John Wiley & Sons (1984).

[16] E. Noether, *Invariante Variationsprobleme*, Nachr. Ges. Wiss. Göttingen, 235 (1918).

[17] M. Peskin and D. Schroeder, *An Introduction to Quantum Field Theory*, Westview Press (1995).

[18] I. Bigi and A. Sanda, *CP Violation*, Cambridge University Press, Cambridge, U.K. (2000), chapter 4.

[19] M. Fierz, *Über die relativistische Theorie kräftefreier Teilchen mit beliebigem Spin*, Helvetica Physica Acta **12**, 3 (1939).

[20] W. Pauli, *The Connection Between Spin and Statistics*, Phys. Rev. **58**, 716 (1940).

[21] S. Weinberg, *Current Algebra and Gauge Theories. I*, Phys. Rev. D **8**, 605 (1973).

[22] S. Weinberg, *A Model of Leptons*, Phys Rev. Lett. **19**, 1264 (1967).

[23] L. Wolfenstein, *Parametrization of the Kobayashi-Maskawa Matrix*, Phys. Rev. Lett. **51**, 1945 (1983).

[24] Z. Maki, *Remarks on the Unified Model of Elementary Particles*, Prog. Theor. Phys. **28**, 870 (1962).

[25] BABAR Collaboration, B. Aubert *et al.*, *Improved Measurement of CP Violation in Neutral B Decays to $c\bar{c}s$*, Phys. Rev. Lett. **99**, 171803 (2007).

[26] F. Gilman and R. Singleton, *Analysis of semileptonic decays of mesons containing heavy quarks*, Phys. Rev. D **41**, 142 (1990).

[27] I. Bigi *et al.*, *QCD predictions for lepton spectra in inclusive heavy flavor decays*, Phys. Rev. Lett. **71**, 496 (1993).

[28] N. Uraltsev, *Theoretical Uncertainties in $\Gamma_{sl}(b \to u)$*, Int. J. Mod. Phys. **A14**, 4641 (1999).

[29] F. DeFazio and M. Neubert, *$B \to X_u \ell \nu_\ell$ decay distributions to order α_s*, J. High Energy Phys. JHEP06, 017 (1999).

[30] M. Neubert, *Analysis of the photon spectrum in inclusive $B \to X_s \gamma$ decays*, Phys. Rev. D **49**, 4623 (1994).

[31] BABAR Collaboration, B. Aubert *et al.*, *Measurement of the inclusive electron spectrum in charmless semileptonic B decays near the kinematic end point and determination of $|V_{ub}|$*, Phys. Rev. D **73**, 012006 (2006).

[32] BABAR Collaboration, B. Aubert *et al.*, *Determination of $|Vub|$ from Measurements of the Electron and Neutrino Momenta in Inclusive Semileptonic B Decays*, Phys. Rev. Lett. **95**, 111801 (2005).

[33] *BABAR* Collaboration, B. Aubert *et al.*, *Measurements of Partial Branching Fractions for $B^- \to X_u \ell^- \bar{\nu}$ and Determination of $|V_{ub}|$*, Phys. Rev. Lett. **100**, 171802 (2008), `arXiv:0708.3702v2 [hep-ex]`.

[34] P. Ball and V. Braun, *Exclusive semileptonic and rare B meson decays in QCD*, Phys. Rev. D **58**, 094016 (1998).

[35] J. Richman and P. Burchat, *Leptonic and semileptonic decays of charm and bottom hadrons*, Rev. Mod. Phys. **67**, 893 (1995).

[36] N. Isgur *et al.*, *Semileptonic B and D decays in the quark model*, Phys. Rev. D **39**, 799 (1989).

[37] D. Scora and N. Isgur, *Semileptonic meson decays in the quark model: An update*, Phys. Rev. D **52**, 2783 (1995).

[38] I. Balitsky *et al.*, *Radiative decay $\sigma^+ \to p\gamma$ in quantum chromodynamics*, Nucl. Phys. B **312**, 509 (1989).

[39] V. Chernyak and I. Zhitnitsky, *B-meson exclusive decays into baryons*, Nucl. Phys. B **345**, 137 (1990).

[40] C. Boyd et al., *Constraints on Form Factors for Exclusive Semileptonic Heavy to Light Meson Decays*, Phys. Rev. Lett. **74**, 4603 (1995).

[41] C. Boyd and M. Savage, *Analyticity, shapes of semileptonic form factors, and $B \to \pi\ell\nu$*, Phys. Rev. D **56**, 303 (1997).

[42] J. Seeman, *Accelerator Physics of PEP-II*, part of the Accelerator Physics Lecture Series at SLAC, January-May 1998.

[43] *BABAR* Collaboration, P.F. Harrison and H.R. Quinn (editors), *The BABAR Physics Book: Physics at an Asymmetric B Factory*, SLAC-R-504 (1998).

[44] G.D. McGregor, *B Counting at BABAR*, SLAC-R-912, `arXiv:0812.1954v1 [hep-ex]` (2008).

[45] *BABAR* Collaboration, B. Aubert *et al.*, *The BABAR Detector*, Nucl. Instrum. Methods Phys. Res., Sect. C **A479**, 1 (2002).

[46] B. Rossi, *High-Energy Particles*, Prentice Hall Series, 1965.

[47] T. Böhringer *et al.*, *Observation of Υ, Υ', and Υ'' at the Cornell Electron Storage Ring*, Phys. Rev. Lett. **44**, 1111 (1980).

[48] G. Finocchiaro *et al.*, *Observation of Υ''' at the Cornell Electron Storage Ring*, Phys. Rev. Lett. **45**, 222 (1980).

[49] D. Lange, *The EvtGen particle decay simulation package*, Nucl. Instrum. Methods Phys. Res., Sect. A **462**, 152 (2001).

[50] GEANT4 Collaboration, S. Agostinelli *et al.*, *GEANT4 - a simulation toolkit*, Nucl. Instrum. Methods Phys. Res., Sect. A **506**, 250 (2003).

[51] P. Jackson and R. Kowalewski, *Tagging using $B \to Dl\nu(X)$ decays*, BABAR Analysis Document #537.

[52] G. Fox and S. Wolfram, *Observables for the Analysis of Event Shapes in e^+e^- Annihilation and Other Processes*, Phys. Rev. Lett. **41**, 1581 (1978).

[53] R. Faccini *et al.*, *Measurement of Branching Ratios of Charged and Neutral B mesons into Charmonium + K final states: Analysis for Osaka 2000*, BABAR Analysis Document #12, Appendix B.

[54] D. Dujmic, *Merged π^0 Reconstruction: From Cluster Shape to Mass*, BABAR Analysis Document #514.

[55] BABAR Collaboration, B. Aubert *et al.*, *Measurement of the Branching Fractions of $\bar{B} \to D^{**}\ell^-\bar{\nu}_\ell$ Decays in events Tagged by a Fully Reconstructed B Meson*, SLAC-PUB-13351, Phys. Rev. Lett. **101**, 261802, `arXiv:0808.0528 [hep-ex]` (2008).

[56] `http://www.slac.stanford.edu/BFROOT/www/Physics/Analysis/AWG/Neutrals/validation/recipie18.html`.

[57] M. Allen *et al.*, *A Measurement of π^0 Efficiency Using $\tau \to \rho\nu$ and $\tau \to \pi\nu$ Decays*, BABAR Analysis Document #870.

[58] P. Ball and R. Zwicky, *$B_{d,s} \to \rho, \omega, K^*, \phi$ form factors from light-cone sum rules reexamined*, Phys. Rev. D **71**, 014029 (2005).

[59] P. Ball and R. Zwicky, *New Results on $B \to \pi, K, \eta$ Decay Form Factors from Light-Cone Sum Rules*, Phys. Rev. D **71**, 014015, `arXiv:hep-ph/0406232` (2005).

[60] E. Dalgic *et al.*, *B Meson Semileptonic Form Factors from Unquenched Lattice QCD*, Phys. Rev. D **73**, 074502, `arXiv:hep-lat/0601021` (2006).

[61] M. Okamoto *et al.*, *Semileptonic $D \to \pi/K$ and $B \to \pi/D$ decays in 2+1 flavor lattice QCD*, Nucl. Phys. Proc. Suppl. **140**, 461, `arXiv:hep-lat/0409116` (2005).

[62] J. Dingfelder *et al.*, *Study of $B \to \pi\ell\nu$ and $B \to \rho\ell\nu$ Decays and Determination of $|V_{ub}|$* , BABAR Analysis Document #2034.

[63] J. Hewett *et al.*, *The Discovery Potential of a Super B Factory. Proceedings of the 2003 SLAC Workshops.*, SLAC-R-709, `arXiv:hep-ph/0503261` (2004).

Appendix A

Mathematical Derivations

A.1 Derivation of $\cos\theta_{BY}$

In a semileptonic decay $B \to X\ell\nu$, the momenta of the hadron X and the lepton ℓ can be combined to form a hypothetical Y particle, such that the decay may be regarded as a three-body decay $B \to Y\nu$. Assuming a massless neutrino, momentum conservation at the decay vertex then implies

$$\begin{aligned} 0 &= m_\nu^2 = p_\nu^2 = (p_B - p_Y)^2 \\ &= p_B^2 + p_Y^2 - 2p_B \cdot p_Y \\ &= m_B^2 + m_Y^2 - 2(E_B E_Y - \boldsymbol{p}_B \cdot \boldsymbol{p}_Y) \end{aligned} \tag{A.1}$$

where m_i, p_i, E_i, and $\boldsymbol{p}_i$ are the mass, four-momentum, energy, and three-momentum of particle type i, respectively. Thus

$$2\boldsymbol{p}_B \cdot \boldsymbol{p}_Y = 2E_B \cdot E_Y - m_B^2 - m_Y^2 \tag{A.2}$$

$$\cos\theta_{BY} = \frac{2E_B \cdot E_Y - m_B^2 - m_Y^2}{2|\boldsymbol{p}_B| \cdot |\boldsymbol{p}_Y|} \tag{A.3}$$

which is Eq. 6.1, and is valid in any frame of reference. In the CM frame however, i.e. the in rest frame of the $\Upsilon(4S)$, the energy of either B meson is given as half of the $\Upsilon(4S)$ mass, so that both E_B^* and $|\boldsymbol{p}_B^*|$ are determined, and $\cos\theta_{BY}$ can be calculated without any specific knowledge of the B meson kinematics.

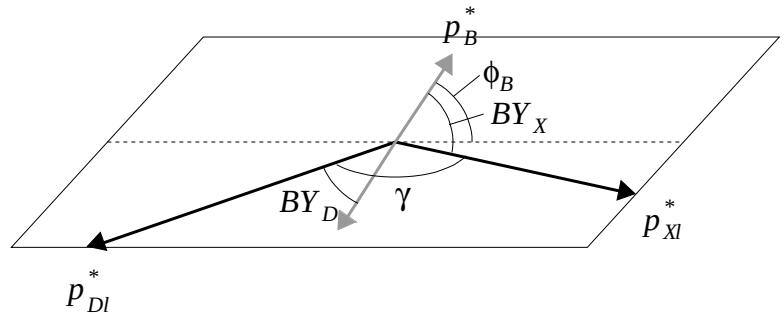

Figure A.1: Event kinematics of a double-semileptonic decay. In the text, the angles BY_D and BY_X are referred to as θ_{BY} and θ_{BX}, respectively, and the $D\ell$ and $X\ell$ systems are referred to as Y and X, respectively.

A.2 Derivation of $\cos^2 \Phi_B$

Figure 8.1 is reproduced here as Fig. A.1 for ease of reference(convenience), and depicts the event kinematics of a double-semileptonic decay in the CM frame.[1] The two combined momentum vectors of all measured (i.e. excluding the two neutrinos) tag and signal side particles, $\boldsymbol{p}^*_{D\ell}$ and $\boldsymbol{p}^*_{X\ell}$, respectively, define a plane, characterized by the unit vector $\hat{\boldsymbol{n}}$ perpendicular to it,

$$\hat{\boldsymbol{n}} \equiv \frac{\boldsymbol{p}^*_{D\ell} \times \boldsymbol{p}^*_{X\ell}}{|\boldsymbol{p}^*_{D\ell}| \cdot |\boldsymbol{p}^*_{X\ell}| \cdot \sin\gamma} = \frac{\hat{\boldsymbol{p}}^*_{D\ell} \times \hat{\boldsymbol{p}}^*_{X\ell}}{\sin\gamma} \tag{A.4}$$

where $\hat{\boldsymbol{p}}$ denotes a momentum unit vector, and γ is the angle between $\boldsymbol{p}^*_{D\ell}$ and $\boldsymbol{p}^*_{X\ell}$. The cross-product of $\hat{\boldsymbol{n}}$ and the normalized momentum vector $\hat{\boldsymbol{p}}^*_B$ of either B meson yields the sine of the complement of Φ_B,

$$\begin{aligned} |\cos\Phi_B| &= |\sin(\pi/2 - \Phi_B)| = \left| \hat{\boldsymbol{p}}^*_B \times \frac{\hat{\boldsymbol{p}}^*_{D\ell} \times \hat{\boldsymbol{p}}^*_{X\ell}}{\sin\gamma} \right| \\ &= \left| \frac{\hat{\boldsymbol{p}}^*_{D\ell}(\hat{\boldsymbol{p}}^*_B \cdot \hat{\boldsymbol{p}}^*_{X\ell}) - \hat{\boldsymbol{p}}^*_{X\ell}(\hat{\boldsymbol{p}}^*_B \cdot \hat{\boldsymbol{p}}^*_{D\ell})}{\sin\gamma} \right| \\ &= \left| \frac{\hat{\boldsymbol{p}}^*_{D\ell}\cos(BY_X) + \hat{\boldsymbol{p}}^*_{X\ell}\cos(BY_D)}{\sin\gamma} \right| \end{aligned} \tag{A.5}$$

[1] This derivation is only valid in the CM frame, since then the two B mesons emerge back-to-back and thus span the same angle with respect to a given plane.

since $\hat{\boldsymbol{p}}_B^* \cdot \hat{\boldsymbol{p}}_{X\ell}^* = \cos(BY_X)$ and $\hat{\boldsymbol{p}}_B^* \cdot \hat{\boldsymbol{p}}_{D\ell}^* = -\hat{\boldsymbol{p}}_{\bar{B}}^* \cdot \hat{\boldsymbol{p}}_{D\ell}^* = -\cos(BY_D)$. In this equation, the absolute value is taken to account for the ambiguity in assigning $\boldsymbol{p}_B^*$ and $\boldsymbol{p}_{\bar{B}}^*$, which yields an overall minus sign. Taking the square and using $\hat{\boldsymbol{p}}_{D\ell}^* \cdot \hat{\boldsymbol{p}}_{X\ell}^* = \cos\gamma$, one finds

$$\begin{aligned} \cos^2\Phi_B &= \frac{cos^2(BY_X) + 2\cos(BY_X)\cos(BY_D)(\hat{\boldsymbol{p}}_{D\ell}^* \cdot \hat{\boldsymbol{p}}_{X\ell}^*) + \cos^2(BY_D)}{\sin^2\gamma} \\ &= \frac{cos^2(BY_X) + 2\cos(BY_X)\cos(BY_D)\cos\gamma + \cos^2(BY_D)}{\sin^2\gamma} \end{aligned} \tag{A.6}$$

which is Eq. 8.1, adjusted for notation.

Appendix B

Form factors from light-cone sum rules

A value for $\Delta\zeta$ is obtained by integrating Eq. 2.26 over the full kinematic regime of q^2, from $q^2_{\rm min} = 0$ to $q^2_{\rm max} = (m_B - m_\omega)^2 = 20.22$ GeV^2, using the method of light-cone sum rules. An expression for $\mathrm{d}\Gamma/\mathrm{d}q^2$ is obtained by integrating Eq. 2.23 over $\cos\theta_{W\ell}$

$$\frac{\mathrm{d}\Gamma}{\mathrm{d}q^2} = |V_{ub}|^2 \frac{G_F^2 |\boldsymbol{p}_\omega| q^2}{96\pi^3 m_B^2} \left[|H_+|^2 + |H_-|^2 + |H_0|^2 \right] \tag{B.1}$$

where the vector meson was specified to be an ω. The squared momentum transfer q^2 is defined as

$$q^2 \equiv (p_\ell + p_\nu)^2 = (p_B - p_\omega)^2 \tag{B.2}$$

where p_X is the four-momentum of particle X. Evaluated in the B meson rest frame,[1] the magnitude of the ω three-momentum can be expressed in terms of q^2:

$$|\boldsymbol{p}_\omega(q^2)| = \sqrt{\left(\frac{m_B^2 + m_\omega^2 - q^2}{2m_B} \right)^2 - m_\omega^2} \tag{B.3}$$

The three helicity amplitudes in Eq. B.1 are given in terms of the relevant form factors by Eq. 2.22; these form factors in turn are written as a dispersion integral in q^2 and can be modeled by various pole ansätze [58]

$$V(q^2) = \frac{r_1}{1 - q^2/m_R^2} + \frac{r_2}{1 - q^2/m_{\rm fit}^2} \tag{B.4a}$$

$$A_1(q^2) = \frac{r_2}{1 - q^2/m_{\rm fit}^2} \tag{B.4b}$$

$$A_2(q^2) = \frac{r_1}{1 - q^2/m_{\rm fit}^2} + \frac{r_2}{(1 - q^2/m_{\rm fit}^2)^2} \tag{B.4c}$$

[1] which is a good approximation for the CM frame

Table B.1: Parameters for the LCSR form factor calculation for the hadronic $B \to \omega$ transition to a vector meson [58, Tables VIII and IX].

Form factor	$F(0)$	r_1	r_2	m^2_{fit} (GeV$^2/c^4$)	m_R (GeV$/c^2$)
V	0.293	1.006	-0.713	37.45	5.32
A_1	0.219	-	0.217	37.01	-
A_2	0.198	0.006	0.192	41.24	-

where the various parameters are given in Table B.1.

The form factors obtained in this way are shown in Fig. B.1, along with the q^2 dependence of the magnitude of the ω momentum. Integration over the full kinematic regime yields

$$\Delta\zeta = 11.87\,\text{ps}^{-1} \tag{B.5}$$

Estimates of the uncertainties of the form-factor integrals are not available.

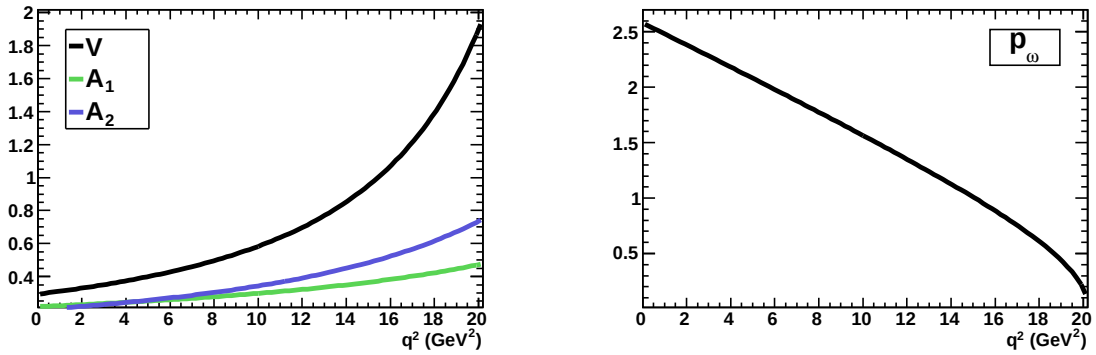

Figure B.1: Form factors (left) and momentum distribution of the ω (right) for $B \to \omega$ decays, as a function of the squared momentum transfer q^2.